Modeling the Effects of Frost Damage on Concrete Structures

By

Maryah Zia Rana

A thesis

Presented to the University of Ottawa in fulfillment of the requirements for Master of Applied Science in Civil Engineering

Department of Civil Engineering

University of Ottawa

Ottawa, Canada

K1N 6N5

December 2019

Abstract

Deteriorating concrete structures demand reliable methods for assessing and quantifying damage. In cold regions, concrete structures are susceptible to freeze and thaw cycles which cause frost damage. Frost damage has been observed to cause most severe type of deterioration in concrete structures as it significantly reduces the strength, stiffness and durability. Due to the climate conditions, concrete infrastructure in Canada is especially prone to frost damage. Since the 1930s, entrained air was found to greatly increase the concrete resistance against surface scaling by de-icing salts. Air entrainment has since become an efficient measure against frost damage of concrete used in environments with freezing and thawing. Currently, however, Canadian standards for concrete structures do not provide explicit guidelines for the evaluation of frost damage. Understanding the effects of frost damage on concrete structures is essential for developing methods to effectively quantify and assess the impact of this deterioration mode on the structural capacity of concrete infrastructure. This study proposes a structural analysis method that accounts for the degradation of the load carrying capacity and stiffness of frost-damaged reinforced concrete flexural members. The method is developed through nonlinear finite element analyses of reinforced concrete beams in which frost damage is accounted for by modifying mechanical properties according to existing analytical constitutive models for frost-damaged concrete in compression and tension, and for bond steel-concrete interaction. The analysis procedure is validated with published experimental results of reinforced concrete beams subjected to frost damage. A parametric analysis of design variables and level of frost damage is also presented in order to establish the importance of each in the behavior of damaged reinforced concrete beams.

Acknowledgements

I would like to thank Dr. Beatriz Martin-Pérez for allowing me the opportunity to complete this work under her supervision. I would also like to thank my mother, Sultana for her unconditional love and support. The kindness and generosity of these women made it possible for me to undertake and complete this research project.

Table of Contents

List of Tables

List of Figures

Notation

b = width of beam cross-section
d = effective beam depth
D = damage expressed as loss in dynamic modulus of elasticity
E_c = modulus of elasticity
E_c^d = secant elastic modulus of frost damaged concrete
E_0^d = tangential elastic modulus of the damaged concrete
$E_{D,rel}^d$ = relative dynamic modulus of elasticity for damaged concrete
f_c = the compressive strength of concrete
f_c^d = the compressive strength of frost damaged concrete
f_{c1}^a = average concrete tensile stress due to tension stiffening effects
f_{c1}^b = average concrete tensile stress due to tension softening effects
f_{cc}^d = biaxial compressive strength of frost damaged concrete
f_{cr} = cracking stress of the concrete determined by the cracking criterion model
f_{cru} = unconfined cracking strength
f_t = tensile strength
f_t^d = tensile strength of frost-damaged concrete
G_f = concrete’s fracture energy
h = beam depth
K = slope of the scaling curve
K_N = coefficient of fatigue
l = span between supports
N = number of freeze-thaw cycles
S = degree of saturation
S_{cr} = critical degree of saturation
w = crack width in the element
w_{crx} = average crack width
w_{ult} = ultimate crack width

ΔQ = dry-weight loss per unit area,

β_d = softening parameter

β_{cr} = crack coefficient

$\epsilon_{c,p}^{d}$ = strain at peak compressive stress of frost damaged concrete

$\epsilon_{t,p}^{d}$ = strain at peak tensile stress of frost damaged concrete

τ_f = residual bond strength for undamaged concrete

τ_f^d = residual bond strength for damaged concrete

τ_{max} = maximum bond strength for undamaged concrete

τ_{max}^d = maximum bond strength for damaged concrete

ρ = reinforcement ratio

Chapter 1. Introduction

1.1 Background

Structural concrete that has been properly specified can be quite resistant to low temperatures; it can even be used for containers that store liquid gas at cryogenic temperatures (Li 2016). However, in Canada and in other cold climates, concrete infrastructure becomes vulnerable to frost damage when exposed to water and freeze-thaw cycles. Successive freezing and subsequent thawing cycles result in the change of liquid water into ice inside the concrete pore system. This water phase change results in a 9% volume expansion. The solid matrix of the material is not able to accommodate this volume expansion and as a result, internal stresses develop. These stresses introduce micro and macro cracks in the concrete and can result in cracking and spalling of the concrete cover. This is referred to as internal frost damage (Pigeon *et al.* 1996). Change in the relative dynamic modulus of elasticity is used to quantify this internal frost damage. ASTM C666 is the published test method for measuring dynamic modulus of elasticity of concrete specimens subjected to rapidly repeated freeze-thaw cycles.

Hydraulic structures such as dams, especially at the waterline, and highway bridges exposed to water are prone to frost damage when subjected to freeze-thaw cycles. These structures can have a high saturation degree due to their exposure to water. As the external temperature drops, the water in the concrete pores freezes and subsequently thaws back to its liquid state when the temperature rises. This process of water freezing introduces pressure in the concrete pores, and ice thawing relieves the pores of this pressure. These cycles of increase and subsequent alleviation of pore pressure induces damage in the concrete. Nineteen percent of dam deterioration was reported to be caused by frost damage (ICOLD 1984). Likewise, concrete highway bridges can have a high degree of saturation in the winter season and experience severe damage as they are subject to freezing and subsequent thawing. Figure 1.1 shows frost damage in concrete piers of a highway bridge.

Figure 1.1. Concrete piers of a highway bridge subject to frost damage (reproduced from Li 2016)

Furthermore, freeze-thaw cycles in the presence of salts cause severe surface damage in concrete. In Canada, during the cold months, de-icing salts are commonly used on roads and pavements. Deterioration of concrete bridge decks and road slabs is often observed as a result of successive freezing and thawing in the presence of these de-icing salts. This type of frost damage is also prevalent in concrete elements that are in contact with saline water bodies such as sea water or ground water with high salt content. Surface damage caused by salts is treated differently compared to frost damage without salts (Li 2016).

1.2 Scope of Research

Frost-damaged concrete structures demand reliable methods for quantifying damage and loss of capacity. Previous research on this subject has primarily focused on the causes and mechanisms of frost deterioration and its effects at the material level, while less attention has been given to assess its impact on the structural behaviour of damaged structures built with no air-entrained concrete. Several studies have investigated the influence of internal frost damage on material properties of concrete and steel-concrete bond (Hanjari *et al.* 2011, Qin *et al.* 2016), but only few studies have focused on the structural response of frost-damaged concrete structures (Hassanzadeh and Fagerlund 2006, Tang and Petersson 2004). In order to effectively assess existing frost-damaged reinforced concrete structures, methods to accurately predict the load carrying capacity and the remaining service life are needed.

The aim of this research is to propose a structural analysis method that accounts for the degradation of the load carrying capacity and stiffness of frost-damaged reinforced concrete flexural members. The scope of this work includes the following:

(i) a literature review of previous experimental studies on the effect of freeze-thaw cycles on concrete compressive and tensile strengths, on concrete stiffness, and on the bond-slip relationship between reinforcement and concrete as well as on the structural behaviour of reinforced concrete members;

(ii) nonlinear finite element analyses of reinforced concrete beams in which frost damage is accounted for by modifying existing analytical constitutive models for concrete in compression and tension and for bond steel-concrete interaction, by modifying the member's geometry to account for surface scaling, and by applying an uneven damage distribution on the member;

(iii) validation of the analysis procedure with published experimental results of reinforced concrete beams subjected to frost damage; and,

(iv) a parametric analysis of design variables and level of frost damage to establish the importance of each in the behavior of damaged reinforced concrete beams.

1.3 Organization of Thesis

In chapter two, background information on the deterioration of reinforced concrete structures due to frost damage is provided. The literature pertaining to the effects of frost damage on the bond and material properties as well as the capacity of flexural members is discussed. The current measures against frost damage are also discussed and research needs are presented.

The methodology implemented to model frost damage in the finite element analysis of reinforced concrete structures is presented in chapter three. The mechanical behaviour of concrete is modified, which allows for frost damage to be quantified and the structural response of frost-damaged reinforced concrete members to be understood.

In chapter four, the methodology developed in chapter three for modeling frost-damaged beams is validated. The proposed methodology is used in the non-linear finite element analysis of frost damaged beams that were tested by Hassanzadeh and Fagerlund (2006) as part of a research study to investigate the behaviour of frost-damaged reinforced concrete beams. The load-carrying capacity and failure mode of the beams predicted by the numerical analysis are compared with the available experimental data in order to validate the proposed methodology.

Chapter five presents a parametric study of external and internal parameters using the methodology that was proposed and validated in the previous chapters. The influence of each parameter on the damage degree and the subsequent reduction in the load capacity is investigated. The test specimen used for the parametric analysis was designed in accordance with CSA A23.3. The results and a discussion of the results are also presented in this chapter.

Lastly, the thesis conclusions are discussed in chapter six, in which considerations for future research are also presented.

Chapter 2. Literature Review

2.1 Introduction

In this chapter, background information on the deterioration of reinforced concrete structures due to frost damage is provided. The literature pertaining to the effects of frost damage on the steel-concrete bond and concrete material properties as well as the capacity of flexural members is discussed. The current measures against frost damage are also discussed and research needs are presented.

2.2 Frost Damage

In cold regions, concrete structures are susceptible to freeze and thaw cycles which cause the most severe type of deterioration (Nili *et al.* 2017). Due to the climate conditions, concrete infrastructure in Canada is especially prone to frost damage. The damage caused by freeze-thaw cycles is related to the water phase change in concrete pores; the pore system cannot accommodate the volume expansion of freezing water, which is restrained by the surrounding concrete. The resulting tensile stresses induce micro and macro cracks in the concrete, causing damage known as internal frost damage. In addition, concrete surfaces exposed to freeze-thaw cycles in the presence of moisture and/or de-icing salts are also susceptible to scaling. This type of damage is termed “surface scaling” or “salt scaling.”

Frost-damaged concrete has been researched for more than half a century. Much of the early works have focused primarily on explaining the mechanisms responsible for frost deterioration. These publications have established concepts that aid in the understanding of the deterioration processes that takes place when concrete is subjected to freeze-thaw cycles. Powers (1949) proposed the hydraulic pressure theory, which states that frost damage is caused by the increase in pore pressure when there is liquid water flow due to the ice volume expansion of 9% in the pores. The osmotic theory was later suggested by Powers and Helmuth (1953) to further explain that the local condensation of pore solution is responsible for driving the liquid water to the freezing site in pores and thus, severe scaling can be observed with the presence of salt. The micro lens theory proposed by Setzer (2001) considered the water-vapour-ice equilibrium in pores during freezing and verified the suction effect of external water during one sided thawing. The phenomenon of water absorption and the damage accompanying freeze-thaw cycles have been addressed by the critical pore saturation theory (Fagerlund 1993) and the low-cycle fatigue theory (Fagerlund 2002). The pore crystallization theory (Scherer 1999) and poromechanics theory (Coussy 2005) have been developed to investigate more formally the pore phase change.

Since the early works of Power and the development of the hydraulic pressure theory, a group of experimental studies have investigated the influence of freeze-thaw cycles on material properties of concrete and steel-concrete bond. A few studies have focused on modeling the structural response of frost-damaged reinforced concrete structures. These experimental works have shown that frost damage significantly reduces the strength, stiffness and durability of concrete structures (Ma *et al.* 2017).

2.3 Mechanical Properties of Frost-Damaged Concrete

2.3.1 Frost-Damaged Concrete in Compression

Published results show that there is a significant influence of freeze–thaw cycles on the compressive strength of concrete. The compressive stress–strain curve of frost-damaged concrete is shown to be significantly different from that of undamaged concrete. When compared with the undamaged concrete, the frost-damaged concrete exhibits lower initial elastic modulus, a larger strain at the peak stress and a more ductile behaviour in the descending branch as shown in Figure 2.1.

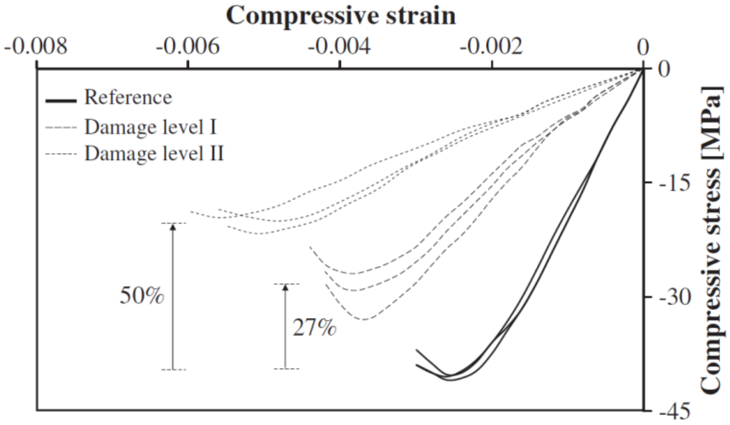

Figure 2.1. Compressive stress-strain curves of 200×100 mm cylinder specimens (reproduced from Hanjari *et al.* 2011)

As part of an experimental study, Hanjari *et al.* (2011) carried out compression tests on cylinders of 200×100 mm (Figure 2.1). Reference specimens as well as frost-damaged specimens were tested. The level of frost damage was quantified by a reduction in the compressive strength. Damage level I refers to specimens that underwent freeze-thaw cycles and experienced a 25% reduction in compressive strength. Damage level II refers to specimens that underwent freeze-thaw cycles and experienced a 50% reduction in compressive strength. A 43% and 84% reduction in the elastic modulus was observed in specimens with damage level I and damage level II, respectively. The authors noted that the frost-damaged concrete had larger strains at peak stresses and exhibited a more ductile behaviour in the post-peak range compared to the undamaged concrete. A change in the stiffness was also noted in the pre-peak curves of the frost-damaged concrete. This was attributed to the randomly oriented cracks in the frost-damaged specimens resulting from freeze-thaw cycles. The frost-damaged specimens were initially loaded with low stiffness, but as loading continued and the cracks perpendicular to the loading direction closed, the concrete experienced a slight increase in stiffness. However, it was noted that the stiffness never fully recovered and a permanent stiffness loss was observed.

In a study where the main focus was to investigate fracture behavior of concrete exposed to freeze-thaw cycles, Ma *et al*. (2017) also carried out compression tests on frost-damaged concrete. The compression tests were carried out on specimens with dimensions of $100 \times 100 \times 100\ mm^3$ using a servo-controlled testing machine. It was observed that the compressive strength decreased as the number of freeze-thaw cycles increased. After 100 freeze-thaw cycles, the compressive strength of the concrete specimen decreased by approximately 55%. The maximum applied load for the specimen without frost damage was 1.11 times higher than for the specimen which had undergone 100 freeze-thaw cycles. Furthermore, it was observed that with increasing freeze-thaw cycles, the slopes and area of the load-deformation curves decreased. These experimental results are in agreement with the observations of Hanjari *et al.* (2011)

The relationship between mechanical properties of undamaged concrete and its compressive strength are well established and widely used. Li *et al.* (2017) proposed similar relationships for frost-damaged concrete. The index of relative compressive strength (*RCS*) was established as the indicator of frost damage. *RCS* is the ratio of compressive strength of frost-damaged concrete to compressive strength of undamaged concrete. Experimental data on the mechanical performance of frost-damaged concrete was collected from the literature and analyzed in order to propose a method for the estimation of the mechanical performance of frost-damaged concrete. The plots in Figure 2.2 were produced to show the dimensionless data of the elastic modulus under compression, strain at peak compressive stress, and biaxial compressive strength versus *RCS*. It was noted that as the *RCS* decreases, so does the relative initial elastic modulus and relative biaxial compression strength, while the strain at peak compressive stress increases.

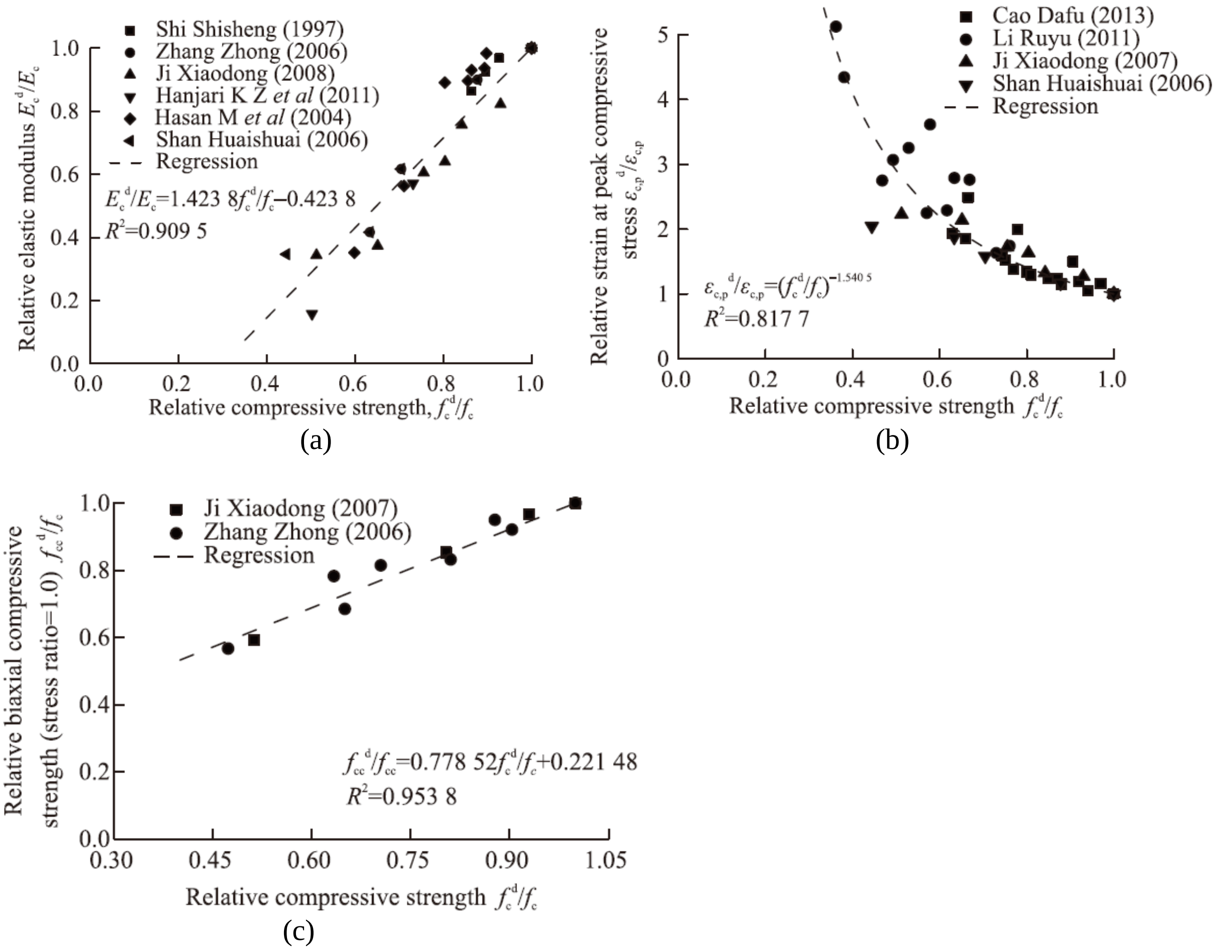

(a)

(b)

(c)

Figure 2.2. Relative compressive strength, RCS versus (a) Relative elastic modulus (b) Relative strain at peak compressive stress (c) Relative biaxial compressive strength (reproduced from Li *et al.* 2017)

The following relationships for the elastic modulus under compression, the strain at the peak compressive stress, and the biaxial compressive strength of frost-damaged concrete were proposed (Li *et al*. 2017):

$$E_c^d = \frac{10^5}{2.2 + 2.64/f_c} \left(1.4238\frac{f_c^d}{f_c} - 0.4238\right) \tag{2.1}$$

$$\epsilon_{c,p}^d = \left(0.833 + 0.135\sqrt{f_c}\right)\left(\frac{f_c^d}{f_c}\right)^{-1.5045} \times 10^{-3} \tag{2.2}$$

$$f_{cc}^d = (1.15 - 1.35)\left(0.77852\frac{f_c^d}{f_c} + 0.22148\right)f_c \tag{2.3}$$

where E_c^d is the secant elastic modulus of frost-damaged concrete, f_c^d is the compressive strength of frost-damaged concrete, f_c the compressive strength of concrete, $\epsilon_{c,p}^d$ is the strain at peak compressive stress of frost-damaged concrete and f_{cc}^d is the biaxial compressive strength of frost-damaged concrete.

2.3.2 Frost-Damaged Concrete in Tension

Frost damage has been reported to have a larger effect on the tensile strength of concrete than on the compressive strength. In the same study discussed above, Hanjari *et al.* (2011) conducted splitting tensile and wedge splitting tests to investigate the tensile strength of frost-damaged concrete. The wedge splitting test results were used in an inverse analysis to estimate the tensile strength. The results show that a 25% and 50% (damage level I and damage level II) reduction in compressive strength due to frost damage correspond to approximately 29% and 63% reduction in splitting tensile strength. A 10% difference was observed between the tensile strength estimated by the splitting tensile test and the tensile strength estimated by wedge splitting test. The effects of frost damage were greater on tensile strength than on compressive strength. The author noted that these results agree with what has been previously observed by other researchers and attributed the slightly larger reduction of tensile strength to the cracks formed during the freeze-thaw cycles. When the frost-damaged concrete experiences compression, cracks perpendicular to the direction of the applied force are closed, whereas in tension, these cracks contribute to the failure of the concrete specimen.

As with the dimensionless data of relative elastic modulus, relative strain at peak compressive stress and relative biaxial compressive strength for frost-damaged concrete, Li *et al.* (2017) also plotted the dimensionless data of tensile strength and strain at peak tensile stress against the relative compressive strength *(RCS)*. These plots are shown in Figure 2.3.

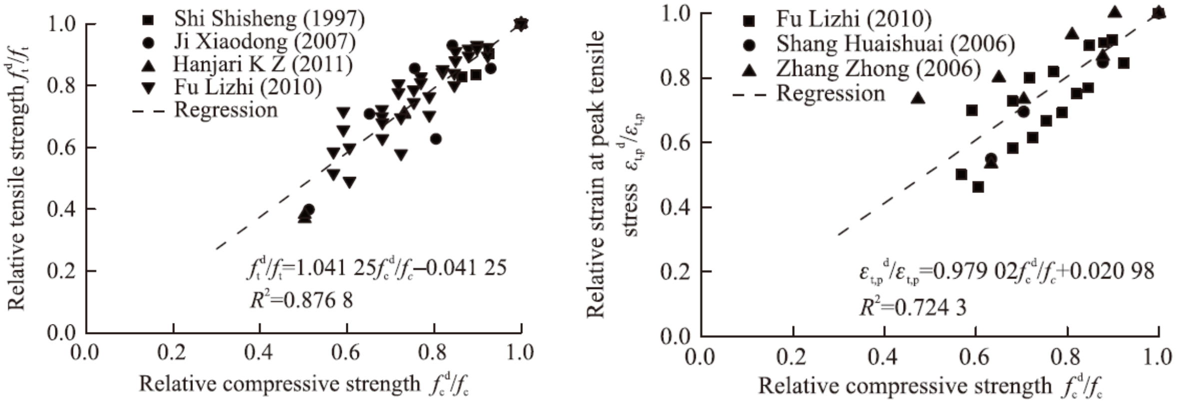

(a) (b)

Figure 2.3. Relative compressive strength, *RCS* versus (a) Relative tensile strength (b) Relative strain at peak tensile stress (reproduced from Li *et al*. 2017)

The following relationships were proposed by Li *et al.* (2017) for calculating the tensile strength and strain at peak tensile stress of frost-damaged concrete:

$$f_t^d = 0.302 f_c^{\frac{2}{3}}(1.04125\frac{f_c^d}{f_c} - 0.04125) \tag{2.4}$$

$$\begin{aligned}\epsilon_{t,p}^d = 34.03 \times 10^{-6} f_c^{0.36}(0.97902\frac{f_c^d}{f_c} \\ + 0.02098)\end{aligned} \tag{2.5}$$

where f_t^d is the tensile strength of frost-damaged concrete, and $\epsilon_{t,p}^d$is the strain at peak tensile stress of frost-damaged concrete.

2.4 Effects of Frost Damage on Bond Strength

Frost damage in the concrete cover is an indicator of change in the bond behaviour between steel reinforcement and concrete. This is due to the ring tension stress present during bond action. When this tension is greater than the capacity of the concrete cover to resist it, bond failure takes place and cracks form along the reinforcement as a result of this failure. The concrete cover has the smallest cross section of concrete resisting the ring tension stress and is the area where this mechanism of crack initiation takes place (Petersen *et al.* 2007).

Petersen *et al.* (2007) carried out pull-out tests to investigate this bond behaviour. The reinforcing bars were eccentrically placed in the pull-out specimen in order to simulate the bond in flexural reinforced concrete members. The results from the pull-out test indicated that bond behaviour changes with deterioration, which was quantified by the relative dynamic modulus of elasticity. The deterioration caused by successive freeze-thaw cycles lengthens the time required for an ultrasonic wave to travel through the concrete. The relative dynamic modulus of elasticity can be derived from this and hence is used to quantify the internal damage. The dynamic modulus of elasticity describes the deformation resistance under impulsive load, which is similar to ultrasound in that it spreads wavelike in the concrete. From the results of the experiments, it was observed that there is a decrease of the maximum bond tension corresponding to the pull-out load. Also, at the maximum bond tension, there is a change in the observed slip. It was also observed that there is some reduction in slip values at the maximum bond tension when the amount of damage is small and only the area of the concrete cover is included. However, when the damage is at a greater depth and affecting the area near the reinforcement, the slip values at the maximum bond tension increase rapidly (Figure 2.4).

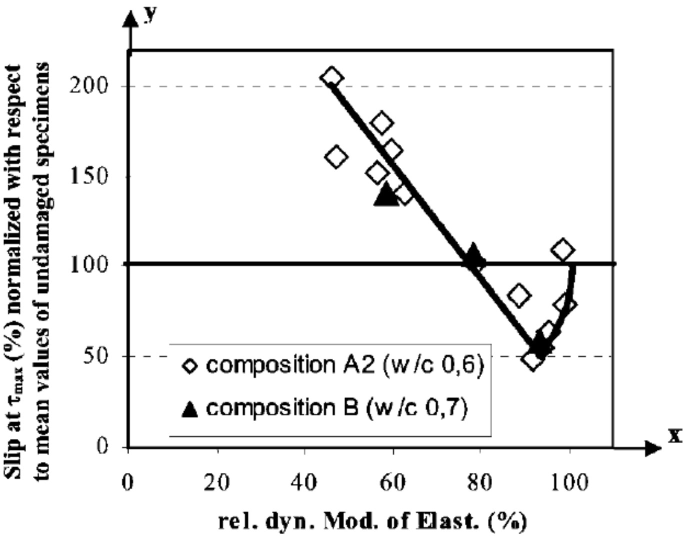

Figure 2.4. Variation of the slip values at the maximum bond tension in relation to the level of the internal damage (reproduced from Petersen *et al.* 2007)

The variation of the slip values at the maximum bond tension was explained using the four specifically measured bond tension-slip curves as presented in Figure 2.5. The curve identified as "undamaged" represents the results of the pull-out test on an undamaged specimen. The results of the pull-out test on specimens with varying degrees of damage are represented with curves A, B, and C. The degree of damage increases from specimen A to C. In the case of curve A, the frost damage in the specimen is only in the area of the concrete cover. The concrete area surrounding the reinforcement is undamaged, and thus the stress-strain behaviour of concrete remains unchanged. Until the point of maximum bond-tension, the curve follows the path of the curve of the undamaged specimen. The decrease in the maximum bond tension is due to the frost damage in the concrete cover. Thus, specimens with a relative low degree of damage have a smaller slip values at the maximum bond tension.

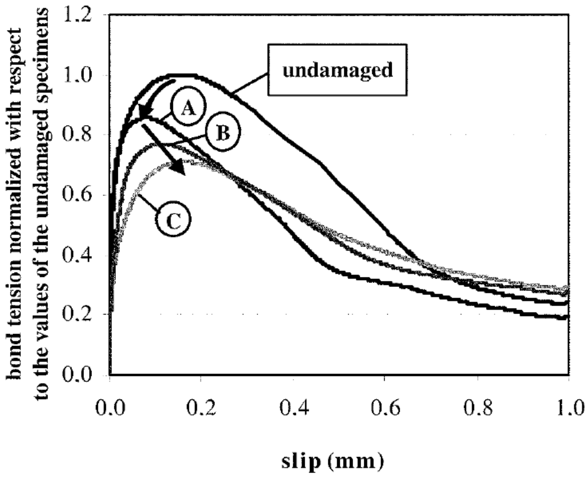

Figure 2.5. Bond-slip curves reflecting freezing and thawing induced changes of bond behavior (reproduced from Petersen *et al.* 2007)

Curves B and C represent results for specimens that experienced frost damage reaching the reinforcing steel. These curves show the maximum bond tension decreasing and the slip increasing rapidly. This behavior is evident both before and after the maximum bond tension. Considering these results, it was concluded that frost damage can have a significant influence on the bond behavior, even if the damage is limited to the concrete cover and has not progressed to the concrete surrounding the reinforcing steel. The maximum bond tension can be reduced considerably if there is even slight damage in the concrete cover.

Hanjari *et al.* (2011) also conducted pull-out tests designed to investigate the effects of frost damage on the local bond-slip relationship. It was noted that pull-out failure occurred at steel stresses below the yield strength, and the failure mode was identified as shear sliding along the perimeter of the reinforcing steel. From the average bond stress-slip response of the reference specimen and specimens with frost damage level I and level II, it was found that the bond capacity is reduced by 14% and 50% for damage levels I and II, respectively. A decrease in the stiffness of the ascending branch of the bond-slip response was also observed with frost damage. Furthermore, as the level of frost damage increased, so did the slip at the maximum bond force. The slip at the maximum force for reference and damage levels I and II was 0.39, 0.48, and 0.60 mm, respectively.

Xu *et al.* (2017) investigated the bond behaviour of deformed steel bars in frost-damage concrete subjected to monotonic and reversed cyclical loading. The bond properties of specimens with varying strength grades and levels of frost damage were observed. The experimental results showed that for specimens of same strength grade, the initial bond stiffness, the maximum bond resistance and the remaining bond strength decreased as the number of freeze and thaw cycles applied to the specimens increased; the slip at peak bond, however, increased. Furthermore, the bond strength decay, the progressive acceleration of bond stiffness degeneration and the loss of energy dissipation capacity were observed for specimens of same strength grade but higher levels of frost damage. The authors also noted that for the same level of frost damage, specimens with higher concrete strength showed an increase in the initial bond stiffness, the slip at peak bond stress, the maximum bond resistance and the remaining bond strength.

2.5 Distribution of Frost Damage

Internal frost damage progresses from the surface into the concrete subjected to freeze-thaw cycles and is therefore unevenly distributed over the cross section of a structural element. Lohaus and Petersen (2002) carried out research to observe the influence of frost deterioration on concrete properties. The data from their experimental work was adapted and is presented in Figure 2.6. It shows the distribution of the internal damage expressed as relative dynamic modulus of elasticity at various distances from the surface in relation to the number of freezing and thawing cycles. The extension and distribution of the damage shows that the exposed concrete surface is most severely affected. The damage lessens as the distance from the freeze-thaw stressed surface increases.

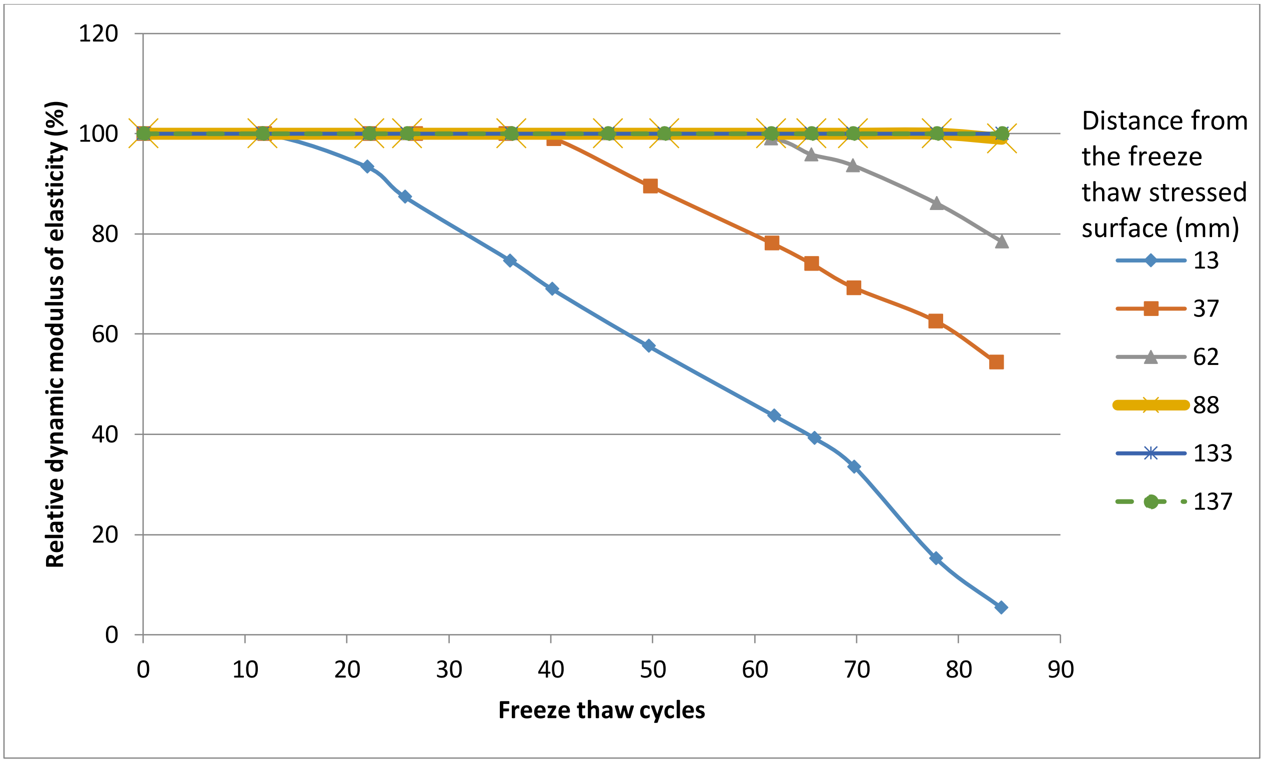

Figure 2.6. Distribution of internal damage in a specimen (reproduced from Petersen *et al.* 2007)

2.6 Effect of Frost Damage on Structural Behaviour of Reinforced Concrete Members

In an experimental study by Qin *et al*. (2017), the influence of freeze-thaw cycles on the seismic behavior of reinforced concrete columns was investigated. The authors analysed the effects of the numbers of freeze-thaw cycles on the failure modes, hysteretic response, and skeleton curves of the specimens. It was observed that freeze-thaw cycles did not affect the failure mode of the columns as all specimens failed due to bending. Furthermore, the authors visually observed uneven distribution of frost damage in the outer and inner part of the columns. It was also noted that the hysteretic response of specimens subjected to different degrees of frost damage was similar. The load bearing capacity of specimens decreased gradually with the increase of freeze-thaw cycles; there was, however, a slight increase in displacements for different damage degrees, and a gradual decline in the corresponding ductility factors; see Table 2.1 and Figure 2.7.

Table 2.1. Force and deformation of the tested columns (reproduced from Qin *et al.* 2013)

Specimen	Cycles	F_y (kN)	Δ_y (mm)	F_{max} (kN)	Δ_{max} (mm)	F_u (kN) ($0.85F_{max}$)	Δ_u (mm)	Δ_u/Δ_y
Z-C1	0	55.99	7.26	66.92	14.42	56.88	38.45	5.30
Z-C2	100	50.55	7.14	60.60	14.58	51.51	44.03	6.16
Z-C3	200	47.65	7.40	56.47	14.6	48.00	44.48	6.01
Z-C4	300	47.20	8.50	54.42	14.28	46.26	42.64	5.02

Note: F_y and Δ_y are the yield load and displacement; F_{max} and Δ_{max} are the peak load and displacement; F_u and Δ_u are the ultimate load and displacement; Δ_u/Δ_y is the displacement ductility coefficient.

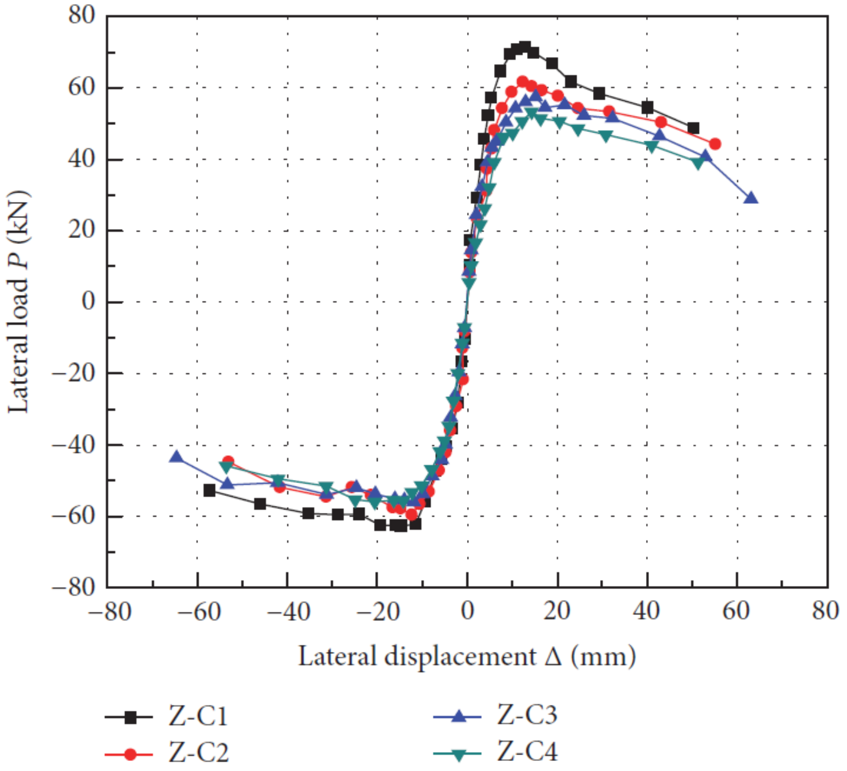

Figure 2.7. Experimental skeleton curves (reproduced from Qin *et al.* 2013)

Hassanzadeh and Fagerlund (2006) studied the structural effects of the internal frost damage on large reinforced concrete beams by subjecting them to frost damage. Freeze-thaw cycles in combination with high degree of saturation induced internal cracks in the reinforced concrete beams. Results from the experimental tests showed that internal frost damage not only caused loss of strength but also caused reduction of the stiffness and extensive visible cracking. In some cases, frost damage also affected the failure mode of the beams. For instance, frost-damaged beams that were designed to fail due to yielding of the reinforcement instead failed as a result of the compression crushing of concrete. Furthermore, the authors noted that given the level of deterioration, the remaining load-bearing capacity of the beams was remarkably high.

The investigation also showed that when the saturation degree was above the critical value and the structural element experienced freeze-thaw cycles, the damage was severe and caused dramatic reduction of the load-bearing capacity and stiffness of the structural member. In practice, however, unless very high moisture conditions are reached in the structure, internal frost damage increases gradually.

2.7 Modeling the Behaviour of Frost-Damaged Concrete

Nili *et al*. (2017) proposed an analytical model for predicting frost damage of concrete exposed to freeze-thaw cycles with one parameter that can be identified on the stress-strain curve of a uniaxial tension test. Results from a sample of 55 experimental tests were used to compare and validate the authors' propositions and analytical results. It was shown that the proposed model can serve as an effective tool to evaluate concrete deterioration due to frost damage. However, this development is only applicable to normal concrete with water-cement ratio of 0.4–0.5 without any air-entraining agents or pozzolanic materials. Investigating the frost damage model of other types of concrete is required to be undertaken as the focus of further research.

Berto *et al*. (2015) reformulated the coupled mechanical-environmental damage model developed previously by the authors and proposed a freeze and thaw degradation model that had the capacity of better simulating the different aspects of the physical phenomenon. The model introduced a relationship that accounts for the effects of frost damage on the tensile strength separately from the compressive strength. This allows for the various effects of frost degradation in relation to the tensile and compressive strength to be accurately simulated. The model was validated by simulating experimentally tested frost-damaged beams. The simulations of a number of four-point bending tests of reinforced concrete beams subjected to frost degradation accurately reproduced the failure load, ultimate displacement, and failure mode. The model was concluded to be a reliable numerical tool for analysis of reinforced concrete structures subjected to freeze-thaw cycles.

Methodologies presented in the literature to model the effects of internal frost damage have been done on the premise that the effects of internal frost damage can be modelled as changes in material and bond properties. In one study, Hanjari *et al.* (2013) proposed a methodology to predict the damage caused by freeze-thaw cycles in terms of mechanical behaviour. The following is a discussion on the suggestions that were made on how to account for the changes in the material properties of frost-damaged concrete.

2.7.1 Stress-Strain Response of Frost-Damaged Concrete in Compression

To take the effects of frost damage into account, Hanjari *et al.* (2013) proposed modifications to a model by Thorenfeldt *et al*. (1987) for the stress-strain relationship of undamaged concrete. With the modifications, it is suggested that the model can be used for frost-damaged concrete, and it is as follows:

$$\sigma = f_c^d \left(\frac{\epsilon}{\epsilon_{c,p}^d}\right)\left(\frac{n}{n-1+\left(\frac{\epsilon}{\epsilon_{c,p}^d}\right)^{nk}}\right) \tag{2.6}$$

where σ and ϵ are the stress and strain in the concrete, respectively. The *n* and *k* correction factors are calculated using the following equations

$$n = \frac{E_c^d}{E_c^d - E_0^d} \tag{2.7}$$

$$k = \begin{cases} 1 & \text{For } 0 < \epsilon < \epsilon_{c,p}^d \\ 0.67 + \frac{f_c^d}{62} & \text{For } \epsilon > \epsilon_{c,p}^d \end{cases} \tag{2.8}$$

where E_c^d and E_0^d are the secant and tangential elastic modulus of the damaged concrete, respectively.

The curves in Figure 2.8 provide estimation for the strain at the maximum stress and the tangential elastic modulus of the damaged concrete based of the dynamic modulus of elasticity, respectively. The secant elastic modulus is calculated as$f_c^d/\epsilon_{c,p}^d$.

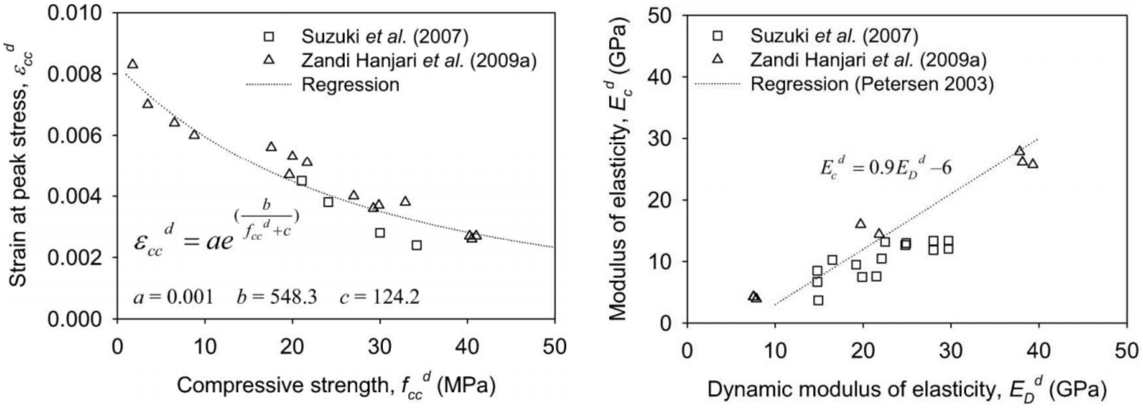

(a) (b)

Figure 2.8. An approximation of (a) strain at maximum stress and (b) the tangential elastic modulus of the damaged concrete based on the dynamic modulus of elasticity (reproduced from Hanjari *et al.* 2013)

Li *et al.* (2017) also accounted for frost damage by modifying the stress-strain relationship proposed by Zhenhai *et al*. (2003) for undamaged concrete. A parameter to account for the frost damage was introduced. The relationship is as follows:

$$y = \frac{\sigma}{f_c^d} = \begin{cases} a_d x + (3 - 2a_d)x^2 + (a_d - 2)x^3 & \text{For } 0 \leq x = \frac{\epsilon}{\epsilon_{c,p}^d} \leq 1 \\ \dfrac{x}{b_d(x-1)^2 + x} & \text{For } x = \frac{\epsilon}{\epsilon_{c,p}^d} > 1 \end{cases} \tag{2.9}$$

where a_d and b_d in the above equation reflect the "compaction effect" during the ascending branch of the stress-strain response and the post-peak behaviour, respectively. Parameters a_0 and b_0 are special cases of a_d and b_d, respectively, where the number of freeze-thaw cycles is 0. The values of a_d and b_d of concrete prisms with different damage degrees were collected from previous works and plotted in the forms of a_d/a_0 and b_d/b_0 in relation to *RCS*.

Through curve fitting, the following relations are established to calculate a_b and b_d:

$$a_d/a_0 = \begin{cases} 2.2268\, f_c^d/f_c - 1.2268 & \text{For } 0.6 \le f_c^d/f_c \le 1 \\ 0.1093 & \text{For } f_c^d/f_c < 0.6 \end{cases} \tag{2.10}$$

$$b_d/b_0 = \begin{cases} -3.395\, f_c^d/f_c + 4.395 & \text{For } 0.6 \le f_c^d/f_c \le 1 \\ 2.358 & \text{For } f_c^d/f_c < 0.6 \end{cases} \tag{2.11}$$

2.7.2 Stress-Crack Opening Relation of Frost-Damaged Concrete in Tension

A bi-linear relationship between tensile stress and crack opening shown in Figure 2.9 was proposed by Hanjari *et al*. (2011); the results from the wedge splitting test were used for an inverse analysis in order to determine the $\sigma_{ct} - w$ relationship. The wedge splitting test results showed an increase in the fracture energy due to frost damage. This is because several cracks were introduced by freeze-thaw cycles prior to mechanical testing and so, greater energy was dissipated, by opening several dominant cracks, to fully fracture the specimen. The tensile stress–crack opening relation, $\sigma_{ct} - w$, shows a very large ultimate crack opening. The bi-linear relationship can be used in numerical analyses of frost-damaged reinforce concrete elements.

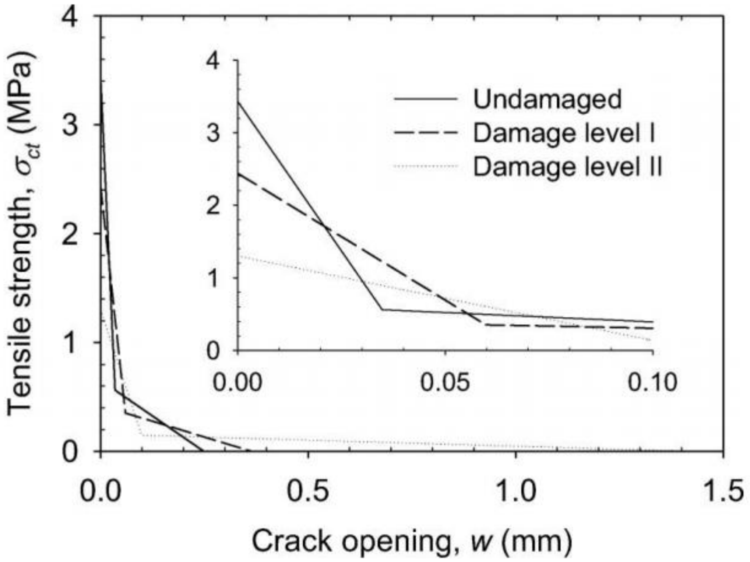

Figure 2.9. Bi-linear relationship between tensile stress and crack opening (reproduced from Hanjari *et al.* 2013)

2.8 Frost Damage Mitigation Measures

Since the 1930s, entrained air was found to increase greatly the concrete resistance against surface scaling by de-icing salts. Air entrainment has since become an efficient measure against frost damage of concrete used in environments with freezing and thawing.

CSA A23.1 - Concrete materials and methods of concrete construction/Test methods and standard practices for concrete stipulates that consideration must be given to the exposure conditions to which the concrete will be subjected. Exposure class F pertain to concrete exposed freezing and thawing without chlorides. Table 1 of the standard goes on to specify additional sub-classes of concrete exposure based on additional concrete exposure condition. Exposure classes F-1 and F-2 are defined as concrete exposed to freezing and thawing in a saturated condition, but not to chlorides, and concrete in an unsaturated condition exposed to freezing and thawing, but not to chlorides, respectively. The standard sets the requirement for air content, in Table 4, based on these various exposures.

2.9 Need for Research

The reliability of methods to assess concrete structures exposed to freeze-thaw cycles is of significant concern to asset managers as it affects the service life prediction of such structures.
Currently, existing Canadian standards for concrete structures do not provide explicit guidelines to evaluate the effect of frost damage over time to ensure the structures meet their design lifetime. Researching the effects of frost damage on concrete structures is essential for developing methods to effectively quantify and assess the impact of this deterioration mode on the structural capacity of concrete infrastructure. The development of these methods is imperative, now more than ever before, because of climate change. The IPCC (2001) has suggested that within the next century, average temperatures in North America will increase by 1.5℃ to 3.0℃. Under a higher emissions scenario, average North American temperatures could increase by 3.5–7.5℃ (IPCC, 2001). Changing temperatures and increased frequencies of freeze thaw cycles make Canada’s reinforced concrete structures more vulnerable to frost damage and so, there is a need to develop finite element methods for evaluating the residual load-carrying capacity of frost damaged concrete structures.

Chapter 3. Finite Element Modeling

3.1 Introduction

In this chapter, the methodology implemented to model frost damage in the finite element analysis of reinforced concrete structures is presented. The mechanical behaviour of concrete is modified, which allows for frost damage to be quantified and the structural response of frost-damaged reinforced concrete members to be understood.

3.2 Nonlinear Finite Element Analysis Software

VecTor2 is the nonlinear finite element software used in this study for the analysis of frost-damaged reinforced concrete members. The program was developed at the University of Toronto and predicts the response of reinforced concrete elements under in-plane normal and shear stresses. It is based on the Modified Compression Field Theory (Vecchio and Collins 1986) and the Disturbed Stress Field Model (Vecchio 2000). Cracked concrete is treated as an orthotropic material with smeared, rotating cracks. The program implements displacement-based finite element methods by generating the structure stiffness matrix and relating the unknown nodal displacements to specified forces. Figure 3.1 illustrates the VecTor2 algorithm for nonlinear finite element analysis. VecTor2 was selected as the nonlinear finite element software to be used for the purposes of this work, because it offers nonlinear models for reinforced concrete with the analytical capabilities of finite element analysis. It also offers constitutive models for a variety of phenomena including compression softening, tension stiffening, and tension softening.

3.3 Finite Element Model

The VecTor2 element library includes planar triangular, rectangular and quadrilateral elements for modeling concrete with or without smeared reinforcement, linear truss bar element for modeling discrete reinforcement and link and contact elements for modeling bond-slip.

Concrete was modeled using the plane-stress rectangle. It is a four-node element and has eight degrees of freedom; each node translates in the x and the y directions. The orientation of the element is parallel to the x and the y axis. The element can be of any width or height; however, the accuracy of the solution is compromised when its dimensions deviate from a square. The maximum aspect ratio was, therefore, specified to be 1.5.

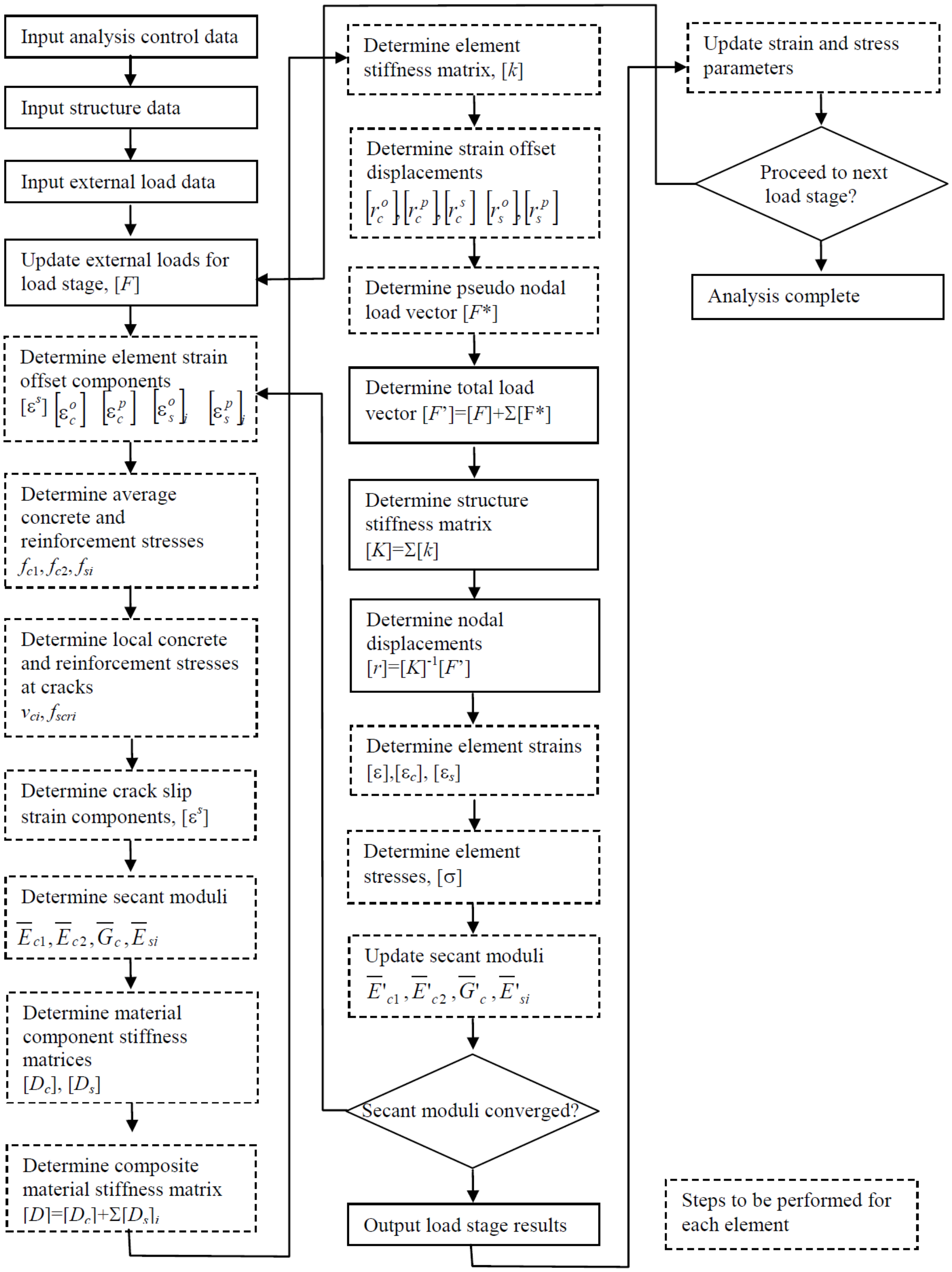

Figure 3.1. VecTor2 algorithm for nonlinear finite element analysis (reproduced from VecTor2 manual)

Steel reinforcement can be modeled as either smeared or embedded in the VecTor2 program. The use of smeared reinforcement is appropriate for cases where the longitudinal or transverse bars are sufficiently well distributed. Although this technique produces results with an acceptable level of accuracy, it does not allow for modeling the bond behaviour between the steel and concrete. The use of discrete truss elements is necessary in cases where bond-slip of reinforcement is to be considered. The truss element is a two-node element with four degrees of freedom, and it was used here to model both the longitudinal and transverse steel reinforcement.

In regions where bond stresses are low, the change in reinforcement strain, during loading, is equivalent to the change in total concrete strain; perfect bond can therefore be assumed. However, in regions where high reinforcement stresses result in large bond stresses, the consideration of bond action is critical. These large bond stresses facilitate imperfect bond action. VecTor2 allows for modeling imperfect bond through the use of bond elements. These elements eliminate the perfect bond relationship between the steel and concrete by acting as a deformable interface between concrete and discrete reinforcement elements. The link element was used across the concrete and reinforcement interface to model the influence of localized bond-slip on the load-deformation response of frost-damaged reinforced concrete beams. Figure 3.2 shows a typical finite element mesh.

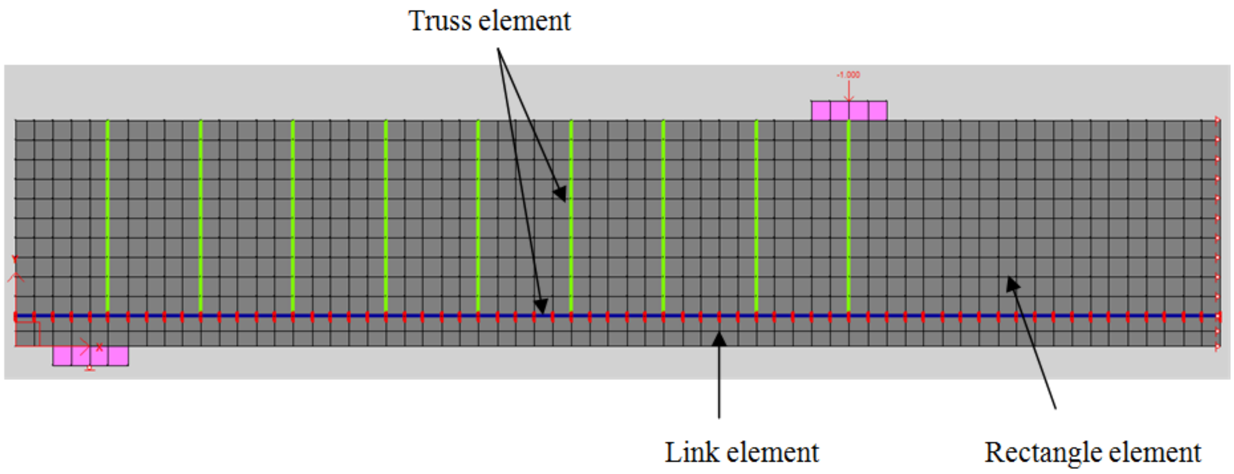

Figure 3.2. Typical finite element mesh

3.4 Modeling Frost Damage

The degree and the extent of damage in concrete due to successive freeze-thaw cycles are constituted by the concrete microstructure (porosity, degree of saturation, etc.) and environmental factors (freezing rate and duration, amplitude of temperature, etc.). The successive freezing and thawing of water within concrete's pore system introduces micro and macro cracks and changes the internal structure of the concrete. Internal frost damage was, therefore, modeled as a change in the mechanical behaviour, which relates to the material properties and bond behaviour of frost damaged concrete. The damage caused by freezing of concrete in the presence of a chloride solution causes surface scaling and was modeled as a reduction of the concrete cover. Figure 3.3 below illustrates the parameters considered in simulating internal frost damage and surface scaling.

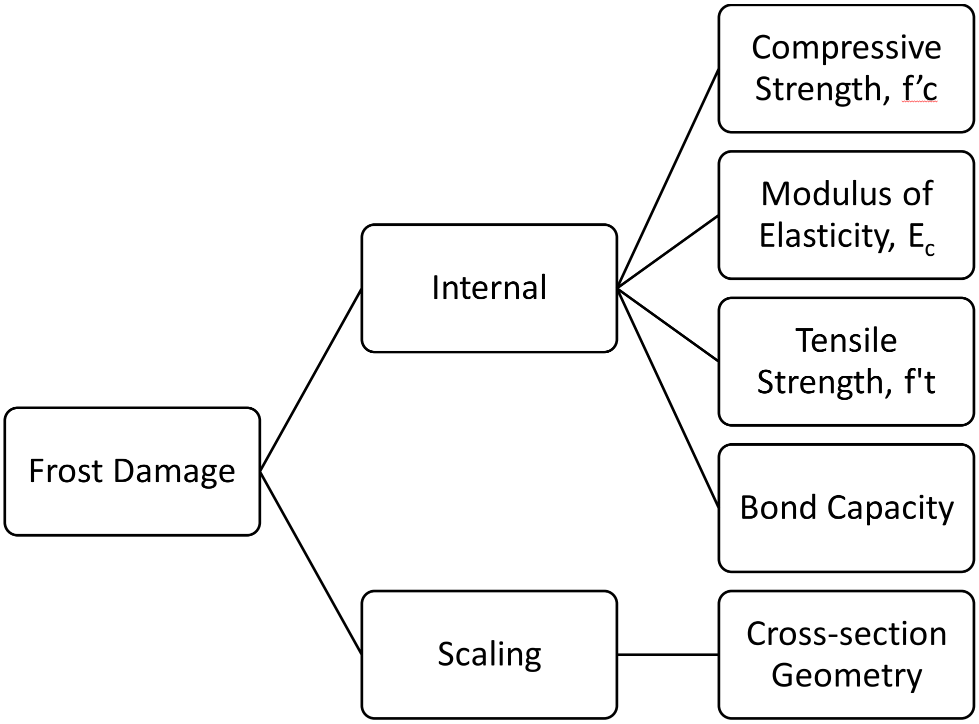

Figure 3.3. Parameters modified to simulate frost damage

3.4.1 Mechanical Properties

The material properties of frost-damaged concrete were used as input for the analysis. Consequently, the mechanical behaviour of concrete was modified to simulate frost damage.

To assess deterioration in a concrete structure at any given time, the measured compressive strength is required as an indicator of the damage. Core samples of the concrete specimen must undergo compression strength testing in the process of evaluating the damaged compressive strength, f_c^d. Once the compressive strength of the frost-damaged concrete, f_c^d is determined, it can be related to the other mechanical properties of the frost-damaged concrete, including modulus of elasticity, E_c^d, and tensile strength, f_t^d.

The relationship between compressive strength of undamaged concrete, f_c, and its mechanical properties have been established and are used in the analysis and design of concrete structures. In an attempt to establish relationships of the same nature for frost-damaged concrete, authors including Li (2017) compiled and analysed experimental data from various research programs.

Li (2017) noted that data from the different experimental studies used specimens with varying geometry and freeze-thaw exposure in their respective controlled environments. Establishing the relationships between compressive strength and other mechanical properties for frost-damaged concrete from regression analysis would require the conversion of experimental data obtained from different research programs and would not be feasible. To overcome this, Li (2017) adopted dimensionless mechanical properties (relative elastic modulus, relative tensile strength, etc.) and related them to the relative compressive strength. The following are the relationships the author proposed for frost-damaged concrete.

$$E_c^d = \frac{10^5}{2.2 + 2.64/f_c}\left(1.4238\frac{f_c^d}{f_c} - 0.4238\right) \tag{3.1}$$

$$f_t^d = 0.302 f_c^{\frac{2}{3}}\left(1.04125\frac{f_c^d}{f_c} - 0.04125\right) \tag{3.2}$$

3.4.2 Bond Capacity

For modeling the effects of frost damage on reinforced concrete structures, the perfect bond assumption of the MCFT is not appropriate as experimental studies have shown that frost damage influences bond strength. The stress-slip response of the bond elements is governed by the bond stress-slip curve. In order to account for the reduction in bond capacity and the subsequent modifications to the internal stress distribution and load-deformation response, the bond stress-slip relation proposed by Eligehausen *et al.* (1983) was modified to incorporate frost-damage effects. The Eligehausen bond stress-slip curve is defined by a non-linear ascending branch followed by a plateau, a linear descending branch and final a residual stress branch, as illustrated in Figure 3.4.

The bond model determines the stress-slip relationship for two distinct cases: confined bars and unconfined bars. The relationship for confined bars corresponds to pullout type bond failure, and the relationship for unconfined bars corresponds to splitting failure. Both the confined and unconfined bond stress-slip relationships are defined by a series of reference bond stresses, τ, and bond slips, Δ. Those pertaining to pullout failure are subscripted as $\tau_p,\ \Delta_p$, while those pertaining to splitting failure are subscripted, τ_s, Δ_s. The actual bond stress-slip model is defined by a series of reference bond stresses and slips, $\tau_{sp},\ \Delta_{sp}$ that are determined by linearly interpolating between the unconfined and confined reference bond stresses and slips.

The confined stress-slip relationship is as follows:

$$\tau = \begin{cases} \tau_{p1}\left(\frac{\Delta}{\Delta_{p1}}\right)^{\alpha} & for \Delta \leq \Delta_{p1} \\ \tau_{p2} & for\ \Delta_{p1} < \Delta \leq \Delta_{p2} \\ \tau_{p2} - \left[\frac{(\Delta - \Delta_{p2})}{(\Delta_{p3} - \Delta_{p2})}(\tau_{p2} - \tau_{pf})\right] & for\ \Delta_{p2} < \Delta \leq \Delta_{p3} \\ \tau_{pf} & for\ \Delta_{p3} < \Delta \end{cases} \tag{3.3}$$

where

$$\tau_{p1} = \left(20 - \frac{d_b}{4}\right)\sqrt{\frac{f_c}{30}} \tag{3.4}$$

$$\tau_{p2} = \tau_{p1} \tag{3.5}$$

$$\tau_{pf} = \left(5.5 - 0.07\frac{S}{H}\right)\sqrt{\frac{f_c}{27.6}} \tag{3.6}$$

$$\Delta_{p1} = \sqrt{\frac{f_c}{30}} \tag{3.7}$$

$$\Delta_{p2} = 3.0\ mm \tag{3.8}$$

$$\Delta_{p3} = S \tag{3.9}$$

$$\alpha = 0.4 \tag{3.10}$$

where S is the lug spacing, H is the lug height, and d_b is the reinforcement bar diameter.

The unconfined stress-slip relationship is as follows:

$$\tau = \begin{cases} \tau_{s1}(\frac{\Delta}{\Delta_{s1}})^{\alpha} & for \Delta \leq \Delta_{s1} \\ \tau_{s2} & for\ \Delta_{s1} < \Delta \leq \Delta_{s2} \\ \tau_{s2} - \left[\frac{(\Delta - \Delta_{s2})}{(\Delta_{s3} - \Delta_{s2})}(\tau_{s2} - \tau_{sf})\right] & for\ \Delta_{s2} < \Delta \leq \Delta_{s3} \\ \tau_{sf} & for\ \Delta_{s3} < \Delta \end{cases} \tag{3.11}$$

where

$$\tau_{s1} = 0.748\sqrt{\frac{f_c \cdot c}{d_b}} \leq \tau_{p1} \tag{3.12}$$

$$\tau_{s2} = \tau_{s1} \tag{3.13}$$

$$\tau_{sf} = 0.234\sqrt{\frac{f_c \cdot c}{d_b}} \leq \tau_{pf} \tag{3.14}$$

$$\Delta_{s1} = \Delta_{p1}\exp\left[\frac{1}{\alpha}\ln\left(\frac{\tau_{s1}}{\tau_{p1}}\right)\right] \tag{3.15}$$

$$\Delta_{s2} = \Delta_{p2} \tag{3.16}$$

$$\Delta_{s3} = \Delta_{p3} \tag{3.17}$$

where c is the minimum concrete cover.

Modifications were made to the Eligehausen bond stress-slip relationship according to the subsequent discussion in order to define a multilinear relationship for frost-damaged concrete. Three reference bond stresses, τ_i, and corresponding slips, Δ_i, were used as input in VecTor2 to define the multilinear bond stress-slip relationship for frost-damaged concrete.

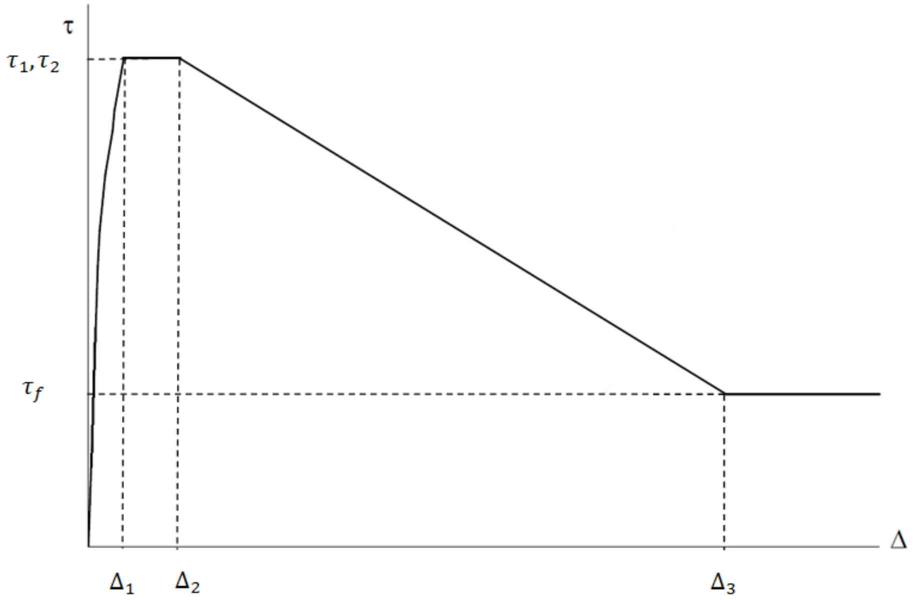

Figure 3.4. The Eligehausen bond stress-slip curve

Petersen *et al.* (2007) proposed the following relationship which relates the variation in the maximum bond stresses to the relative dynamic modulus of elasticity, $E_{D,rel}^{d}$. Frost damage is quantified with the relative dynamic modulus of elasticity in the proposed relationship.

$$\tau_{max}^{d} = \left(0.17 + 0.007\, E_{D,rel}^{d}\right)\tau_{max} \tag{3.18}$$

where τ_{max}^{d} is the maximum bond strength for damaged concrete, $\tau_{max}$is the maximum bond strength for undamaged concrete, and $E_{D,rel}^{d}$ is the relative dynamic modulus of elasticity for damaged concrete, with values ranging from 40% to 100% (Petersen *et al.* 2007).

The reference stress, τ_1, defining the multilinear bond stress-slip relationship for confined frost-damaged concrete was then determined according to the following:

$$\tau_1 = \left(0.17 + 0.007\ E_{D,rel}^{d}\right)\tau_{p1} \tag{3.19}$$

where τ_{p1} is calculated from Eq. 3.4.

For unconfined concrete, the reference stress, τ_1, that defines the multilinear bond stress-slip relationship is determined as follows:

$$\tau_1 = \left(0.17 + 0.007\ E_{D,rel}^{d}\right)\tau_{s1} \tag{3.20}$$

where τ_{s1} is obtained from Eq. 3.12. The reference stress,τ_2, was defined as per the Eligehausen bond stress-slip curve:

$$\tau_2 = \tau_1 \tag{3.21}$$

The following relationship was proposed by Hanjari (2013) to determine the residual bond strength, τ_f, which is reduced proportionally to the reduction in the bond capacity.

$$\tau_f^d = \left(\frac{\tau_{max}^d}{\tau_{max}}\right)\tau_f \tag{3.22}$$

For confined concrete, the reference stress, τ_3, defining the multilinear bond stress-slip relationship, is then determined as follows:

$$\tau_3 = \left(\frac{\tau_1}{\tau_{p1}}\right)\tau_{pf} \tag{3.23}$$

The reference stress, τ_3, for unconfined concrete is determined according to the following:

$$\tau_3 = \left(\frac{\tau_1}{\tau_{s1}}\right)\tau_{sf} \tag{3.24}$$

For confined concrete, Δ_1, Δ_2, and Δ_3 are calculated from Eqs. 3.7, 3.8 and 3.9, respectively. For unconfined concrete, Δ_1, Δ_2, and Δ_3 are calculated from Eqs. 3.15, 3.16 and 3.17, respectively. For a level of frost damage corresponding to ≈50% reduction in compressive strength, the values of the reference bond stresses, τ_1, τ_2, and τ_3 and corresponding slips, $\Delta_1 < \Delta_2 < \Delta_3$ defining the confined and unconfined multilinear bond stress-slip relationships for frost-damaged concrete are presented in Table 3.1. Figure 3.5 shows the confined and unconfined multilinear bond stress-slip relationships for both undamaged and frost-damaged concrete.

Table 3.1. Unconfined and confined reference bond stresses and corresponding slips to define multilinear bond stress-slip relationships

i	Confined		Unconfined	
	τ_i (MPa)	Δ_i (mm)	τ_i (MPa)	Δ_i (mm)
1	1.12	3.72	0.09	1.34
2	3	3.72	3.00	1.34
3	13.6	1.17	13.60	0.42

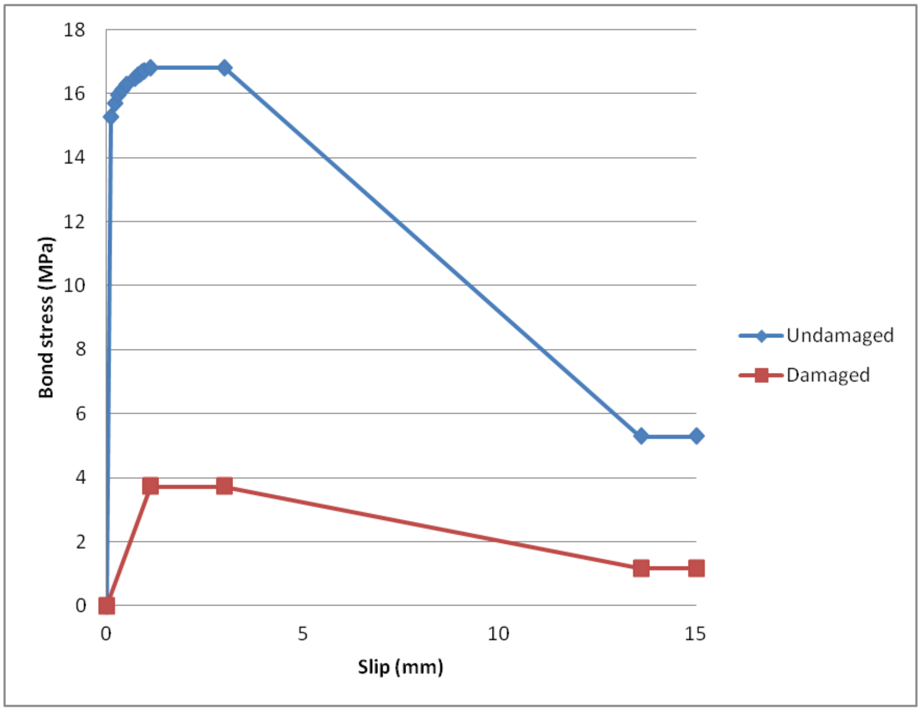

(a)

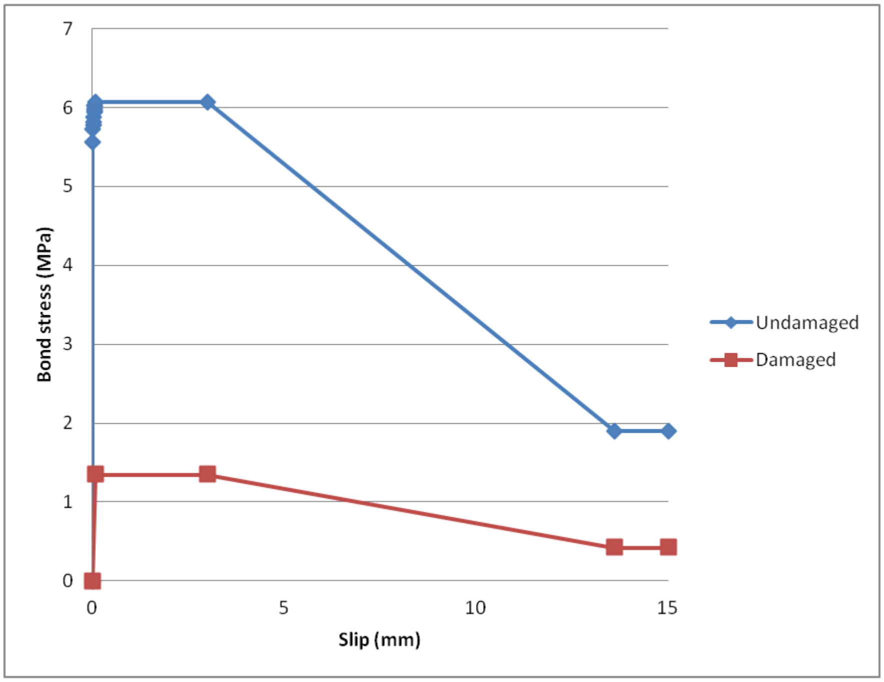

(b)

Figure 3.5. Bond stress-slip relationship for (a) confined bars and (b) unconfined bars

3.4.3 Surface Scaling

Scaling is a function of:

I. salt concentration
II. minimum temperature reached during a freeze-thaw cycle.

To estimate future salt scaling, Fagerlund (2005) proposed salt scaling tests, in which the surface of test specimens is exposed to freeze-thaw cycles in a salt solution. The weight loss is then measured.

It was stated that given undamaged concrete, the dry-weight loss per unit area, ΔQ (kg/m^2) can be expressed by the following linear relationship:

$$\Delta Q = K \times N \tag{3.25}$$

where K is the slope of the scaling curve, and N is the number of freeze-thaw cycles.

Results from an experimental study by Lindmark (1993) have been adapted and plotted in Figure 3.6. It was found that concrete with water-cement ratio of 0.4 has K=0.043 for a salt concentration of 3% NaCI-solution and for a minimum temperature of -22°C.

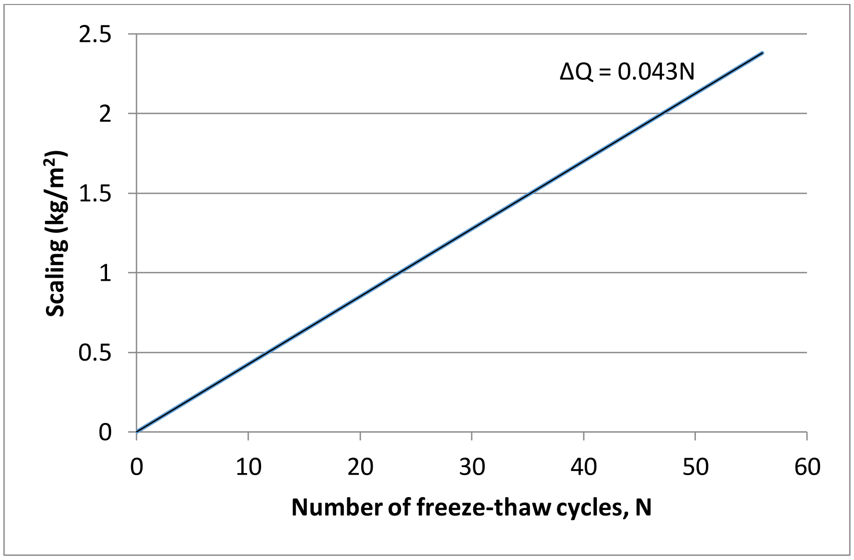

Figure 3.6. The effect of freeze-thaw cycles on salt scaling for a concrete with w/c = 0.4 (reproduced from Lindmark 1993)

The weight loss is translated to a scaling depth s (m), using the dry-bulk density, γ:

$$s = \frac{K \times N}{\gamma} \tag{3.26}$$

3.5 Constitutive Models for Concrete

Accounting for the behaviour of frost-damaged concrete through appropriate constitutive models is critical in simulating frost damage in reinforced concrete and obtaining an accurate representation of the load-carrying capacity. These behavioural models determine the stress and strain from which the structure stiffness is determined at each load step. Inclusion or exclusion of analysis models allow for the option of including relevant behaviours and omitting behaviours that are not applicable to the analysis. In this section, the investigation of constitutive models available in VecTor2 and their effect on the simulation of frost-damaged beams is presented. The effects of the input parameters on the constitutive models' ability to simulate frost-damaged beams is also investigated and presented in this section.

A flexure-governed frost-damaged beam, D1, and a shear-governed frost-damaged beam, D5, were used for the purpose of the investigation. These beams were tested as part of an experimental program carried out by Hassanzadeh and Fagerlund (2006). In the experimental program, frost damage was introduced to the beams through vacuum treatment for a week, followed by submerging them in water and then subjecting them to two freeze–thaw cycles (3 days at -20°C followed by 2 days submerged in water at room temperature). Frost damage in the form of cracking was observed after the first freeze-thaw cycle. Both beams have a span of 4.4 m. The cross section of the beams is 0.2 m by 0.5 m. The longitudinal reinforcement in the beams consists 4Ø20 longitudinal bars. Beam D1 has 28Ø8 stirrups with a shear span of 1.7 m. Beam D5 has 4Ø8 stirrups at each support to prevent the cracking of the beams due to the concentrated load at the support. Two concentrated loads were applied to the beams at a third of the span. The compressive strength of the concrete in the frost-damaged beams, f_c^d, was reported by the authors to be 17.5 MPa.

Figures 3.7 and 3.8 show the geometry and finite element mesh of the beams, respectively. Half of the beams were modeled due to symmetry of geometry, boundary conditions and loading.

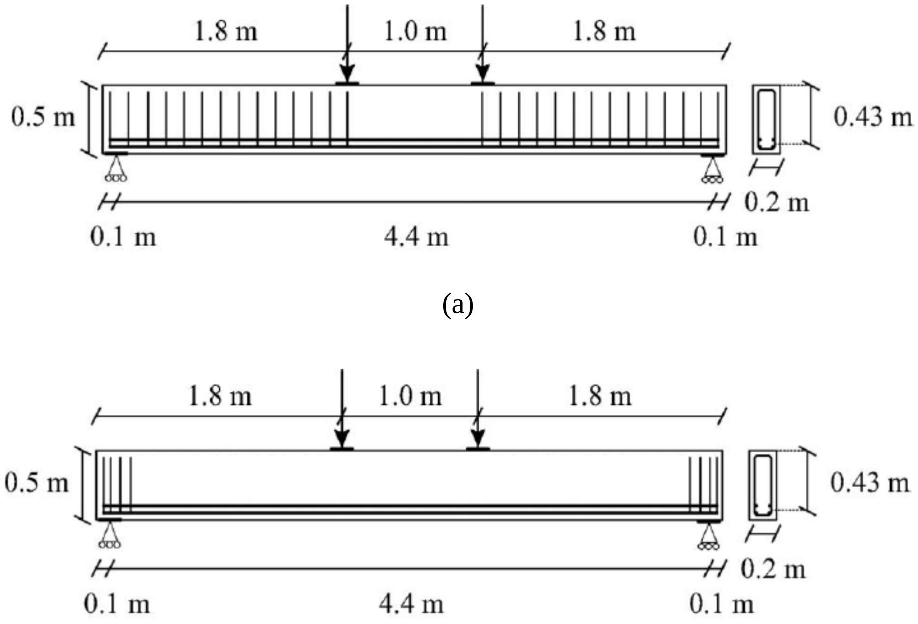

(a)

(b)

Figure 3.7. Geometry of beams (a) D1 and (b) D5 (reproduced from Hassanzadeh and Fagerlund 2006)

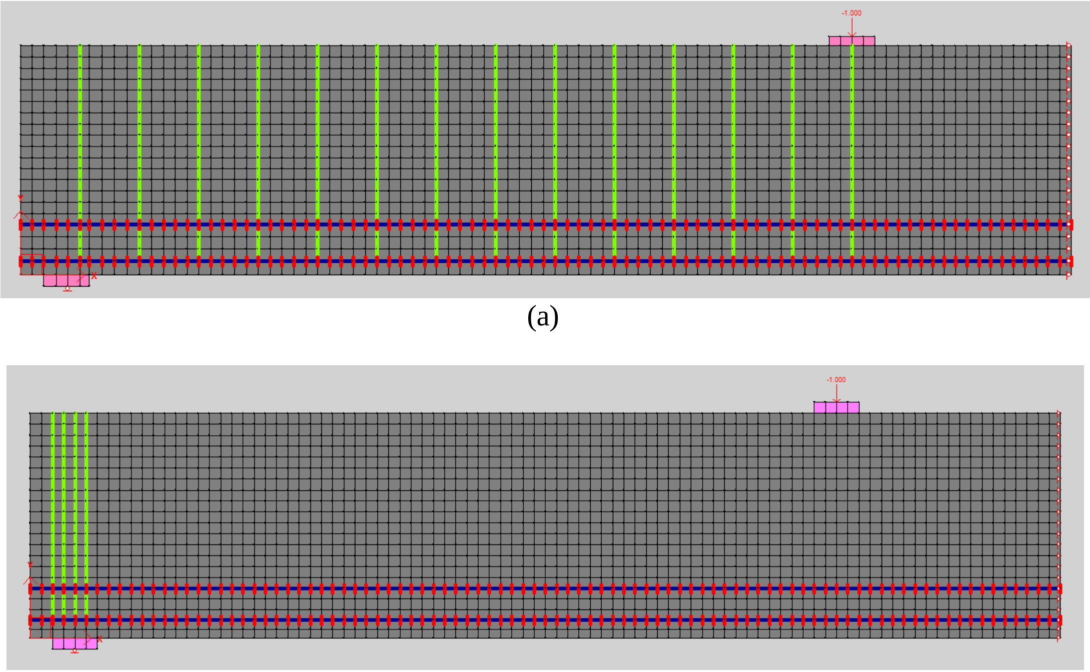

(a)

(b)

Figure 3.8. Finite element mesh of beams (a) D1 and (b) D5

3.5.1 Compression Response

VecTor2 offers various pre-peak and post-peak response models to be used in the analysis of reinforced concrete members. These models compute the principal compressive stress, f_{ci}, for the compressive principal strain, ε_{ci}. They determine the strain, ε_p, corresponding to the peak compressive stress, f_p, by adjusting the unconfined uniaxial concrete cylinder strength, f_c, and the corresponding strain, ε_o, for compression softening due to transverse tensile strains and strength enhancement due to confinement.

The Hognestad, Popovics and Smith-Young pre-peak response models and the effects of input parameters, including modulus of elasticity, E_c and tensile strength, f_t, on the load-deformation response of the beams using these models are explored in this section. The Hognestad stress-strain curve is defined by the following relationship:

$$f_{ci} = -f_p \left(2\left(\frac{\varepsilon_{ci}}{\varepsilon_p}\right) - \left(\frac{\varepsilon_{ci}}{\varepsilon_p}\right)^2 \right) < 0 \; for \; \varepsilon_{ci} < 0 \tag{3.27}$$

Formulation of the Popovics stress-strain curve is as follows:

$$f_{ci} = -\left(\frac{\varepsilon_{ci}}{\varepsilon_p}\right) f_p \left(\frac{n}{n-1+\left(\frac{\varepsilon_{ci}}{\varepsilon_p}\right)^{nk}} \right) < 0 \; for \; \varepsilon_{ci} < 0 \tag{3.28}$$

Parameters n and k diminish the difference between the initial tangent stiffness, E_c and secant stiffness, E_{sec} to account for increased linearity of higher strength concrete and increase the post-peak decay in stress, respectively. The following relationship defines the Smith-Young pre-peak curve:

$$f_{ci} = f_p \left(\frac{\varepsilon_{ci}}{\varepsilon_p}\right) \exp\left(1 - \left(\frac{\varepsilon_{ci}}{\varepsilon_p}\right)\right) \tag{3.29}$$

The modulus of elasticity, E_c, was varied according to the equation proposed by Li (2017) as well as the default value calculated by VecTor2 when E_c is not specified. According to the relationship proposed by Li (2017), E_c for frost-damaged concrete is determined using Eq. 3.1. Given that f_c and f_c^d for beams D1 and D5 were 37.6 MPa and 17.5 MPa, respectively, 8 GPa was used as input for E_c. In the absence of information, VecTor2 estimates E_c as $5{,}500\sqrt{f_c}$. For beams D1 and D5, this value is 23 GPa, which was also used as input in order to determine the effects of varying the concrete elastic modulus, E_c on the load deformation response of reinforced concrete beams.

Figures 3.9, 3.10 and 3.11 show the effects of varying E_c on the load-deformation response of flexure-governed beam, D1, simulated using Hognestad, Popovics and Smith-Young compression models, respectively. From these figures, it was noted that varying E_c significantly changes the initial stiffness of the load-deformation curve when the Hognestad and the Popovic models are used. The elastic modulus E_c estimated using the relationship proposed by Li (2017) provides a relatively accurate response of the beam, whereas the default value calculated by VecTor2 grossly overestimated the initial stiffness, and underestimated the load and deflection at failure. When the Smith-Young model is used, however, the load-deformation curve is not affected by the change in E_c; a reduction in E_c does not lead to a reduction of flexural stiffness.

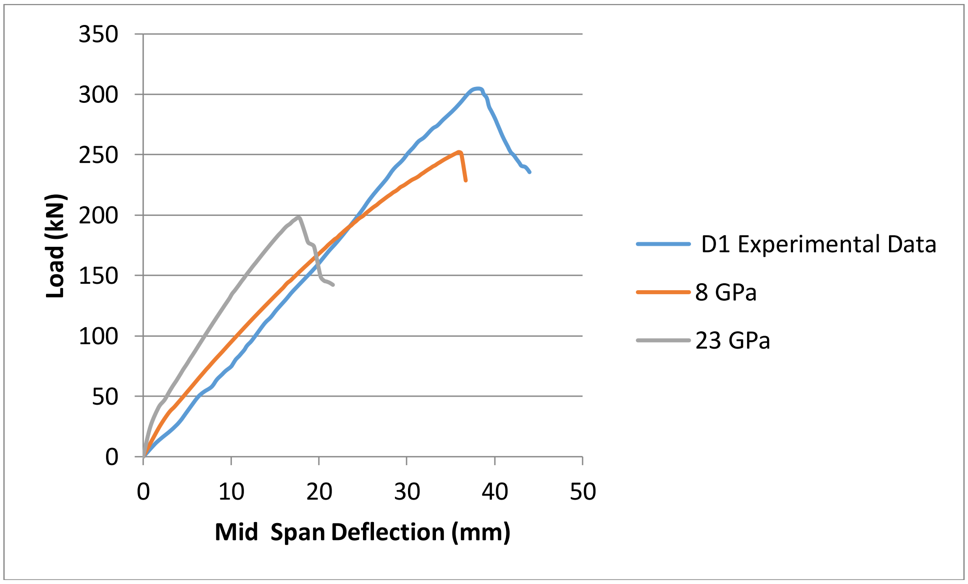

Figure 3.9. Effects of elastic modulus on the load deformation response of beam D1 using Hognestad model

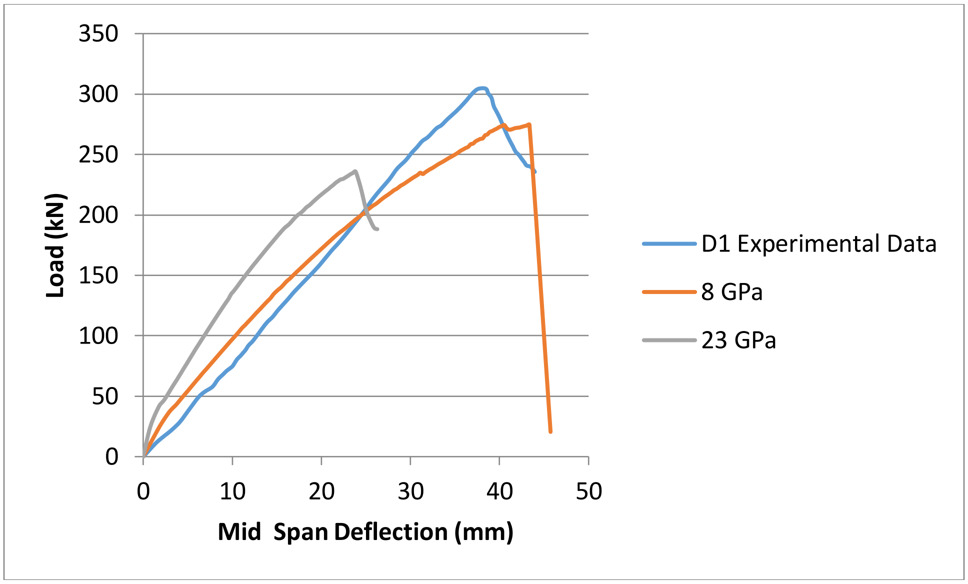

Figure 3.10. Effects of elastic modulus on the load deformation response of beam D1 using Popovic model

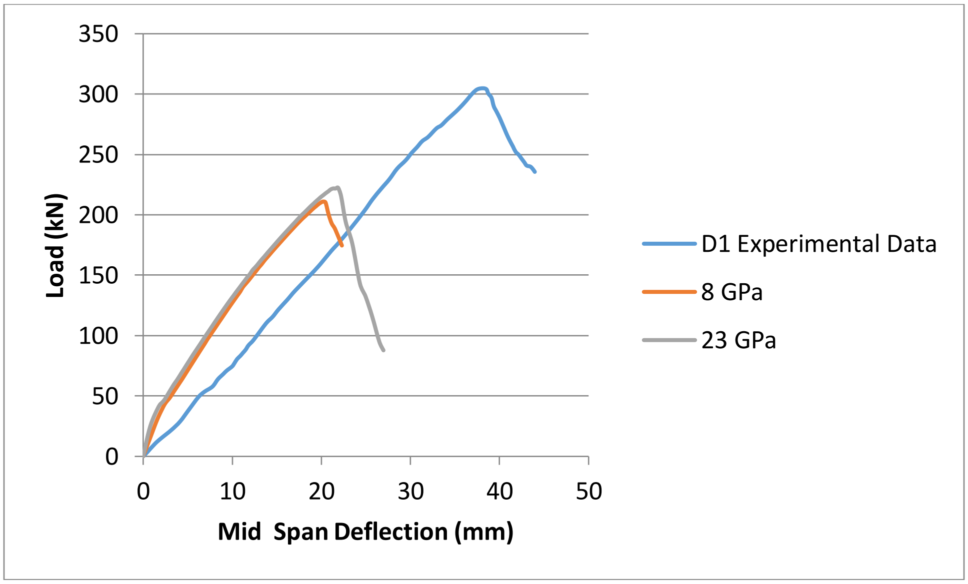

Figure 3.11. Effects of elastic modulus on the load deformation response of beam D1 using Smith-Young model

Figure 3.12 illustrates how the three models compare in predicting the load-deformation response of beam D1. Using the Smith-Young model in the analysis grossly underestimates the load and deflection at failure while overestimating the stiffness. The Hognestand and the Popovics response curves are almost identical in that the stiffness is the same. The load at failure is underestimated when both models are used, however, through the implementation of the Hognestad model, deflection at failure is more accurately represented; see Table 3.2. Therefore, the Hognestad stress-strain was selected to model the compression response of flexure-governed frost-damaged beams.

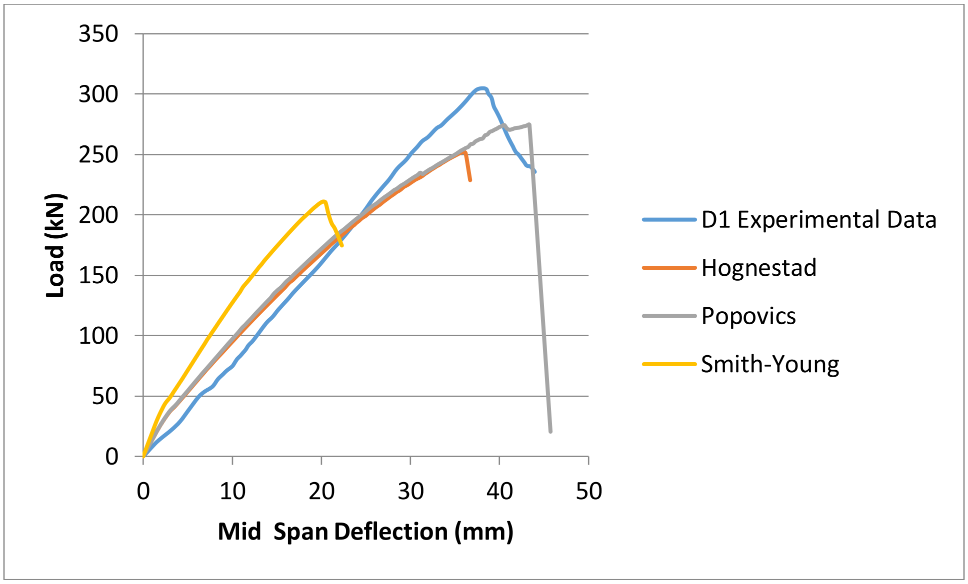

Figure 3.12. Effects of compression response models on load-deformation response of flexure-governed beam

Table 3.2. Comparison of beam D1 peak load and deflection at peak load predicted by FE analysis using various compression response models

Compression Response Model	P_{max} (kN)	P_{max} FE/Exp.	Δ_{max} (mm)	Δ_{max}FE/Exp.
Hognestad	252.26	0.83	35.92	0.94
Popovics	274.54	0.90	43.36	1.14
Smith-Young	211.02	0.69	20.20	0.53

The effects of varying E_c on the load-deformation response of shear-governed beam, D5, simulated using Hognestad, Popovics and Smith-Young compression models are shown in Figures 3.13, 3.14 and 3.15, respectively. As was seen in the response of beam D1, when the Hognestad and the Popovic models are used, varying E_c noticeably changes the initial stiffness of the load-deformation curve. However, when the Smith-Young model is used, the load-deformation curve is insignificantly affected by the change. From using the Hognestad and Popovics models, a relatively accurate response of the beam is generated when the value of E_c is given by the Li (2017) relationship. The value of E_c equivalent to the VecTor2 default value grossly overestimated the initial stiffness, as was also seen in the results for beam D1.

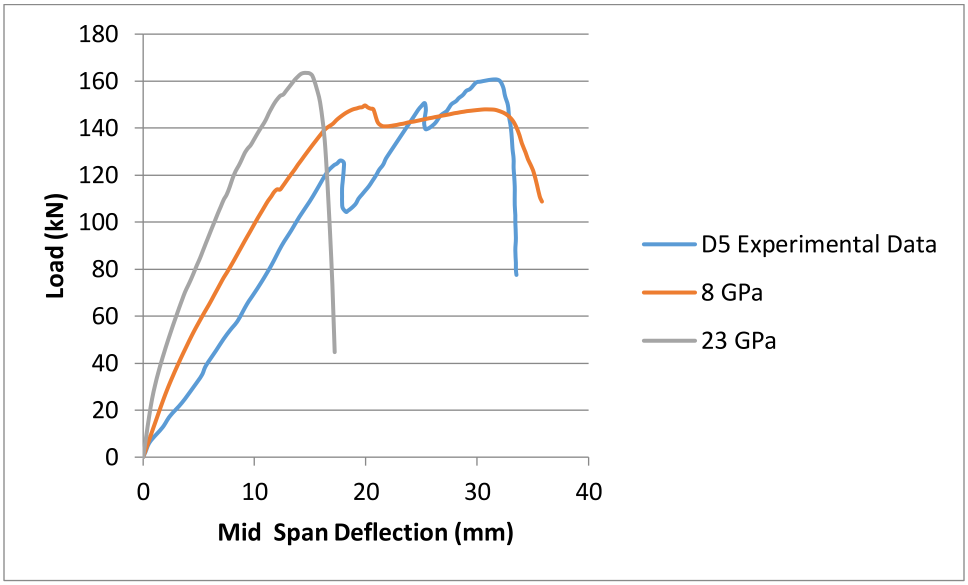

Figure 3.13. Effects of elastic modulus on the load-deformation response of beam D5 using Hognestad model

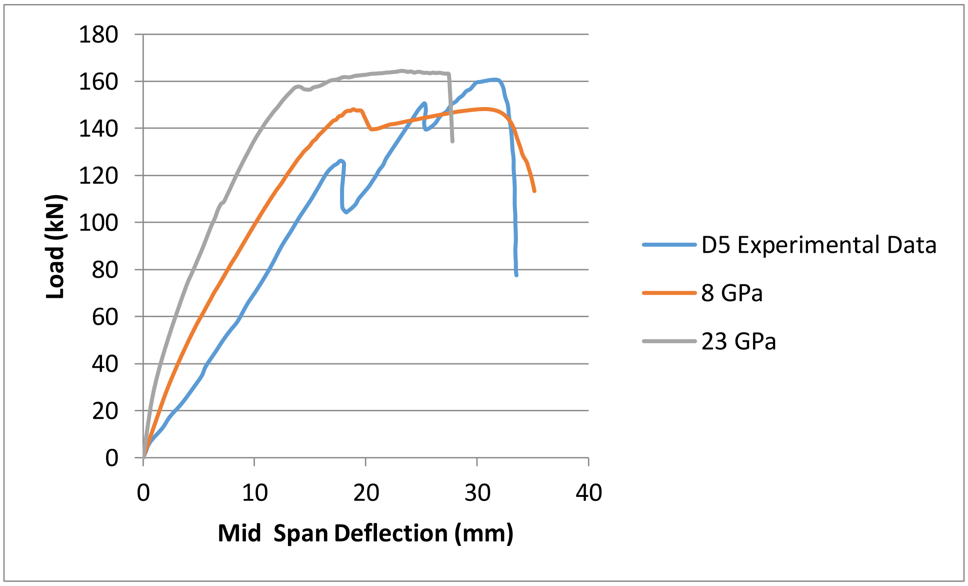

Figure 3.14. Effects of elastic modulus on the load-deformation response of beam D5 using Popovic model

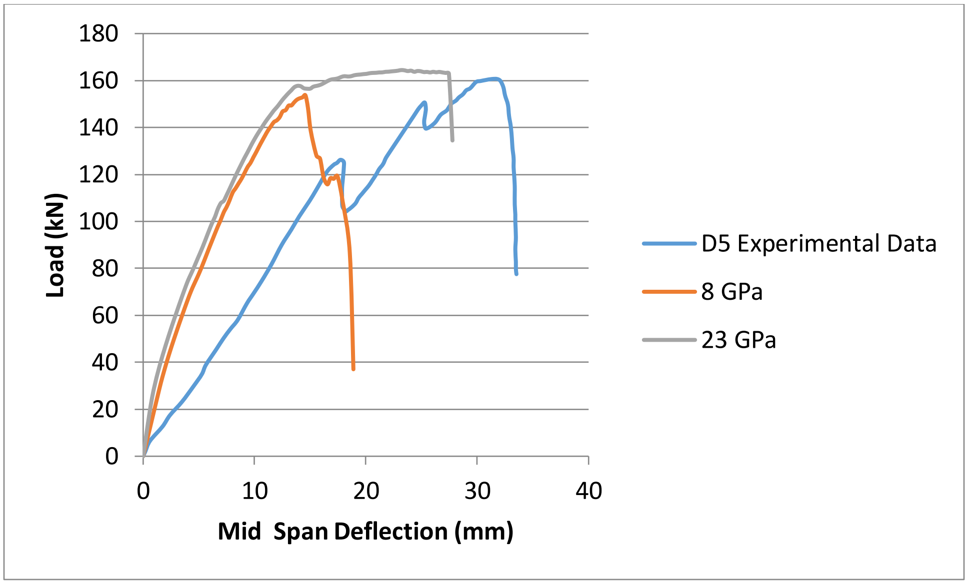

Figure 3.15. Effects of elastic modulus on the load-deformation response of beam D5 using Smith-Young model

The load-deformation curves for beam D5, using the different compression response models, is presented in Figure 3.16. As was observed from the response curves of beam D1 (Figure 3.12), the Hognestand and the Popovics load-deflection response is nearly identical; the curves show that the stiffness remains unchanged when either of the models is used. There is, however, a variation in the deflection at failure. With using both models, deflection is underestimated, but the Popovics model provides a slightly more accurate value of deflection at failure; see Table 3.3. In comparison with the curves generated using the Hognestand and the Popovics model, using the Smith-Young model reduces the deformation capacity of the beam and increases the stiffness significantly. For these reasons, the Popovics stress-strain curve was selected to model the compression response of shear-governed frost-damaged beams.

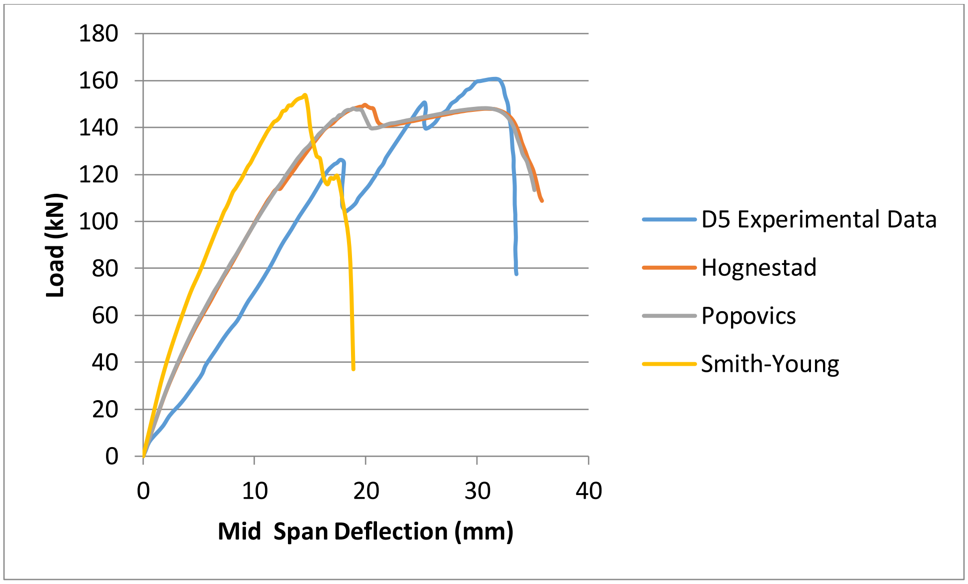

Figure 3.16. Effects of compression response models on load-deformation response of shear-governed beam

Table 3.3. Comparison of beam D5 peak load and deflection at peak load predicted by FE analysis using various compression response models

Compression Response Model	P_{max} (kN)	P_{max} FE/Exp.	Δ_{max} (mm)	Δ_{max}FE/Exp.
Hognestad	149.65	0.93	19.92	0.64
Popovics	148.23	0.92	30.59	0.98
Smith-Young	153.70	0.96	14.57	0.47

Similar to the elastic modulus, E_c, the tensile strength, f_t, was also varied in order to investigate the effects of this parameter on the load-deformation response of the beams using different compression response models. The authors of the experimental program, Hassanzadeh and Fagerlund (2006), reported a splitting tensile strength of 0.95 MPa for frost-damaged concrete and thus, it was used as an input for the analysis. Another input value was calculated from Eq. 3.2 proposed by Li (2017); according to the equation, 1.5 MPa is the approximated value for f_t that was used as an input.

Figures 3.17, 3.18 and 3.19 show the effects of varying f_t on the load-deformation response of flexure-governed beam, D1, simulated using Hognestad, Popovics and Smith-Young compression models, respectively. Varying f_t from 0.95 MPa to 1.5 MPa does not have significant impact on the load-deformation response when the different compression response models are used. Hence, the relationship proposed by Li (2017) is valid to use for determining the input parameter, f_t, when modeling flexure-governed frost-damaged concrete.

The effects of tensile strength on the load-deformation response using Hognestad model show no increase in stiffness for higher tensile strength, however, there is an increase in the load and deflection at failure. The same is not observed when effects of tensile strength on the load-deformation response using both the Popovics and Smith-Young models are considered. On the contrary, when the Popovics model is used, there is a decrease in deflection for higher tensile strength, while there is a decrease in both the ultimate strength and deflection when the Smith-Young model is used.

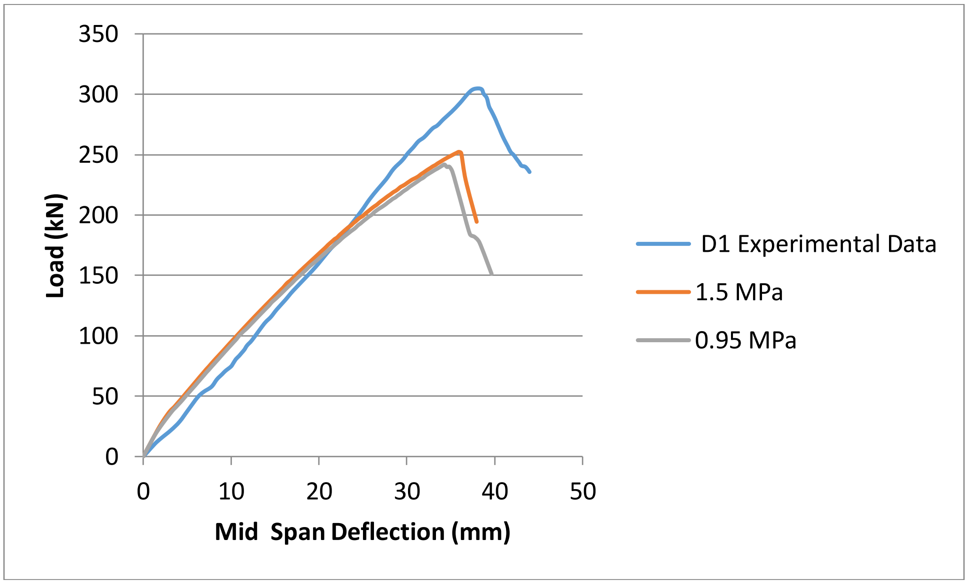

Figure 3.17. Effects of tensile strength on the load-deformation response of beam D1 using Hognestad model

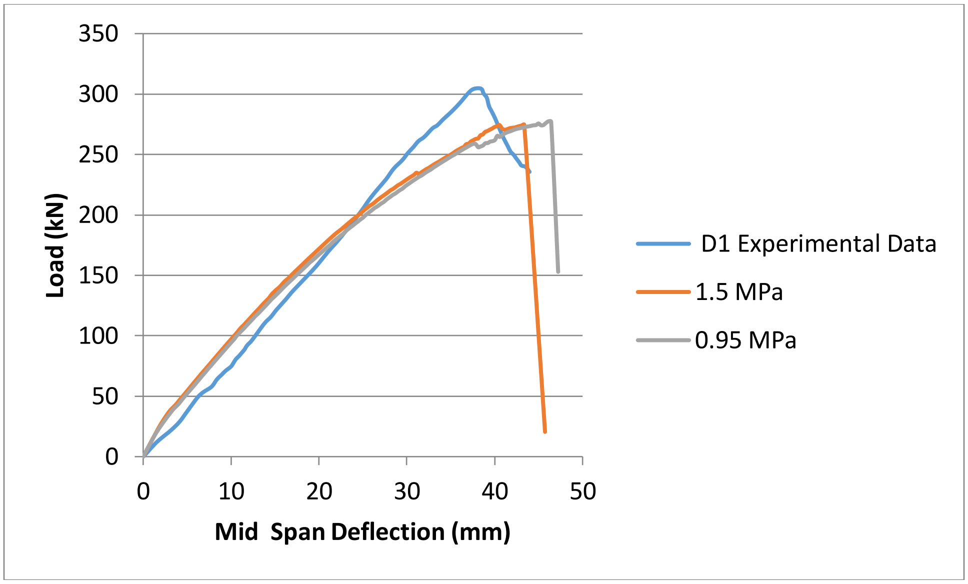

Figure 3.18. Effects of tensile strength on the load-deformation response of beam D1 using Popovic model

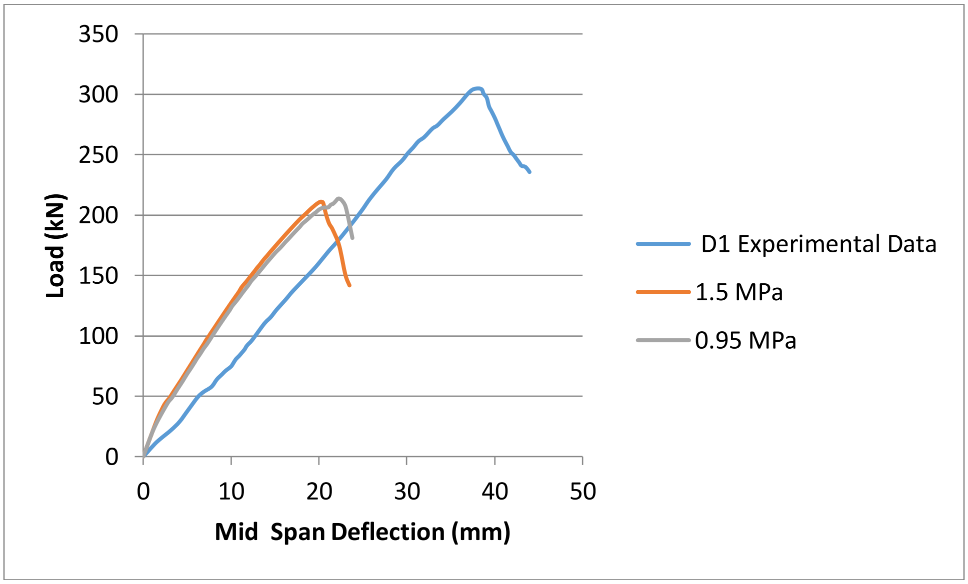

Figure 3.19. Effects of tensile strength on the load-deformation response of beam D1 using Smith-Young model

The effects of varying f_t on the load-deformation response of shear-governed beam, D5, simulated using Hognestad, Popovics and Smith-Young compression models are shown in Figures 3.20, 3.21 and 3.22, respectively. Similar to the results of the parametric analysis for beam D1, when f_t is varied, the impact on the load-deformation response is insignificant. Therefore, the relationship proposed by Li (2017) is again validated and can be used for determining the input parameter, f_t, when modeling frost-damaged beams.

The effects of tensile strength on the load-deformation response using both the Hognestad and the Popovics models show an increase in the load and deflection at failure for higher tensile strength. This increase is slightly larger than what was observed for beam D1, suggesting that shear-governed beams are more sensitive to this input parameter when the Hognestad model is used. The tensile strength f_t obtained from the splitting tensile test provides a better approximation of load at failure, but the deflection at failure is better estimated with the approximated f_t. However, when the Smith-Young model is used, the load-deformation curve is insignificantly affected by the change in f_t.

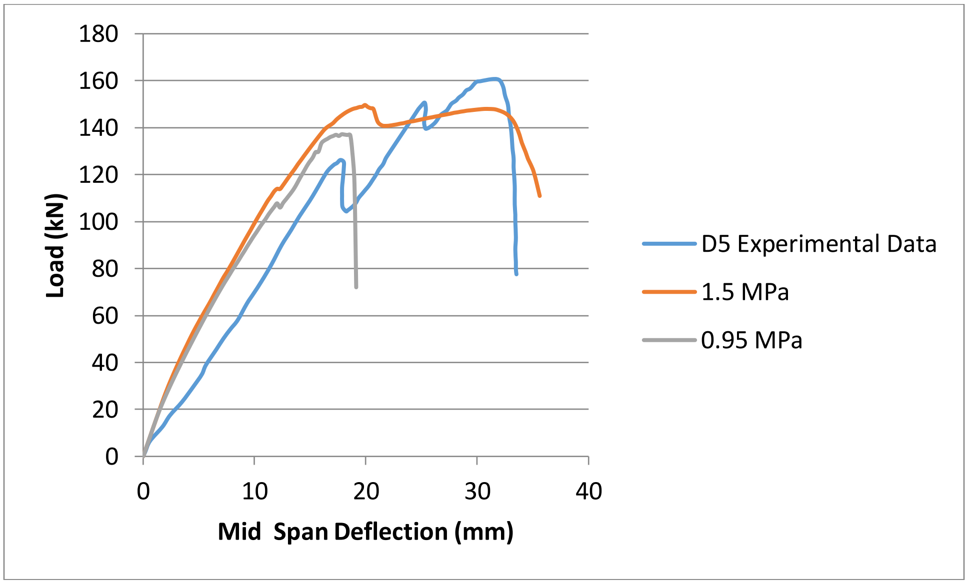

Figure 3.20. Effects of tensile strength on the load-deformation response of beam D5 using Hognestad model

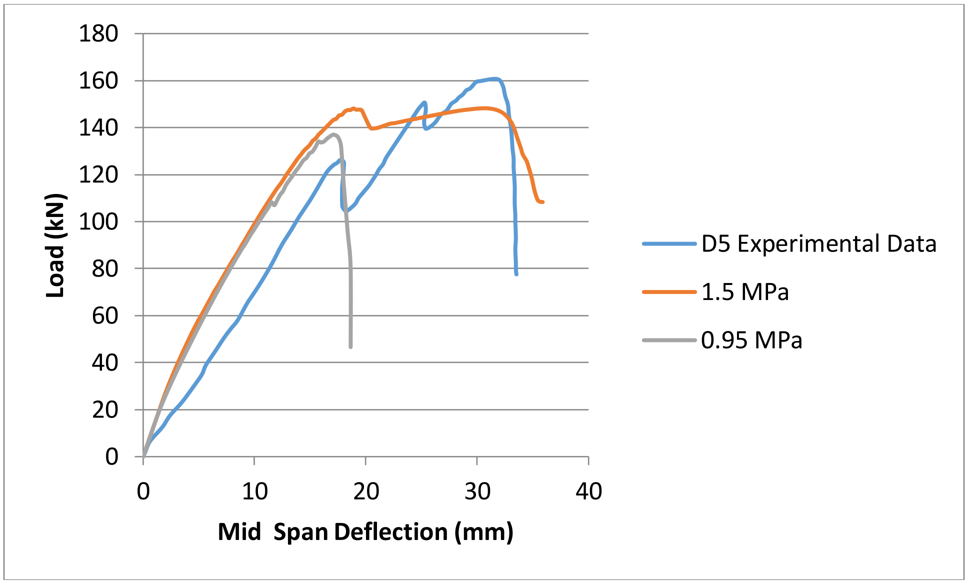

Figure 3.21. Effects of tensile strength on the load-deformation response of beam D5 using Popovic model

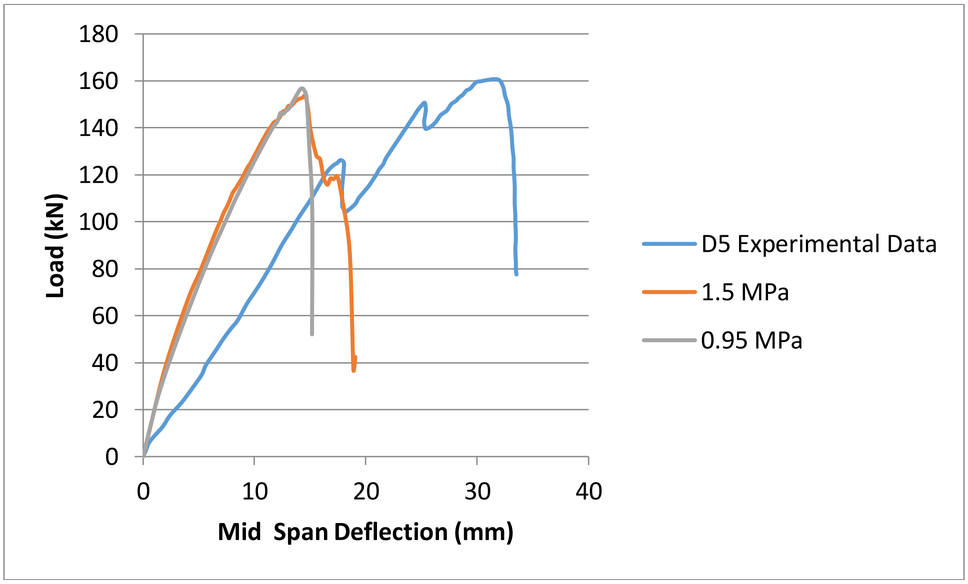

Figure 3.22. Effects of tensile strength on the load-deformation response of beam D5 using Smith-Young model

3.5.2. Compression Softening

The reduction of compressive strength and stiffness resulting from simultaneous transverse cracking and tensile straining, known as compression softening, can have a significant impact on the load-deformation response of reinforced concrete structures. In VecTor2, compression softening models calculate the softening parameter, β_d, which has a value between zero and one. A value of one indicates that the compression response is independent of the coexisting tensile strains.

The impact of Vecchio-Collins (1982) and Vecchio (1992-A) models on the load-deformation response of frost-damaged beams is explored in this section. Both are strength-and-strained softened models, which means that they use β_d to reduce both the compressive strength, f_c, and corresponding strain, ε_0, to determine the peak compressive strength, f_p, and corresponding strain, ε_p, used in the compression response model.

The compression softening model proposed by Vecchio and Collins (1982), which was originally developed for the Hognestad compression stress-strain curve, does not take into account the softening effects of shear slip if included in the analysis. On the other hand, the model by Vecchio (1992-A), which was originally developed for the Popovics compression response, includes a factor that takes into consideration shear slip deformations, if included in the analysis.

The Vecchio-Collins (1982) compression softening model computes the softening parameter, β_d, the peak compressive strength, f_p, and corresponding strain, ε_p as follows:

$$\beta_d = \frac{1}{0.85 - 0.27\left(\frac{-\varepsilon_{c1}}{\varepsilon_{c2}}\right)} \leq 1 \tag{3.30}$$

$$f_p = \beta_d \, f'_c \tag{3.31}$$

$$\varepsilon_p = \beta_d \, \varepsilon_o \tag{3.32}$$

where ε_{c1} and ε_{c2} are the principal tensile and compressive strains in the concrete, respectively. The Vecchio (1992-A) compression softening model computes the softening parameter, β_d, the peak compressive strength, f_p, and corresponding strain, ε_p as follows:

$$\beta_d = \frac{1}{1 + C_s \, C_d} \leq 1 \tag{3.33}$$

$$C_d = \begin{cases} 0 & if\ r < 0.28 \\ 0.35\ (r - 0.28)^{0.80} & if\ r > 0.28 \end{cases} \tag{3.34}$$

$$r = \frac{-\varepsilon_{c1}}{\varepsilon_{c2}} \leq 400 \tag{3.35}$$

$$C_s = \begin{cases} 0 & if\ shear\ slip\ not\ considered \\ 0.55 & if\ shear\ slip\ considered \end{cases} \tag{3.36}$$

$$f_p = \beta_d\ f'_c \tag{3.37}$$

$$\varepsilon_p = \beta_d\ \varepsilon_o \tag{3.38}$$

As shown in Figure 3.23, using either compression softening model produces a similar load-deflection response for the flexure-governed beam. However, the Vecchio-Collins (1982) model provides a better approximation of the deflection at failure for the shear-governed beam, D5; see Table 3.5 and Figure 3.24. Hence, the Vecchio-Collins (1982) model was used in the analysis of both the flexure-governed and shear-governed beams.

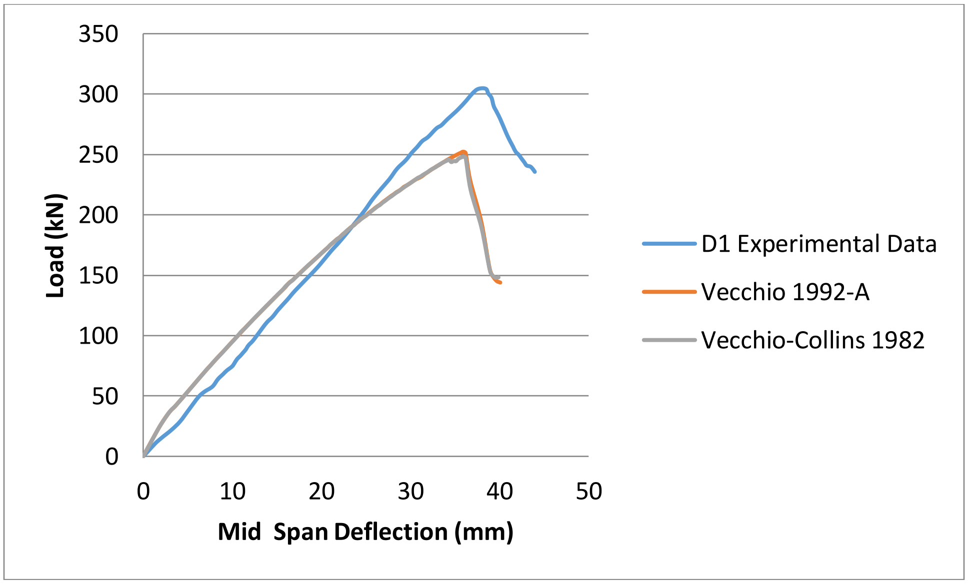

Figure 3.23. Effects of compression softening models on the load-deformation response of beam D1

Table 3.4. Comparison of beam D1 peak load and deflection at peak load predicted by FE analysis using various compression softening models

Compression Softening Model	P_{max} (kN)	P_{max} FE/Exp.	Δ_{max} (mm)	Δ_{max}FE/Exp.
Vecchio (1992-A)	252.26	0.83	35.92	0.94
Vecchio-Collins (1982)	248.03	0.81	35.93	0.94

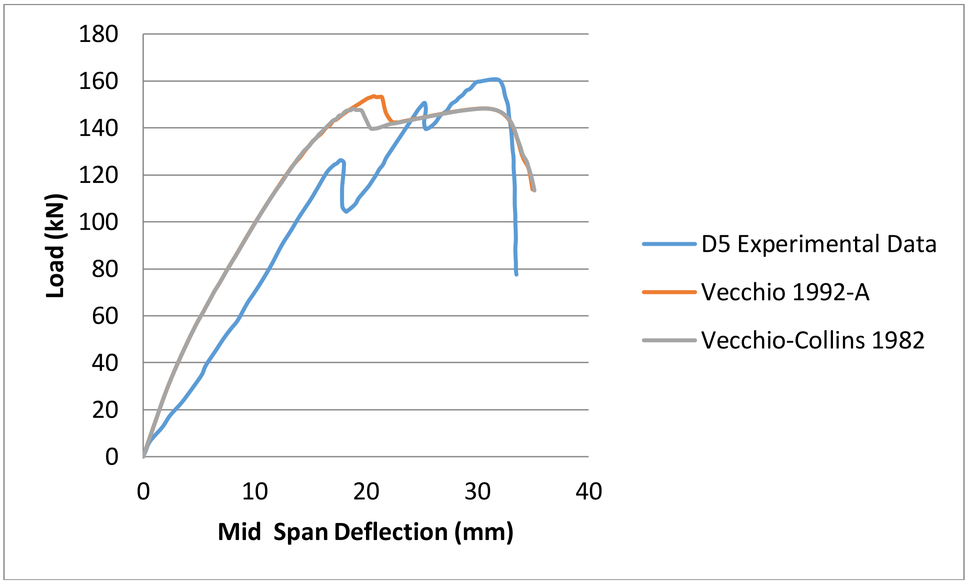

Figure 3.24. Effects of compression softening models on the load-deformation response of beam D5

Table 3.5. Comparison of beam D5 peak load and deflection at peak load predicted by FE analysis using various compression softening models

Compression Softening Model	P_{max} (kN)	P_{max} FE/Exp.	Δ_{max} (mm)	Δ_{max}FE/Exp.
Vecchio (1992-A)	153.52	0.96	20.71	0.66
Vecchio-Collins (1982)	148.23	0.92	30.59	0.98

3.5.3 Tension Response

Concrete behaves in a brittle manner when it is in tension. The response of concrete prior to cracking is assumed to be linear elastic as defined by the following relationship:

$$f_{c1} = E_c \varepsilon_{c1} \text{ for } 0 < \varepsilon_{c1} < \varepsilon_{cr} \tag{3.39}$$

$$\varepsilon_{cr} = \frac{f_t}{E_c} \tag{3.40}$$

where f_{c1} is the principal tensile stress in concrete, ε_{c1} is the principal tensile strain , f_t is the cracking stress of the concrete determined by the cracking criterion model, and ε_{cr} is the cracking strain. When reinforced concrete experiences cracking, there are no tensile stresses at the surface of the cracks. Concrete which remains uncracked in the tributary area of the reinforcement, however, continues to be subjected to average tensile stresses due to bond action. As tensile straining continues, the crack widths increase and the bond between steel and concrete weakens. The average concrete tensile stresses slowly diminish. These average tensile stresses ($<f_t$) exist in relatively large regions surrounding the tensile reinforcement and thus, the reinforcement is not alone in contributing to the stiffness of the reinforced concrete in tension. This is referred to as tension stiffening. Failing to account for tension stiffening reduces the concrete tensile stresses to zero at the instance cracking occurs and assumes that the reinforcement alone is resisting the tensile stress.

VecTor2 includes tension stiffening effects in the analysis through a gradual decrease of average stress-strain response of concrete in tension. The average concrete tensile stress determined is denoted by f_{c1}^{a}, to distinguish it from the average concrete tensile stress due to tension softening effects, denoted by f_{c1}^{b}. The magnitude, f_{c1}^{a} is always limited by the yielding of the reinforcement of the crack, and additionally by the maximum shear stress at the crack when slip deformations are not included. The larger of the two tensile stresses is assumed to be the average post cracking concrete tensile stress:

$$f_{c1} = \max\left(f_{c1}^{a}, f_{c1}^{b}\right) \tag{3.41}$$

The effects of no tension stiffening as well as the effects of the Vecchio (1982) and the Modified Bentz (2003) models on the load-deformation response of frost-damaged beams are explored in this section. The model proposed by Vecchio (1982) was developed based on results of tests conducted on thirty panel elements with welded wire mesh reinforcement at the University of Toronto and was originally used in the Modified Compression Field Theory. According to this model, the average concrete tensile stress-strain curve is determined as follows:

$$f_{c1}^{a} = \frac{f_t}{1 + \sqrt{200\varepsilon_{c1}}} \; for \; 0 < \varepsilon_{cr} < \varepsilon_{c1} \tag{3.42}$$

The Bentz (2003) formulation takes into account the percentage of reinforcement and bond characteristics. It is as follows:

$$f_{c1}^{a} = \frac{f_t}{1 + \sqrt{c_t \varepsilon_{c1}}} \; for \; \varepsilon_{c1} > \; \varepsilon_{cr} \tag{3.43}$$

where

$$c_t = 3.6 \; t_d \cdot m \tag{3.44}$$

$$t_d = 0.6 \tag{3.45}$$

$$\frac{1}{m} = \sum_{i=1}^{n} \frac{4\rho_i}{d_{bi}} \cdot |\cos{(\theta - \alpha_i)}| \tag{3.46}$$

where $\rho_i$is the reinforcement ratio, d_{bi} is the rebar diameter, θ is the inclination of the principal direction, and $\alpha_i$is the inclination of reinforcement.

Figure 3.25 shows the effects of tension stiffening models on the load-deformation response of beam D1. The load deflection curves generated with no tension stiffening as well as with the tension stiffening models are noticeably similar and do not deviate significantly from one another. Similarly, for beam D5, Figure 3.26 shows the effects of tension stiffening models on the load-deflection curves. It is observed that the load capacity is more accurately estimated with the

Vecchio (1982) model; see Table 3.7. Hence, the Vecchio (1982) tension stiffening model was considered in the analysis of frost-damaged beams.

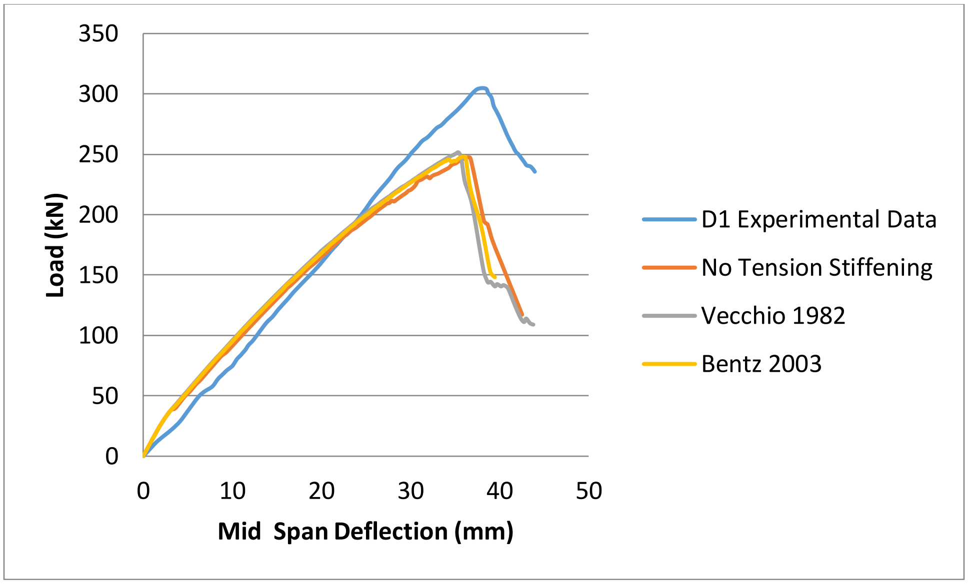

Figure 3.25. Effects of tension stiffening models on the load-deformation response of beam D1

Table 3.6. Comparison of beam D1 peak load and deflection at peak load predicted by FE analysis using various tension stiffening models

Tension Stiffening Model	P_{max} (kN)	P_{max} FE/Exp.	Δ_{max} (mm)	Δ_{max} FE/Exp.
No tension stiffening	247.51	0.81	36.46	0.96
Vecchio (1982)	251.52	0.83	35.41	0.93
Modified Bentz (2003)	248.03	0.81	35.93	0.94

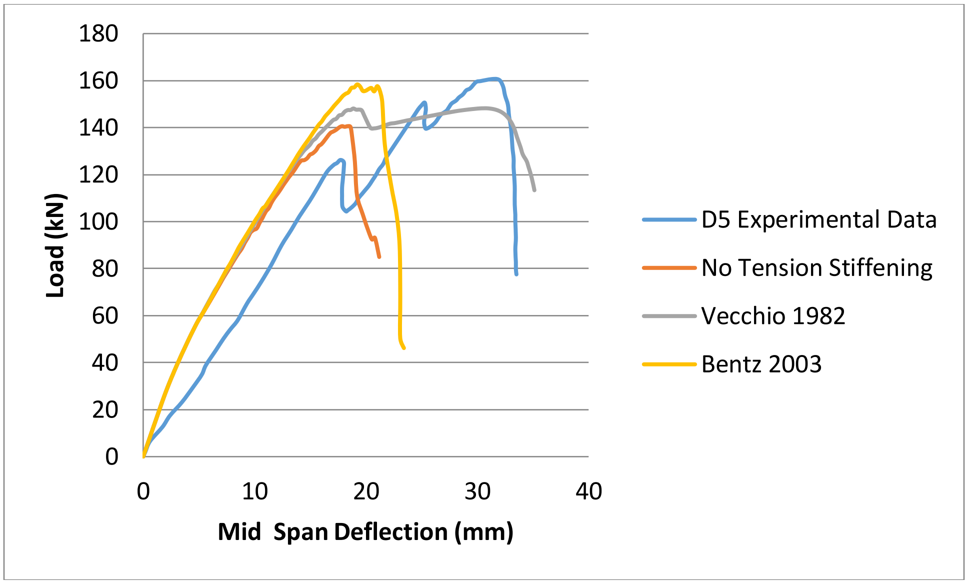

Figure 3.26. Effects of tension stiffening models on the load-deformation response of beam D5

Table 3.7. Comparison of beam D5 peak load and deflection at peak load predicted by FE analysis using various tension stiffening models

Tension Stiffening Model	P_{max} (kN)	P_{max} FE/Exp.	Δ_{max} (mm)	Δ_{max} FE/Exp.
No tension stiffening	140.62	0.88	17.87	0.57
Vecchio (1982)	148.23	0.92	30.59	0.98
Modified Bentz (2003)	158.38	0.99	19.22	0.61

3.5.4 Tension Softening

After cracking, tensile stresses are present in plain concrete. These tensile stresses diminish from increased tensile straining. This phenomenon is known as tension softening and occurs because concrete is not a perfectly brittle material. In terms of fracture mechanics, energy is required for a localized crack to form. As the crack grows, it dissipates energy which propagates to the crack tip.

Including tension softening in the analysis of reinforced concrete structures can have significant implications. The inclusion of post cracking stress-strain curve for plain concrete allows for a more accurate load-deformation response as well as ductility of the structure.

In VecTor2, the post cracking average tensile stress-strain curve constitutes the tension softening effects. As mentioned previously, the average concrete tensile stress due to tension softening is denoted by f_{c1}^{b} , to distinguish it from the average concrete tensile stress due to tension stiffening effects, denoted by a f_{c1}^{a}. As per Eq. 3.41, the larger of the two tensile stresses is assumed to be the average post-cracking concrete tensile stress.

The nonlinear Hordijk model and the nonlinear Yamamoto (1999) models were both used in the analysis in order to investigate the effects of tension softening on the load-deflection response of frost-damaged beams. The nonlinear Hordijk model, appropriate for both normal-weight and light-weight concrete, is implemented in VecTor2 with the following formulation:

$$f_{c1} = f_t\left[\left(1+\left(C_1\frac{w_{crx}}{w_{ult}}\right)^3\right)exp\left(-C_2\frac{w_{crx}}{w_{ult}}\right)-\frac{w_{crx}}{w_{ult}}(1+C_1^3)\exp\left(-C_2\right)\right] \tag{3.47}$$

$$C_1 = 3 \tag{3.48}$$

$$C_2 = 6.93 \tag{3.49}$$

$$w_{ult} = \frac{5.136\,G_f}{f_t} \tag{3.50}$$

where G_f is concrete’s fracture energy, w_{crx} is the average crack width, and w_{ult} is the ultimate crack width.

The tension softening base curve as proposed by Yamamoto (1999) is formulated as follows:

$$f_{ts,base} = \begin{cases} \dfrac{f_t}{1+\sqrt{c(\varepsilon_{c1}-\varepsilon_{cr})}} & for\ \varepsilon_{cr} < \varepsilon_{c1} < \varepsilon_{ch} \\ f_{ch}\dfrac{(\varepsilon_{te}-\varepsilon_{c1})}{(\varepsilon_{te}-\varepsilon_{ch})} \geq 0 & for\ \varepsilon_{ch} < \varepsilon_{c1} \end{cases} \tag{3.51}$$

where the characteristic strain, ε_{ch}, of the tension softening curve is determined as follows:

$$\varepsilon_{ch} = \frac{2\,G_f}{L_r \cdot f_t}.\,1.1 \qquad \varepsilon_{cr} < \varepsilon_{ch} < 10\varepsilon_{cr} \tag{3.52}$$

The terminal strain, ε_{te}, is the strain at which the tension softening stress diminishes to zero, determined as:

$$\varepsilon_{te} = 5\varepsilon_{ch} \tag{3.53}$$

and c is the tension softening coefficient determined based on the following:

$$\frac{G_f}{L_r} = \int_0^{\infty} f_{ts,base}\, d\varepsilon_{c1} \tag{3.54}$$

where L_r is the representative length which is the distance over which the crack is assumed to be uniformly distributed and is assigned a value of half the crack spacing.

As can be observed from Figures 3.27 and 3.28, tension softening has a considerable impact on the load-deformation response of frost-damage concrete beams. For flexural-governed and shear-governed beams, when tension softening is not considered, the load and deflection capacity are grossly underestimated. For the flexural-governed beam, the nonlinear Hordijk model provides the best approximation of load and deflection at failure; see Tables 3.8. Therefore, in the analysis of flexural-governed frost-damaged beams, the nonlinear Hordijk tension softening model is used. The nonlinear Hordijk model was able to most accurately predict the failure load and the deflection of the shear-governed beam as well; see Tables 3.9. Therefore, it was also chosen to be used in the analysis of shear-governed frost-damaged beams.

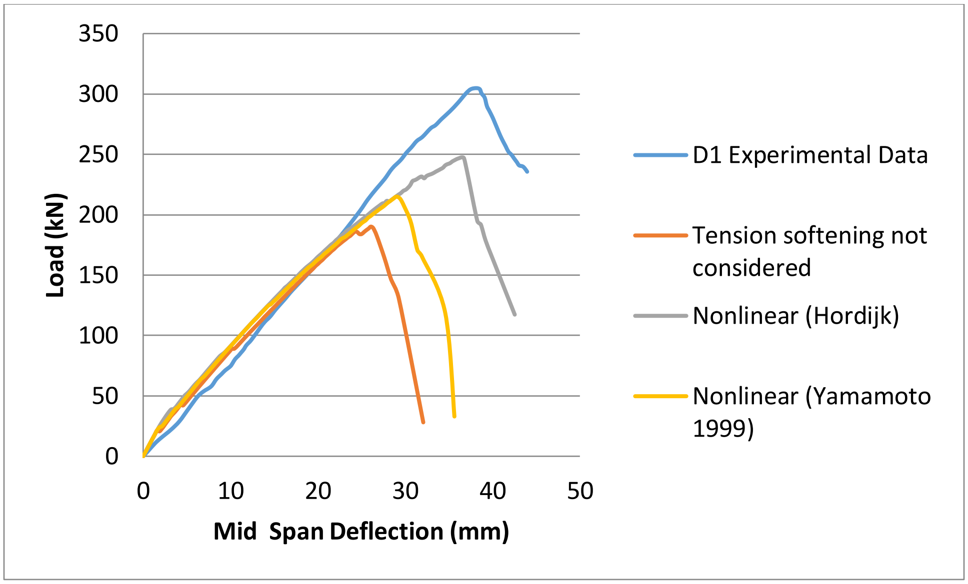

Figure 3.27. Effects of tension softening models on the load-deformation response of beam D1

Table 3.8. Comparison of beam D1 peak load and deflection at peak load predicted by FE analysis using various tension softening models

Tension Softening Model	P_{max} (kN)	P_{max} FE/Exp.	Δ_{max} (mm)	Δ_{max}FE/Exp.
No tension softening	190.15	0.62	26.07	0.68
Nonlinear Hordijk	247.51	0.81	36.46	0.96
Nonlinear Yamamoto (1999)	214.86	0.70	28.93	0.76

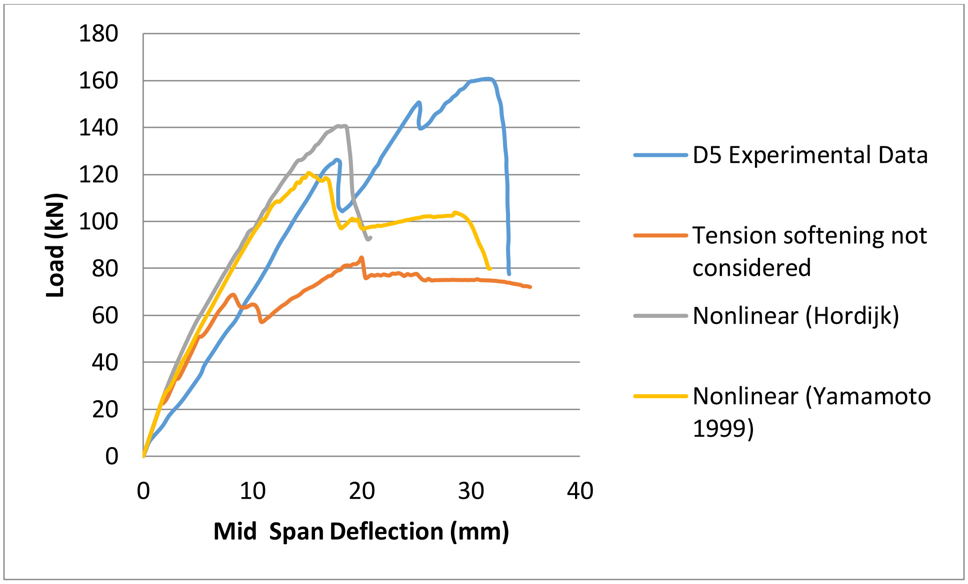

Figure 3.28. Effects of tension softening models on the load-deformation response of beam D5

Table 3.9. Comparison of beam D5 peak load and deflection at peak load predicted by FE analysis using various tension softening models

Tension Softening Model	P_{max} (kN)	P_{max} FE/Exp.	Δ_{max} (mm)	Δ_{max}FE/Exp.
No tension softening	84.46	0.53	20.04	0.64
Nonlinear Hordijk	140.62	0.88	17.87	0.57
Nonlinear Yamamoto (1999)	120.57	0.75	15.11	0.48

3.5.5 Cracking Criterion

The cracking strength of concrete is related to parameters such as the specimen size and compressive strength as well as the stress state; an increase in transversely acting compressive stresses results in the decrease of cracking strength. To account for this effect in the analysis, the cracking criterion computes f_t by considering the coexisting compressive stresses or strains. The cracking strain,ε_{cr}, is then computed through the linear-elastic relationship presented in Eq. 3.40 before cracking. The computed values of f_t and ε_{cr} are then used for the tension stress-strain response and the tension stiffening models.

The effects of the Mohr-Coulomb (Stress) and the CEB-FIP cracking model on the load-deflection response of frost-damaged concrete are explored in this section. For the Mohr-Coulomb (Stress) model, the combination of shear stress, τ, and normal stresses, f_{c1} and f_{c3} that result in shear failure is defined by the failure envelope, which is tangent to Mohr's circle. For a set of principal concrete strains, $\varepsilon_{c3} < \varepsilon_{c2} < \varepsilon_{c1}$, the principal compressive stress is determined as follows:

$$f_{c3} = \begin{cases} -f_c\left(2\left(\frac{\varepsilon_{c3}}{\varepsilon_o}\right) - \left(\frac{\varepsilon_{c3}}{\varepsilon_o}\right)^2\right) & for \varepsilon_{c3} < \varepsilon_o < 0 \\ -f_c & for\ \varepsilon_o < \varepsilon_{c3} < 0 \\ 0 & for\ 0 > \varepsilon_{c3} \end{cases} \tag{3.55}$$

The cracking strength is then the principal tensile stress, f_{c1} of the Mohr's circle tangent to the failure envelope, i.e.,

$$f_{cr} = f_{cru}\left(1 + \left(\frac{f_{c3}}{f_c}\right)\right), \qquad 0.20 f_t \leq f_{cr} \leq f_t \tag{3.56}$$

where f_{cru} is the unconfined cracking strength.

With the CEB-FIP model, the cracking strength for increasing biaxial compression is reduced based on the following linear relationship:

$$f_{cr} = f_{cru}\left(1 + 0.8\left(\frac{f_{c3}}{f_c}\right)\right), \qquad 0.20 f_t \leq f_{cr} \leq f_t \tag{3.57}$$

The principal compressive stress, f_{c3}, is computed from Eq. 3.55 and the unconfined cracking strength, f_{cru}, is computed from the compressive strength, f_c, as follows:

$$f_{cru} = 0.6\sqrt{f_c} \tag{3.58}$$

Figures 3.29 and 3.30 illustrate the effects of the Mohr-Coulomb (Stress) and the CEB-FIP cracking models on the load-deflection response of frost-damaged beams. For both beams, using either of the two models generates a similar load-deflection response. However, deflection at failure of beam D1 is predicted slightly more accurately with the CEB-FIP model; see Table 3.10.

Therefore, this model was chosen to be used in the analysis of both flexural and shear governed frost-damaged beams.

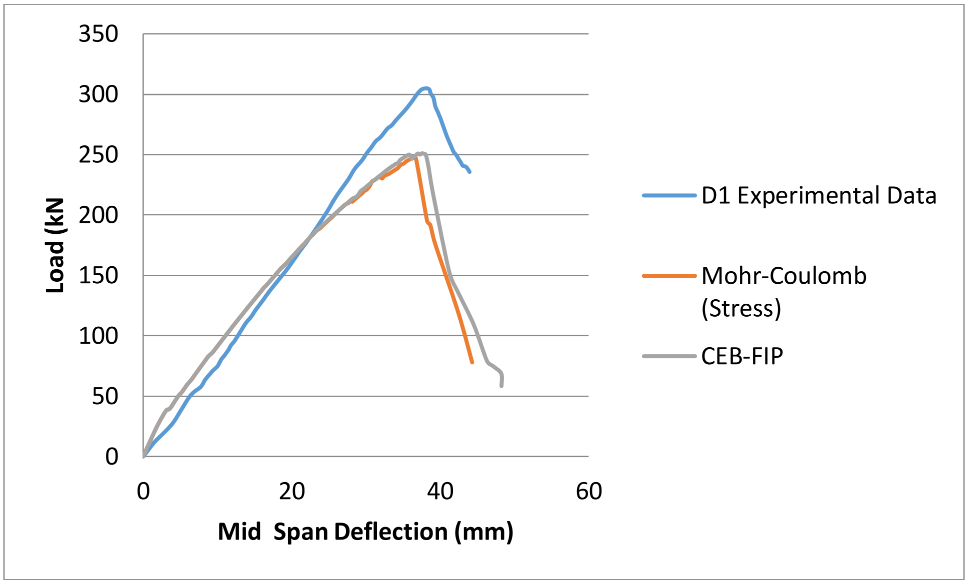

Figure 3.29. Effects of cracking criterion models on the load-deformation response of beam D1

Table 3.10. Comparison of beam D1 peak load and deflection at peak load predicted by FE analysis using various cracking criterion models

Cracking Criterion Model	P_{max} (kN)	P_{max} FE/Exp.	Δ_{max} (mm)	Δ_{max} FE/Exp.
Mohr-Coulomb (Stress)	247.51	0.81	36.46	0.96
CEB-FIP	250.98	0.82	37.53	0.98

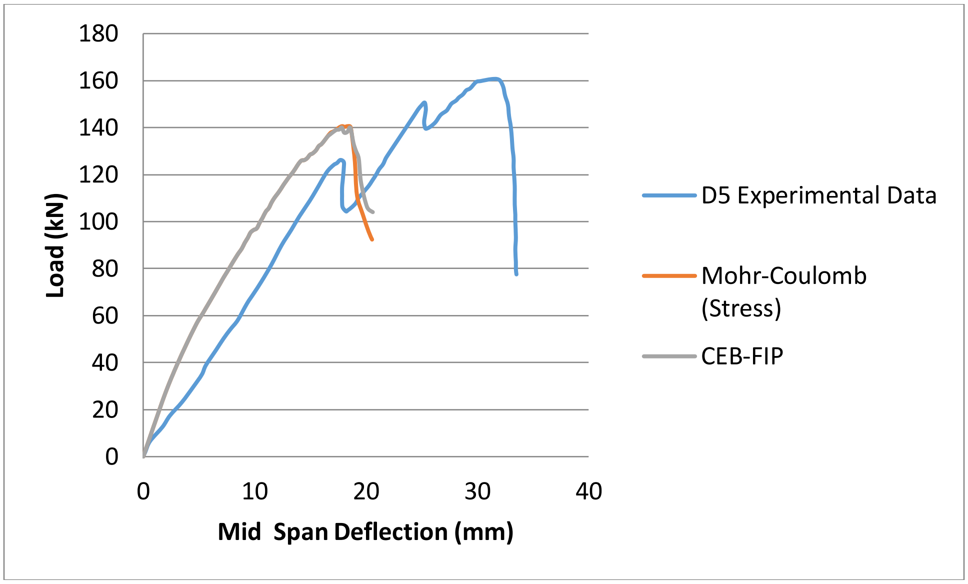

Figure 3.30. Effects of cracking criterion models on the load-deformation response of beam D5

Table 3.11. Comparison of beam D5 peak load and deflection at peak load predicted by FE analysis using various cracking criterion models

Cracking Criterion Model	P_{max} (kN)	P_{max} FE/Exp.	Δ_{max} (mm)	Δ_{max}FE/Exp.
Mohr-Coulomb (Stress)	140.62	0.88	17.87	0.57
CEB-FIP	140.06	0.87	17.84	0.57

3.5.6 Crack Width Check

VecTor2 implements crack width check so that the average compressive stresses may be reduced if the crack width exceeds a specified limit. Limiting compressive stresses in elements with cracks of considerable width is necessary. One reason for this is because the reorientation of the principal stresses is overestimated in the absence of shear-slip distortion considerations. Transmission of local compressive stress across the crack takes place; however, when the crack exceeds the specified width, this transmission is not likely to take place. The load-deformation response is more accurately predicated when the average compressive stress is reduced upon the crack exceeding a limit.

The average compressive stress computed from the stress-strain response, f_{c2}, is reduced by a crack coefficient β_{cr}.

$$f_{c2} = \beta_{cr} f_{c2}^{*} \tag{3.59}$$

$$\beta_{cr} = \begin{cases} 1 & for\ w < w_l \\ 1 - \dfrac{w - w_l}{3} \geq 0 & for\ w_l < w \end{cases} \tag{3.60}$$

where w is the crack width in the element, and w_l is the limiting crack width, which is selected to be one quarter of the aggregate size.

The crack width was limited to 5 mm and 10 mm. The effects of specifying these limits in VecTor2 are shown in Figures 3.31 and 3.32 for beams D1 and D5, respectively. For both beams, the change in the response curve is insignificant when the limit of the crack width is increased, see Tables 3.12 and 3.13.

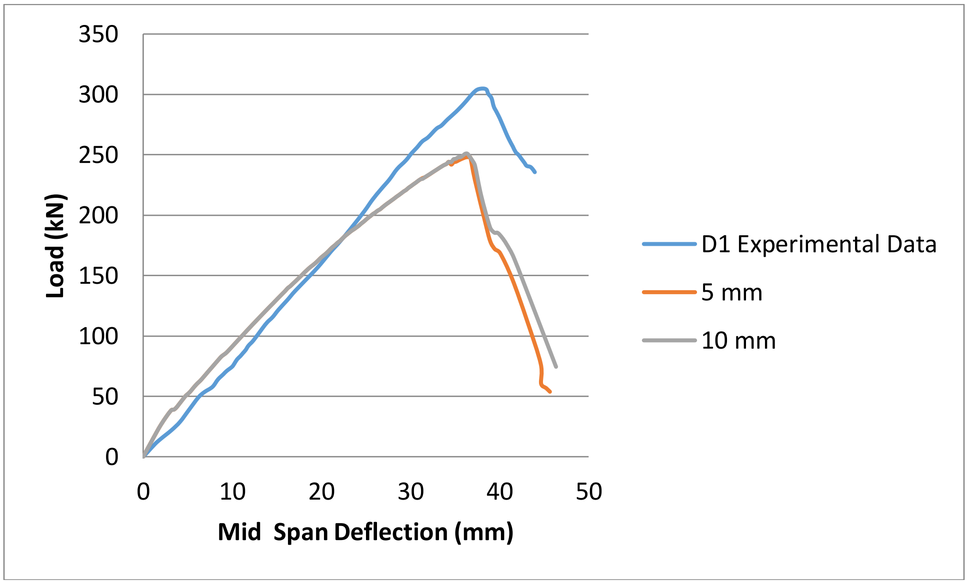

Figure 3.31. Effects of crack width limit on the load-deformation response of beam D1

Table 3.12. Comparison of beam D1 peak load and deflection at peak load predicted by FE analysis using various crack width limits

Crack Width Limit	P_{max} (kN)	P_{max} FE/Exp.	Δ_{max} (mm)	Δ_{max}FE/Exp.
5 mm	248.06	0.81	36.46	0.96
10 mm	250.84	0.82	36.15	0.95

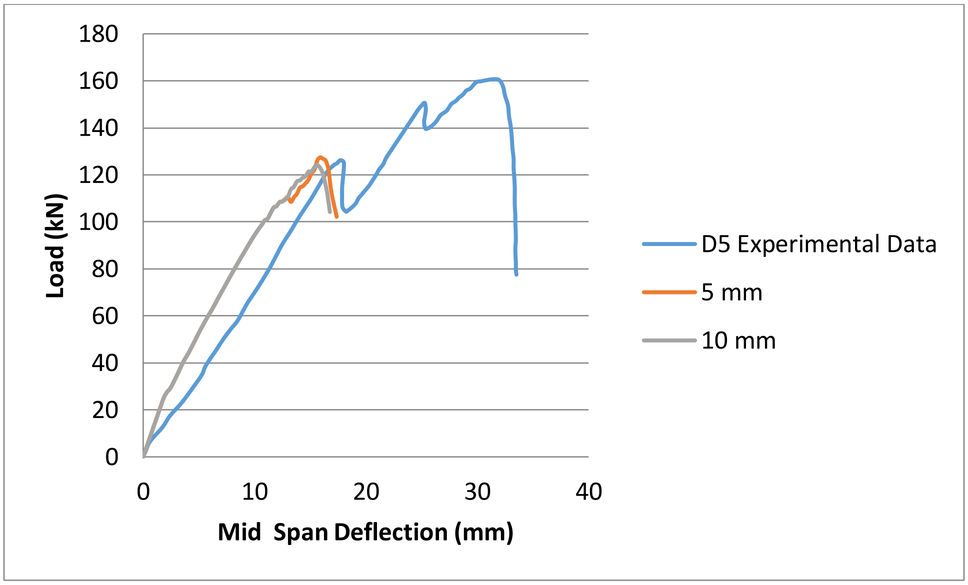

Figure 3.32. Effects of crack width limit on the load-deformation response of beam D5

Table 3.13. Comparison of beam D5 peak load and deflection at peak load predicted by FE analysis using various crack width limits

Crack Width Limit	P_{max} (kN)	P_{max} FE/Exp.	Δ_{max} (mm)	Δ_{max}FE/Exp.
5 mm	127.44	0.79	15.90	0.51
10 mm	124.18	0.77	15.64	0.50

3.5.7 Bond-Slip Response

Beam D1 tested by Hassanzadeh and Fagerlund (2006) was analysed to show the effects of modelling bond-slip on the load-deformation response of frost-damaged reinforced concrete beams. The experimental and analytical response of the beam is shown in Figure 3.33. From the load-deflection response curves, assuming perfect bond and not considering the effect of frost damage on the bond between the reinforcement and concrete provides a slightly stiffer response.

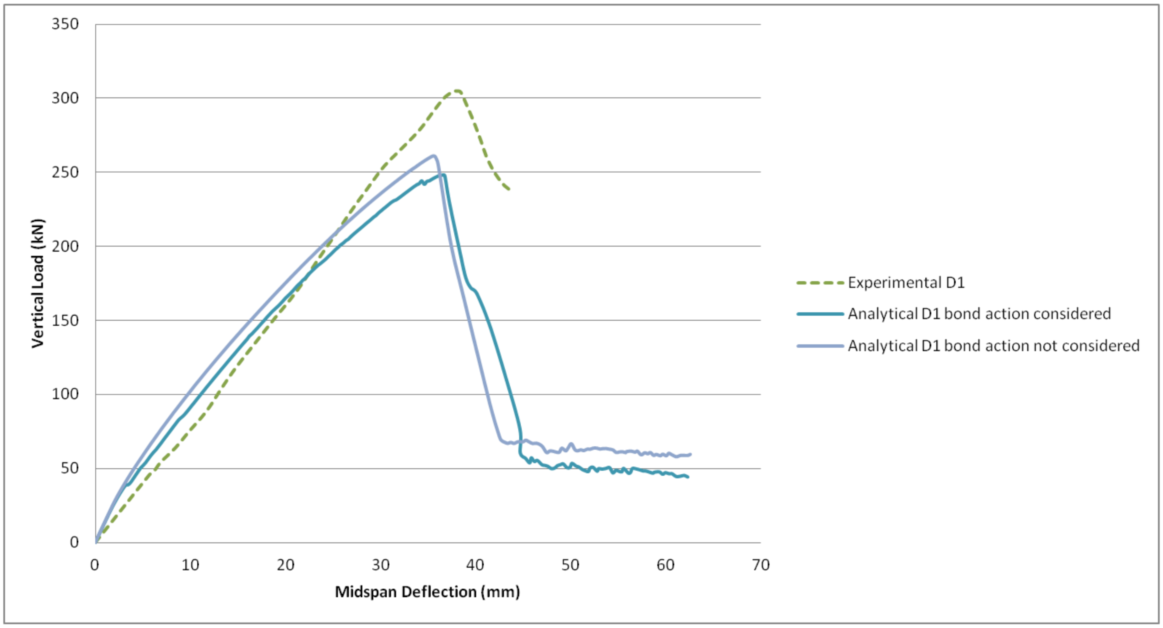

Figure 3.33. The response of a frost-damaged beam with and without the consideration of bond action

3.6 Summary of Modelling Methodology

Frost damage changes the internal structure of concrete by introducing micro and macro cracks. This change in the internal structure was modeled as a change in the mechanical behaviour, which relates to the material properties and bond behaviour of frost-damaged concrete. The damage caused by freezing of concrete in the presence of a chloride solution causes surface scaling, which was modeled as a reduction of the concrete cover.

To accurately predict the structural response of frost-damaged concrete elements, the use of appropriate constitutive models in the numerical analysis is critical. The following table shows the behavioural models that were selected based on the analyses of available material models discussed in this chapter.

Table 3.14 Models for concrete material used in the numerical analysis of frost-damaged beams

	Models for Concrete Materials	
	Flexure-governed beam	Shear-governed beam
Compression Response	Hognestad	Popovics
Compression Softening	Vecchio-Collins (1982)	Vecchio-Collins (1982)
Tension Stiffening	Vecchio (1982)	Vecchio (1982)
Tension Softening	Nonlinear Hordijk	Nonlinear Hordijk
Cracking Criterion	CEB-FIP	CEB-FIP

Chapter 4. Finite Element Model Validation

4.1 Introduction

In this chapter, the methodology presented in the previous chapter to model frost-damaged beams is validated. The proposed methodology is used in the nonlinear finite element analysis of frost-damaged beams that were tested by Hassanzadeh and Fagerlund (2006) as part of a research study to investigate the behaviour of frost-damaged reinforced concrete beams. The load-carrying capacity and failure mode of the beams predicted by the numerical analysis are compared with the available experimental data in order to validate the proposed methodology.

4.2 Modeling Frost Damage in Reinforced Concrete Beams

Frost damage reduces the stiffness and load-carrying capacity of reinforced concrete structures. To assess the damage in a structure subjected to successive freeze-thaw cycles, the damage needs to first be quantified. The degree of internal frost damage is related to the internal microstructure of the concrete. Successive freeze-thaw cycles introduce micro and macro cracks; this change in the internal structure affects the material properties, thereby reducing the shear, moment and bond capacity. In this work, change in the material properties of concrete is, therefore, used to quantify internal frost damage. It is further assumed that damage is uniform throughout the cross section, as opposed to a non-uniform distribution as illustrated in Figure 2.6. Surface scaling, on the other hand, only affects the concrete cover and causes loss of concrete area. This reduction in cross-section results in a reduction in moment, shear and anchorage capacities.

In the previous chapter, methods to account for the changes in material and bond properties of frost-damaged concrete were introduced; these methods modify the mechanical behaviour of concrete in accordance with a measured amount of frost damage, allowing for prediction of the load-carrying capacity of the damaged structures. The behaviour of frost-damaged concrete beams tested by Hassanzadeh and Fagerlund (2006) was modeled using the proposed methodology. VecTor2 is the non-linear finite element analysis program that was used. In the subsequent sections, validation of the proposed methodology is discussed.

4.3 Experimental Beam Tests for Comparison with FE Analysis

Hassanzadeh and Fagerlund (2006) carried out an experimental study to investigate the behaviour of frost-damaged reinforced concrete beams. In the experimental program, tests were carried out on six types of beams. There were two of each beam type; one was the reference beam exposed to laboratory climate and the other was the frost-damaged beam. The types of beams, their varying geometries and reinforcement contents are presented in Table 4.1, where l is the span between supports. The length of the beam is $l + 0.2\ (m)$. Variables h, b and d are the beam depth, width of the cross-section and effective beam depth, respectively. The reinforcement ratio ρ is calculated as A_s/bd, where A_s is the longitudinal reinforcing steel cross-sectional area, and ρ_{bal} is the balanced reinforcement ratio. As it is presented in Table 4.1, the diameter of all longitudinal bars was 20 mm, and the diameter of all stirrups was 8 mm. Four stirrups were placed at each support in beam types 5 and 6 to prevent cracking of the beams due to the concentrated load at the supports.

Table 4.1. Type of beams (Hassanzadeh and Fagerlund, 2006)

Type	$l\ (m)$	h x b $(mm$	$d\ (m)$	Tensile reinforcement	Stirrup	Beam		ρ (%)	ρ/ρ_{bal}	
						Reference	Damaged		Reference	Damaged
1	4.4	500 x 200	430	4Ø20	28Ø8	R1	D1	1.46	0.84	1.72
2	3.0	300 x 200	260	3Ø20	18Ø8	R2	D2	1.81	1.05	2.13
3	4.4	500 x 200	430	6Ø20	32Ø8	R3	D3	2.19	1.27	2.58
4	3.0	300 x 200	260	5Ø20	22Ø8	R4	D4	3.41	1.97	4.02
5	4.4	500 x 200	430	4Ø20	8Ø8	R5	D5	1.46	0.84	1.72
6	3.0	300 x 200	260	3Ø20	8Ø8	R6	D6	1.81	1.05	2.13

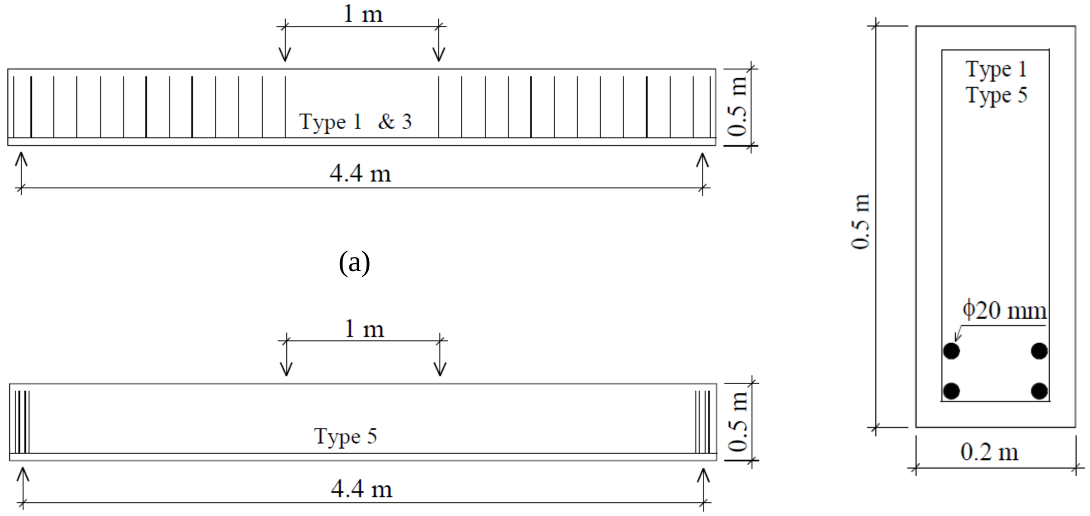

(a)

(b)

(c)

Figure 4.1. Example of beam types and reinforcement arrangement (reproduced from Hassanzadeh and Fagerlund, 2006)

Beam types 1, 3 and 5 are shown in Figure 4.1 (a) and (b). As can be seen from the figure, the beams were subjected to a four-point-bending test. The distance between the supports and the distance between the loads was 4.4 m and 1 m, respectively. The stirrups in beam types 1 and 3 were distributed evenly within the shear span, while in type 5 beam the stirrups were concentrated at the supports. Figure 4.1 (c) shows the cross section of beam types 1 and 5. The dimensions of the cross section are the same for beam type 3; the reinforcement content, however, differs. Beam types 2, 4 and 6 differ from beam types 1, 3 and 5 in their size and amount of reinforcement, as shown in Table 4.1.

To induce frost damage in the beams, conditions where the degree of water saturation, S, exceeded the critical value, S_{cr} had to be achieved. The critical water saturation S_{cr} is a material property and does not depend on the number of frost cycles or freezing rate. In order to reach S_{cr} within a reasonable amount of time, the entrapped air in the pore system was replaced with water by applying vacuum treatment with a residual pressure of 2-mm Hg, and subsequently the beams were submerged in water. The beams then experienced two complete freeze-thaw cycles. Freezing took place in the freeze room and thawing took place in water. They were once again placed in the freeze room and were taken out a day before the bending test in order to reach the laboratory temperature. The temperature inside the climate chamber was between -20° C and -22° C. The beams were kept in the freeze room for at least three days and were kept at least two days in water.

The four-point-bending test was performed on the beams to determine the failure behaviour. The load-deflection curves were captured, where the load was the total load applied on the beam and the deflection is the difference between the displacement at the midspan of the beam and at the supports. The measured compressive strength was 37.6 MPa and 17.5 MPa for undamaged concrete and frost damaged concrete, respectively.

As mentioned in Chapter 3, the numerical analysis was performed using the non-linear finite element analysis program, VecTor2. Concrete was modeled with the four-noded plane stress rectangle element. The truss element was used to model both the longitudinal and transverse steel reinforcement. The link element was used across the concrete and reinforcement interface to model the influence of localized bond-slip on the load-deformation response of frost-damaged reinforced concrete. Half of the beams were modeled due to symmetry of geometry, boundary conditions and loading. The automatic mesh generation function with the hybrid discretization type was used to create the mesh of the beams. For optimal mesh, the coarse mesh that was initially generated for each beam was refined by decreasing the element size. A change in the results was noticed and so the element size was further reduced. The mesh were refined until there was no change in the results from further refining the mesh. Through this process, the optimal mesh of the beams was produced. The finite element mesh of the beams is shown in Figure 4.2.

The input parameters used in the FE analysis of the frost damaged beams were determined using the relationships presented in Chapter 3 and are shown in Table 4.2. Reference bond stresses, τ_i, and corresponding slips, Δ_i, were used as input in VecTor2 to define the multilinear bond stress-slip relationships for frost-damaged concrete. These relationships are shown in Figure 4.3.

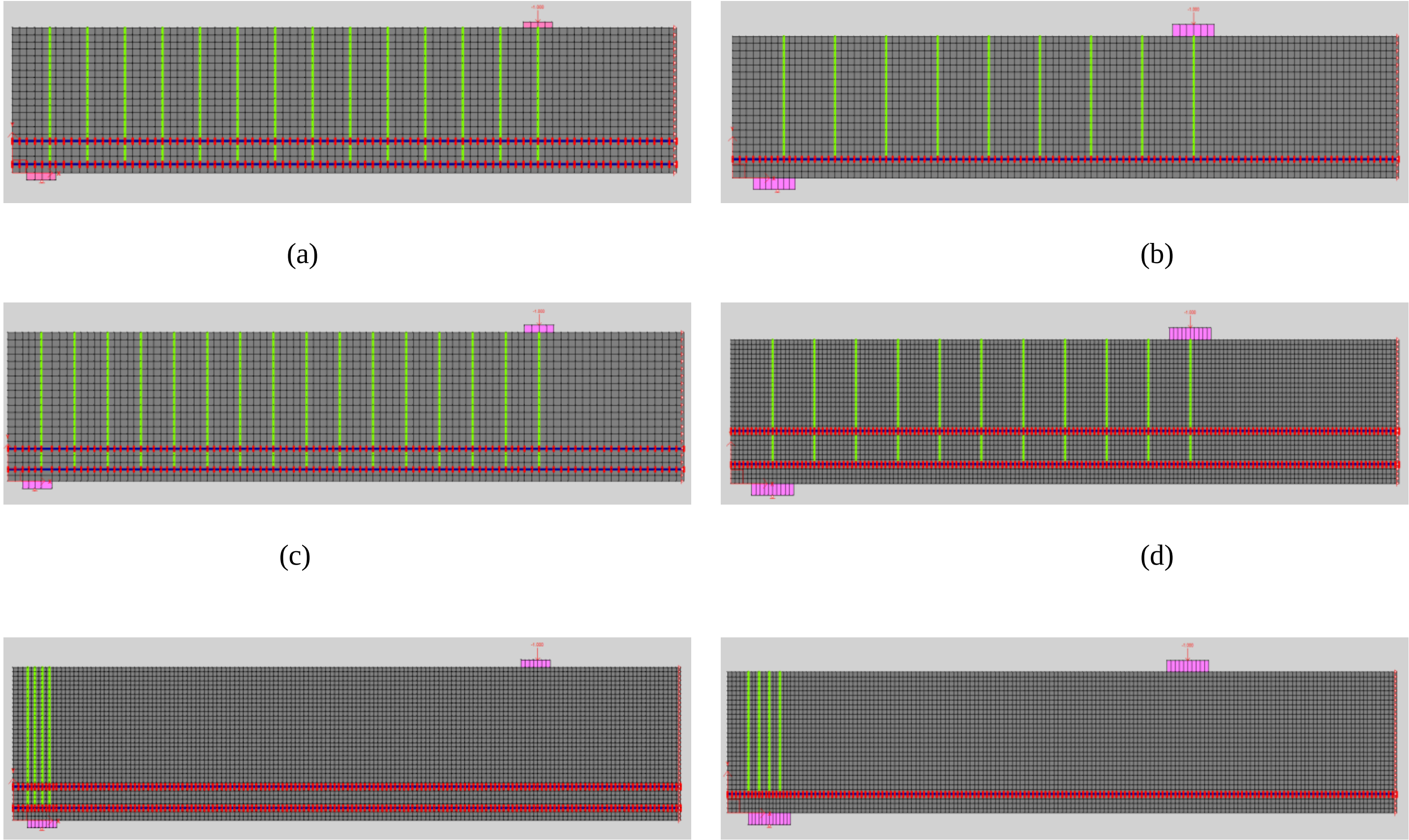

(a)

(b)

(c)

(d)

(e)

(f)

Figure 4.2. Finite element mesh of beams (a) D1 (b) D2 (c) D3 (d) D4 (e) D5 and (f) D6

Table 4.2. Values of input parameters for FE analysis of frost-damaged beams

Input Parameter	Value
E_c^d (MPa)	8,000
f_t^d (MPa)	1.5

Note: Values of input parameters E_c^d and f_t^d are calculated using Eqs. 3.1 and 3.2, respectively.

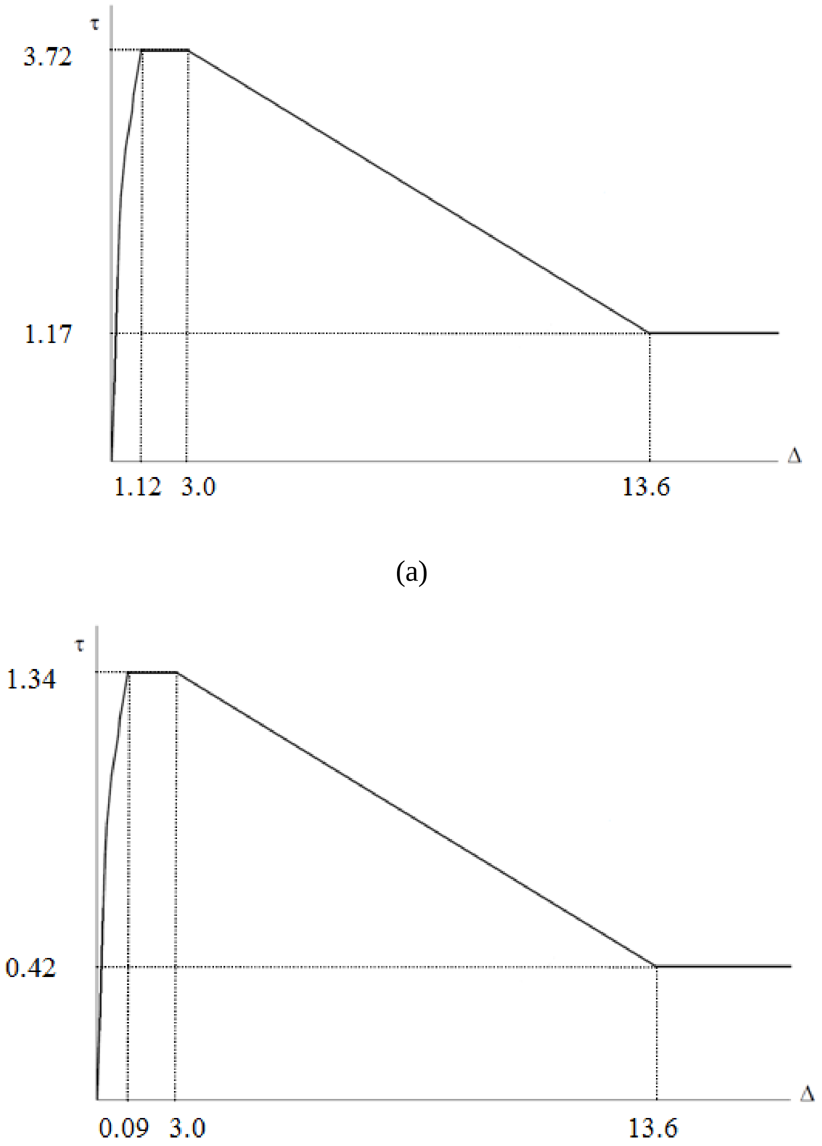

(a)

(b)

Figure 4.3. Bond stress-slip relationship for (a) confined bars and (b) unconfined bars (The bond stress-slip relationships were developed using Eqs. 3.3-3.24). Bond stresses in MPa and corresponding slips in mm

4.4 Results of FE Analysis

Failure in a reinforced concrete beam subjected to bending moment occurs due to either yielding of the reinforcement resulting from tension failure, crushing of concrete resulting from compression failure or yielding of steel and crushing of concrete occurring simultaneously (balanced condition). The failure mode depends on the reinforcement ratio. Tension failure results from under reinforcement, while compression failure is the result of over reinforcement. When the reinforcement in the beam is balanced, yielding of steel and crushing of concrete occur simultaneously. In the absence of sufficient transverse and longitudinal reinforcements, shear stresses can cause diagonal cracks form, which results in shear failure.

The beams tested by Hassanzadeh and Fagerlund (2006) were designed to fail in either of the modes discussed above. For the purposes of the subsequent discussion, the beams are categorized according to their respective failure mode and their cross-section size. The experimental and analytical load-deflection response of the beams as well as the crack distribution is discussed in the following sections. The analytical failure mode is determined from the maximum stress in the concrete and reinforcement at peak load.

4.4.1 Beam types 1 and 3: larger cross-section and flexural failure

Reinforcement in beam 1 consists of 4Ø20 longitudinal bars and 28Ø8 stirrups; the stirrups were evenly distributed within the shear span, and the beam was not heavily reinforced in the tension zone. It was, therefore, expected that the failure in beam R1 would be initiated by tension failure in reinforcement steel. The analysis showed that crushing of concrete and yielding of steel took place during peak load. Ductile was observed during experimental testing. Figure 4.4 shows the comparison between the experimental and numerical analysis load-deflection response for beams R1 and D1. From the analysis of beam R1, it is noted that yielding of the steel is followed by the crushing of concrete at a load and mid-span deflection of 361 kN and 29 mm, respectively. The stiffness and the load-carrying capacity were predicted relatively well by the numerical analysis.

Frost damage was induced in beam D1, thereby changing the mechanical properties of concrete and causing the reinforcement ratio to become greater than the reinforcement ratio of the balanced section. It was therefore expected that the beam would fail in a brittle manner, by crushing of concrete in the compression zone. This was confirmed by experimental and analysis results; see Figure 4.4. The deflection capacity of the beam was predicted relatively accurately by the analysis; the load at failure, however, was underestimated. The experimental load and deflection at failure was reported to be 305 kN and 38 mm, respectively, while the results of the analysis showed the load and deflection at failure to be 248 kN and 36 mm, respectively.

In the analysis of the reference beam, R1, flexural cracks developed at the onset of loading and continued to propagate until the beam failed due to the yielding of the steel reinforcement; see Figure 4.6(a). The crack pattern from the analysis of the damaged beam D1 showed the development of vertical flexural cracks followed by inclined flexural-shear cracks; see Figure 4.6(b).

Beam type 3 was designed similar to beam type 1; the reinforcement consists of 6Ø20 longitudinal bars and 32Ø8 stirrups. The experimental and finite element results of beam 3 are plotted in Figure 4.5. Beam R3 failed due to crushing of concrete in compression. This mode of failure was also observed in the FE analysis. The analysis predicted the stiffness as well as the load and deflection at failure of the beam relatively well. The analysis showed that vertical flexural cracks continued to develop in the beam until concrete crushing limited the load capacity; see Figure 4.6(c).

During experimental testing, beam D3 had failed due to concrete crushing in the compression zone. The mode of failure as well as the deflection capacity was accurately predicted by the FE analysis (Figure 4.5). However, the load capacity was underestimated. The authors reported the load and deflection capacity of beam D3 to be 325 kN and 32 mm, respectively, and the analysis predicted 277 kN and 33 mm, respectively. The crack pattern from the analysis showed that, similar to beam R3, bending cracks began to form at a low level of loading and continued to propagate until the crushing of concrete; see Figure 4.6(d).

The discrepancy between the experimental and analytical results for beams D1 and D3 can be attributed to uneven damage distribution over a cross-section; it has been reported in the literature that the internal damage progresses from the surface into the concrete beam subjected to freeze-thaw cycles (Petersen *et al.*, 2007). It was observed by Hassanzadeh and Fagerlund (2006) that in beams with larger cross section, the degree of damage was less at the inner part of the beams. In modelling the frost-damaged beams, the compressive strength was used to quantify the damage and used as an input. The compressive strength of frost-damaged concrete was determined from tests on concrete cores drilled from frost-damaged blocks. Due to the fact that the dimensions of the block ($1m$ x $0.4m$ x $0.2m$) were smaller than the beams type 1 and 3, it can be concluded that the damage was not indicative of the damage in the larger beam, as the damage in the block would be greater than that experienced by the beams D1 and D3. Additionally, the drilled cores used for testing were 80 mm in length, while the height of the beam was 500 mm. The value of compressive strength, then, does not take into account the strength of the inner concrete core of the beam. For these reasons, numerical analysis underestimated the load-carrying capacity of the frost-damaged beams, D1 and D3, as the input parameter quantifying this damage was assumed to uniform throughout the beam.

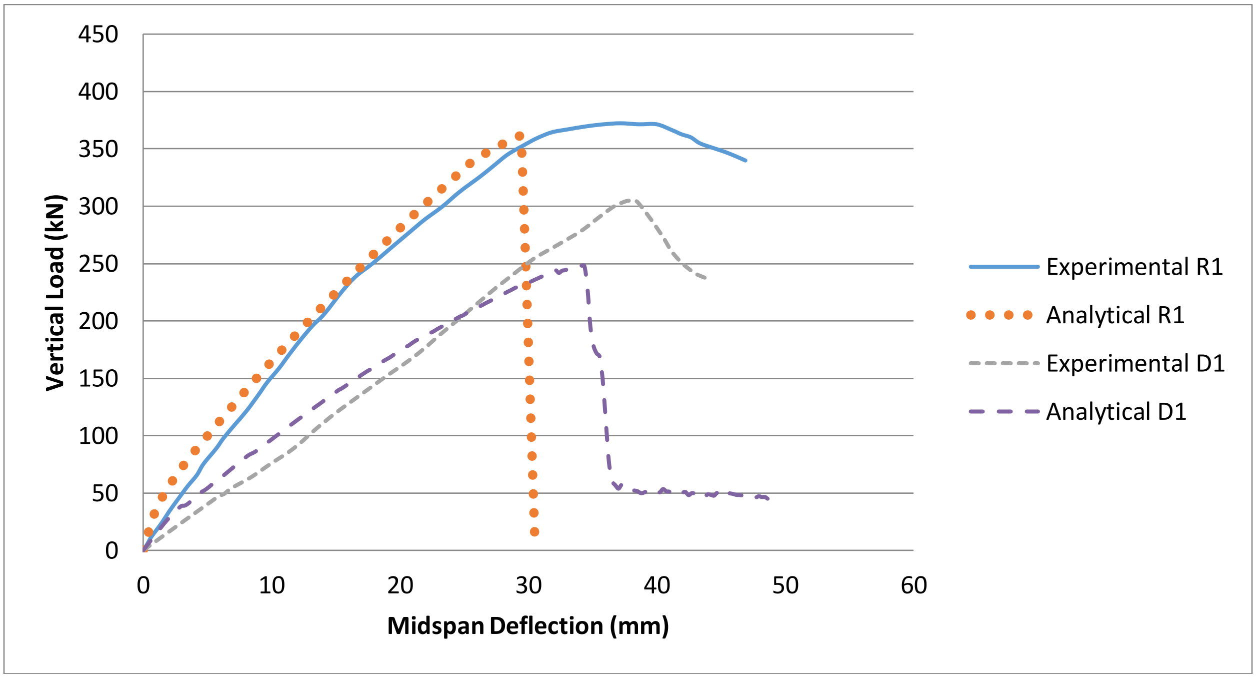

Figure 4.4. Load-deflection response of beam type 1

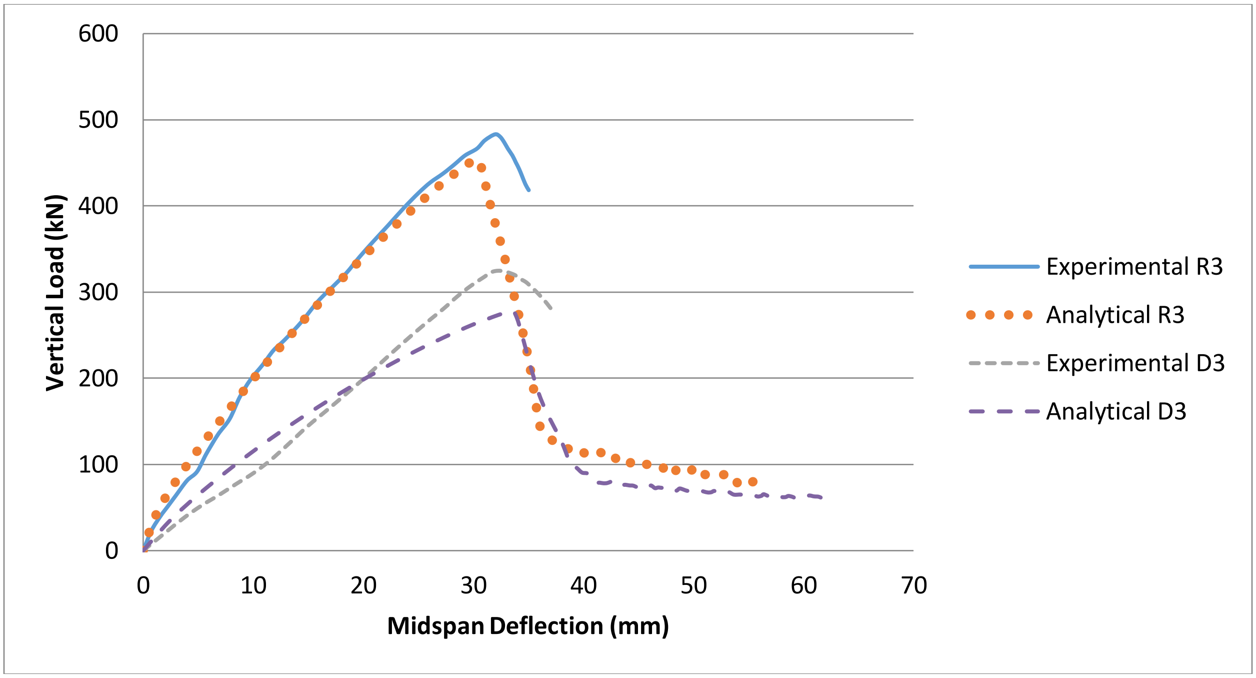

Figure 4.5. Load-deflection response of beam type 3

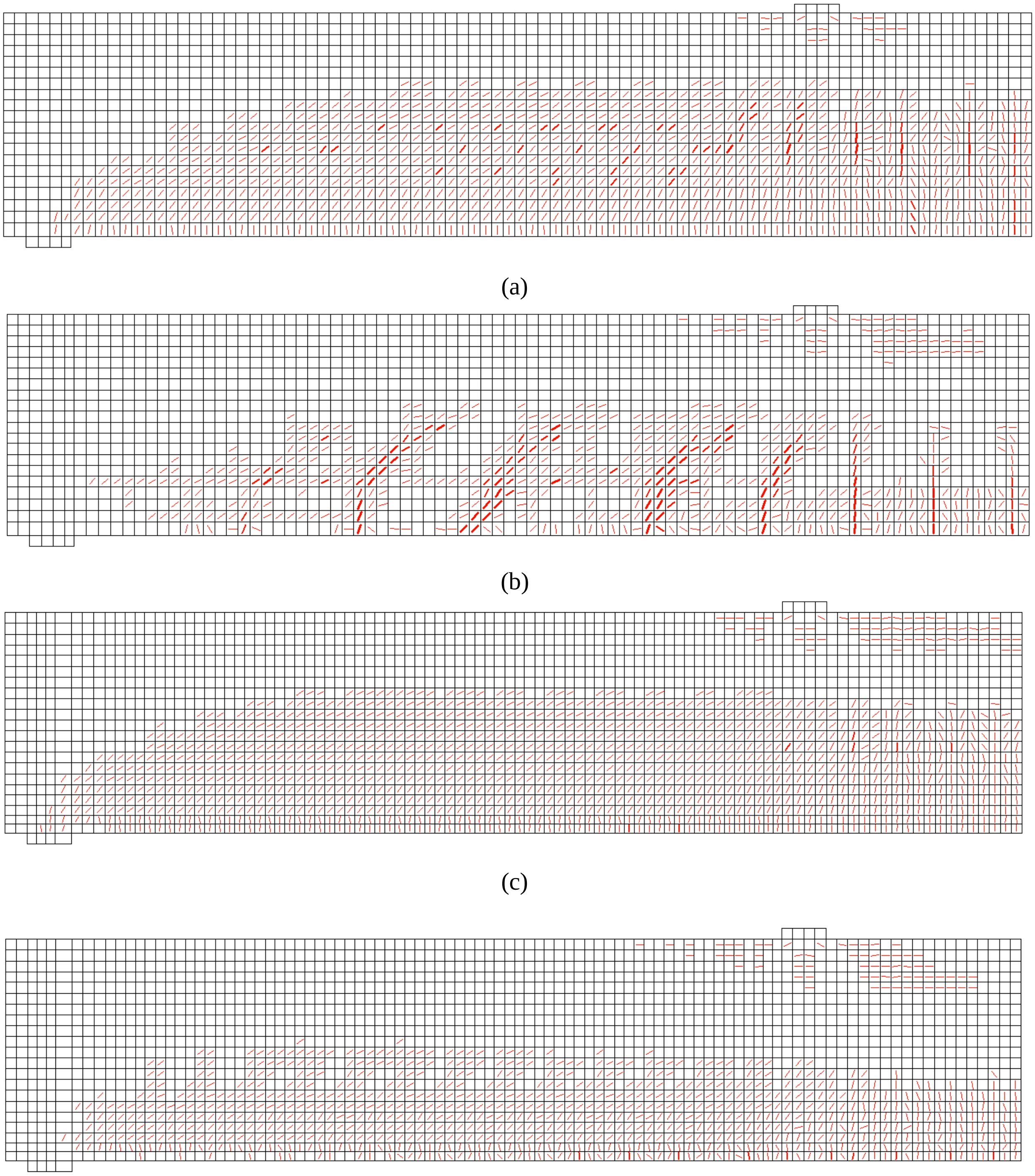

(a)

(b)

(c)

(d)

Figure 4.6. Crack pattern of beams (a) R1 (b) D1 (c) R3 (d) D3

4.4.2 Beam types 2 and 4: smaller cross-section and flexural failure

Reinforcement in beam type 2 consisted of 3Ø20 longitudinal bars and 18Ø8 stirrups closely spaced. The reference beam R2 was, therefore, expected to fail in bending either by yielding of steel or crushing of concrete. A ductile failure was predicted by the numerical analysis; the yielding of steel reinforcement was followed by crushing of concrete. This agrees with what was observed during the experimental testing. Figure 4.7 shows the comparison between numerical and experimental results in terms of load-displacement curves for type 2 beams. The numerical analysis predicted the load-carrying capacity relatively well. The crack pattern from the analysis showed the propagation of bending cracking along the tensile reinforcement until failure; see Figure 4.9(a).

The damaged beam, D2, failed due to crushing of concrete in the compression zone. The analysis results were in agreement with the mode of failure observed during experimental testing; the stiffness and the load-carrying capacity was, however, slightly overestimated (Figure 4.7). The experimental load and deflection at failure were reported to be 140 kN and 24 mm, whereas the analysis provided a peak load and deflection at peak load of 158 kN and 25 mm, respectively. Prior to failure, diagonal cracks had formed in the beam; see Figure 4.9(b). However, the beam failed in compression.

Beam type 4 had high bending reinforcement content of 5Ø20 bars and closely spaced 22Ø8 stirrups. The reference beam R4 was expected to fail in a brittle manner due to crushing of concrete in compression prior to yielding of reinforcement. This failure mode was observed during the experimental testing and was captured by the numerical analysis. Figure 4.8 shows the comparison between the experimental and numerical analysis load-deflection responses for beam R4. The analysis of the beam showed the initiation and propagation of flexural cracks as loading was applied to the beam; see Figure 4.9(c).

Beam D4 also failed in a brittle manner; the capacity was limited by crushing of concrete in the compression zone. The load-deflection response and the stiffness were accurately predicted by the numerical analysis; the experimental and analytical load deflection curves are shown in Figure 4.8. Before failure, inclined flexural-shear cracks had developed in the beam; see Figure 4.9(d).

The numerical analysis slightly overestimated the load-carrying capacity of the damaged beams with smaller cross-section and flexure failure. The discrepancy between the experimental and numerical results can be attributed to the direction of the visible cracking that was observed by Hassanzadeh and Fagerlund (2006) after the beams had undergone freeze-thaw cycles. For the other types of damaged beams, the authors reported that cracks that formed as a result of frost damage were largely parallel to the longitudinal axis of the beam. However, the authors reported that frost-induced cracks in beams with smaller cross-section and flexure failure were not parallel to the longitudinal axis of the beams as other beams, but rather they were perpendicular (Hassanzadeh and Fagerlund 2006). The significance of the orientation of cracks in relation to the cross section size of the beams was not commented on by the authors. The orientation of the cracks in a beam has a significant influence on the response of the beam when it is subject to loading. When the cracks are oriented in the direction of compressive stresses, i.e., cracks are perpendicular to the direction of the longitudinal axis of the beam, delamination occurs. In modelling the frost-damaged beams, this effect was not taken into consideration and therefore, the analysis provided a slight over estimation of the failure loads.

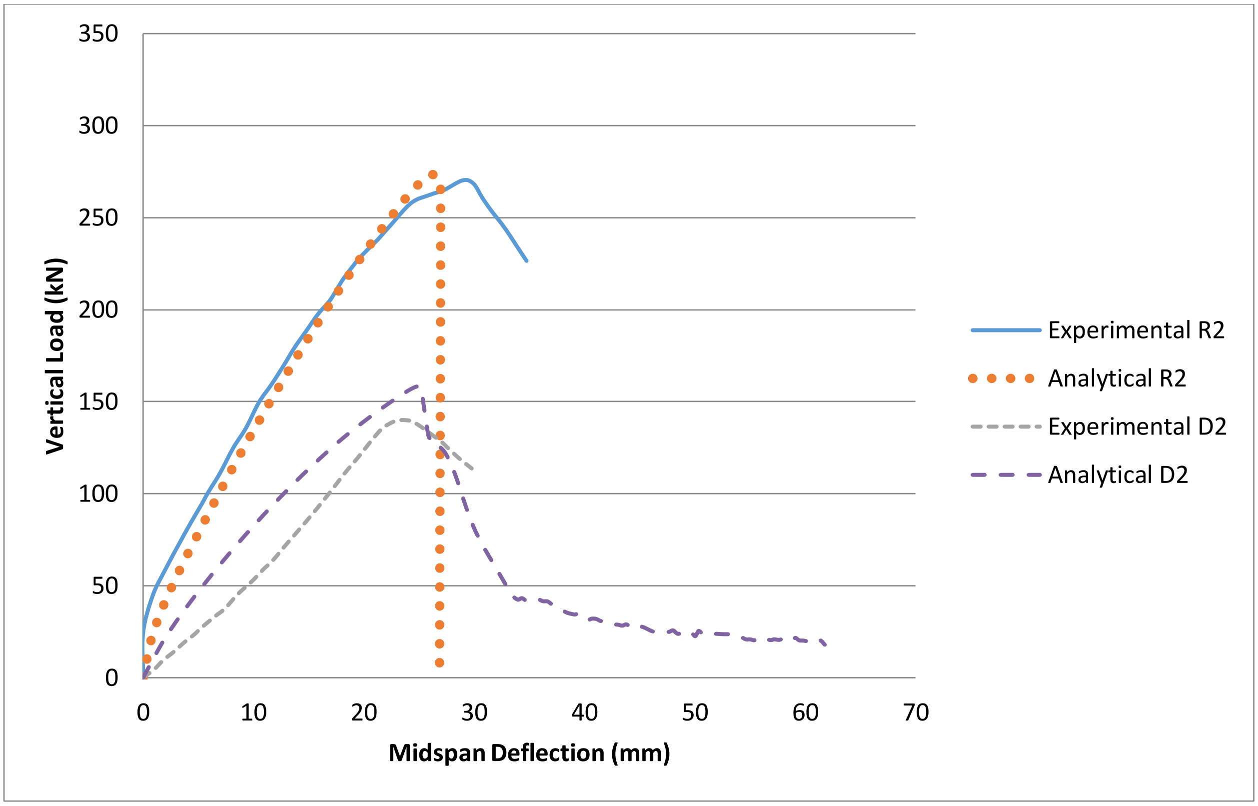

Figure 4.7. Load-deflection response of beam type 2

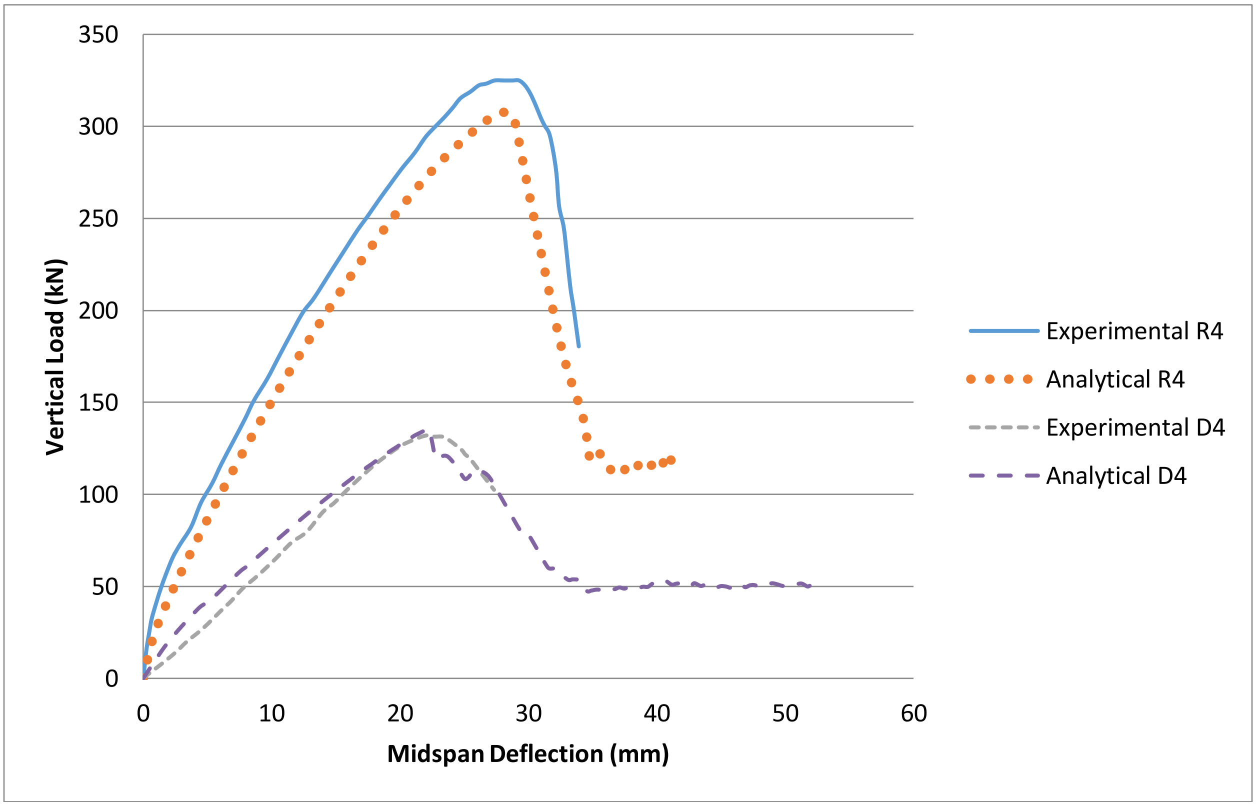

Figure 4.8. Load-deflection response of beam type 4

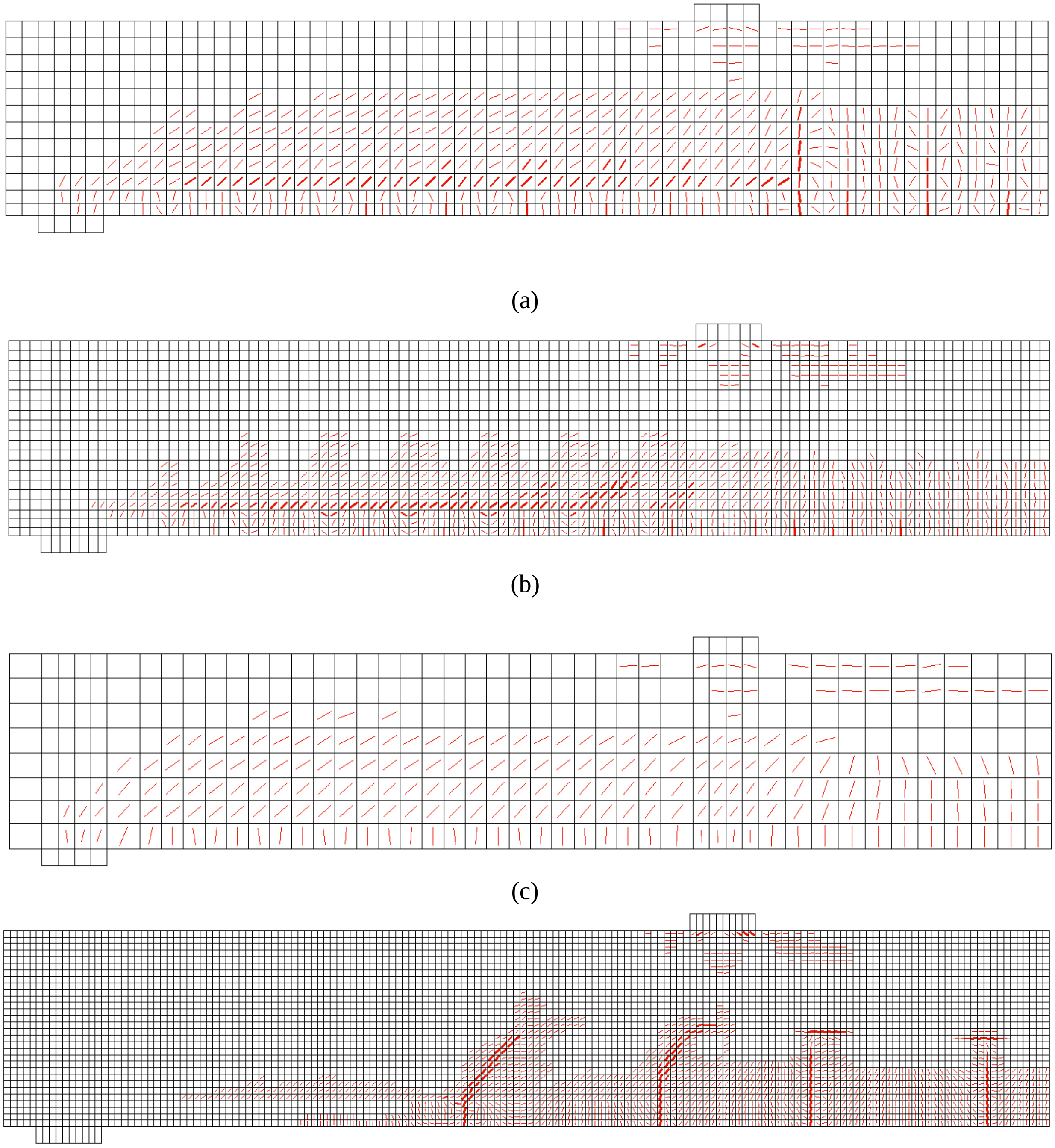
(a)

(b)

(c)

(d)

Figure 4.9. Crack pattern of beams (a) R2 (b) D2 (c) R4 (d) D4

4.4.3 Beam types 5 and 6: shear failure

Beam type 5 was designed similar to beam type 1, but with stirrups only at the supports. For the reference beam R5, Hassanzadeh and Fagerlund (2006) reported shear failure, resulting from inclined cracks at a load of 215 kN. The analytical load-deflection curve in Figure 4.10 shows a peak load of 217 kN. The curve had two peak loads, which can be explained by considering the crack pattern from the analysis as illustrated in Figure 4.12(a); flexural cracks developed at the onset of loading which resulted in a change in the initial stiffness. This was followed by initiation of shear cracking that propagated to the tensile reinforcement and resulted in the first peak load in the load-deflection curve. Longitudinal cracks progressed along the tensile reinforcement to the supports, where vertical cracks formed and resulted in failure at the second peak load.

Similar to beam R5, inclined cracking governed the failure of the damaged beam, D5. The experimental and analytical load-deflection curves are shown in Figure 4.10. It can be observed that the analysis overestimated the initial stiffness; however, the failure load was predicted relatively well. The analysis showed that inclined shear cracking governed the failure of the beam; see Figure 4.12(b).

The reinforcement in beam type 6 consisted of 3Ø20 longitudinal bars. The transverse reinforcement content was the same as that of beam type 5; however, beam type 6 had a smaller cross section. It was therefore expected that the effects of frost damage would be more extensive in beam type 6. From experimental observation, the reference beam R6 and beam D6 both failed due to inclined shear cracking. This failure mode was also observed in the analysis of the beams. The experimental and analytical load-deflection curves of beams R6 and D6 are shown in Figure 4.11. The load capacity of beam R6 was predicted relatively well; however, for the damaged beam, D6, the analysis grossly overestimated the stiffness and underestimated the deflection at peak load. The crack patterns from the analysis of beams R6 and D6 are shown in Figures 4.12(c) and 4.12(d), respectively. The initiation and propagation of diagonal cracks resulted in shear failure.

Concrete is not a perfectly brittle material; when concrete cracks, it is able to resist tensile stresses across the crack. As the crack width increases, there is a decrease in the post cracking tensile stresses. Concrete can transmit tensile stresses after cracking due to tension softening, and the model used in the analysis to account for this effect is based on the energy of fracture, G_f. Under shear loading, stresses are also transferred over the crack through friction. However, since only the fracture energy of plain concrete was taken into account to define the stress-strain relationship of the concrete for the analysis, the load-carrying capacity of the beams was underestimated.

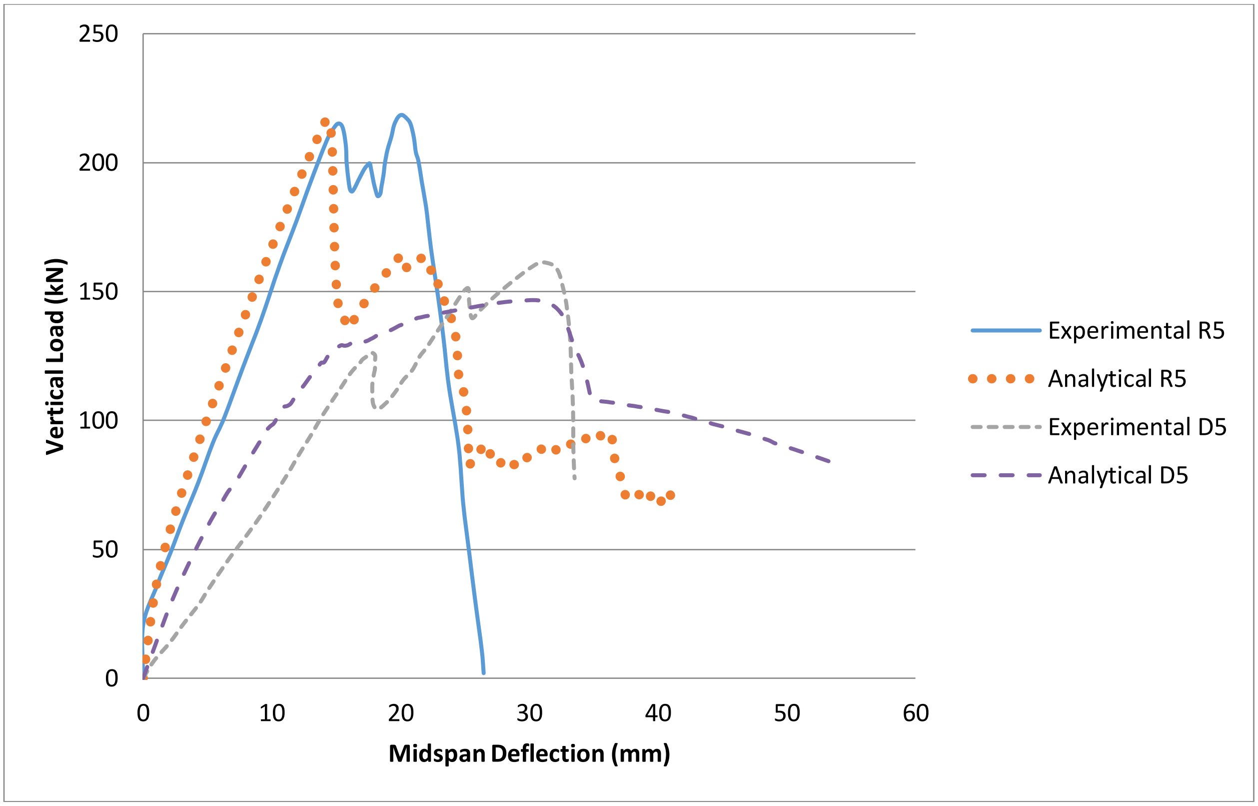

Figure 4.10. Load-deflection response of beam type 5

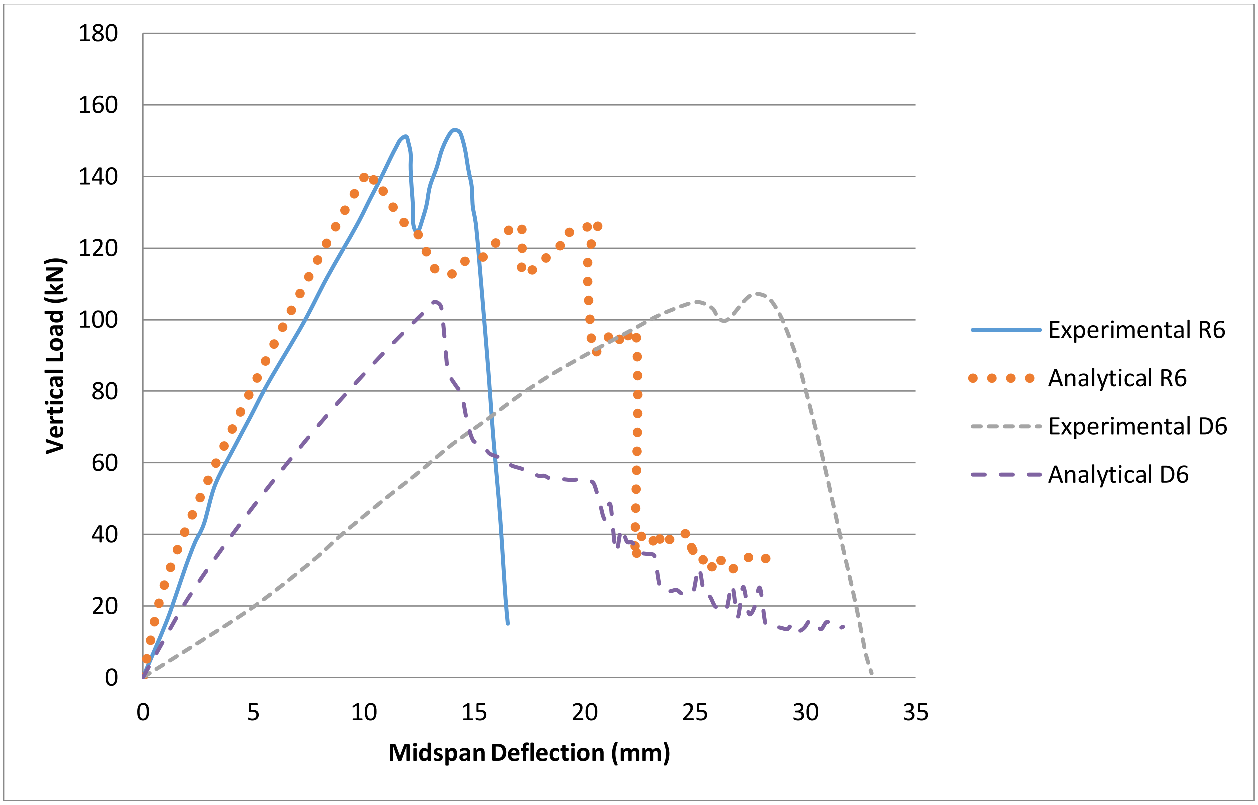

Figure 4.11. Load-deflection response of beam type 6

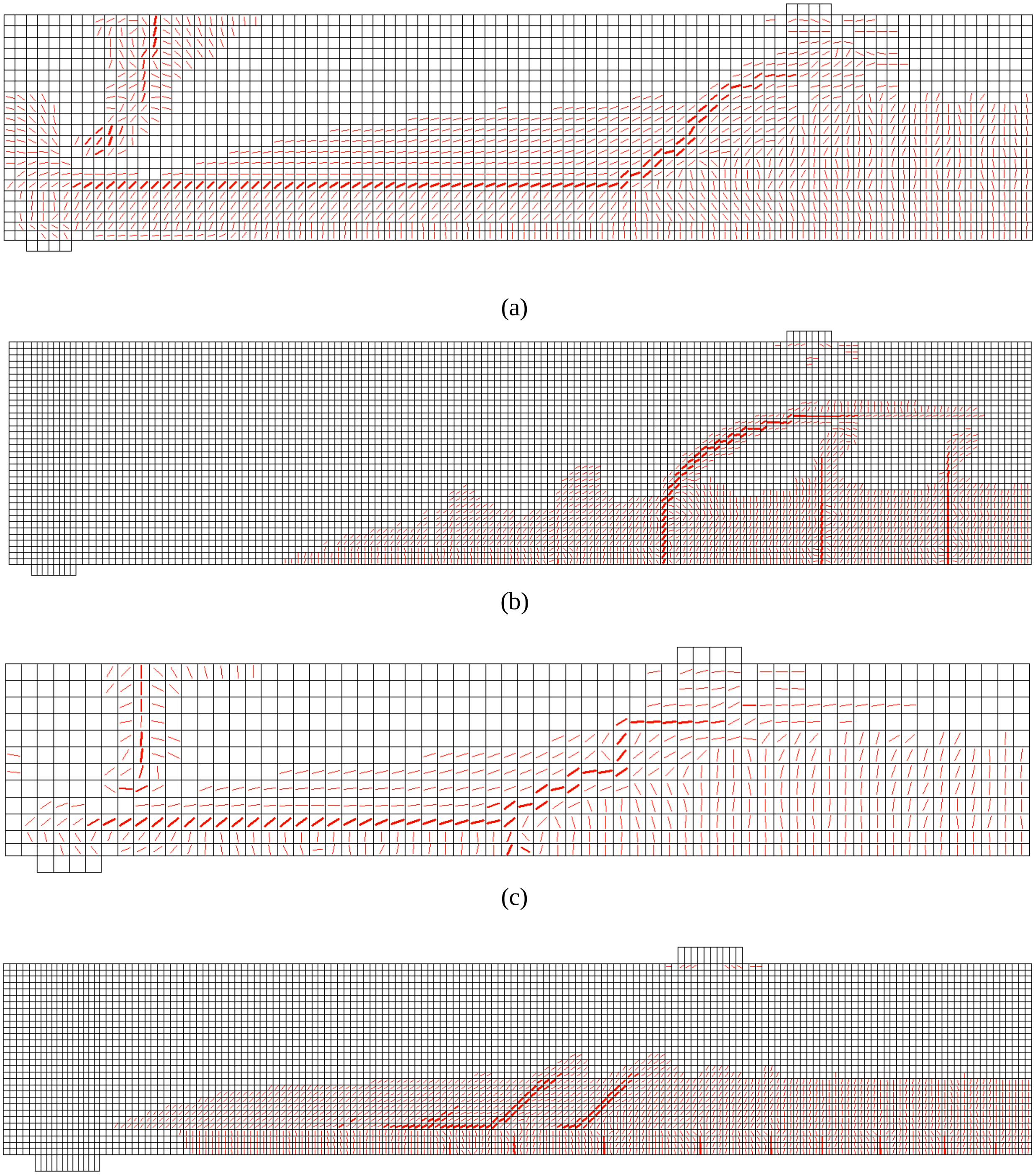
(a)
(b)
(c)
(d)

Figure 4.12. Crack pattern of beams (a) R5 (b) D5 (c) R6 (d) D6

4.5 Discussion of FE Analysis and Summary of Results

Comparison of results from experiments and numerical analyses in terms of maximum load and deflection at the peak load is presented in Table 4.3 and Figure 4.13; the table and figure show how well the analysis is able to predict the load and deflection capacity of frost-damaged beams when the proposed methods are applied. It can be observed that the analysis provided a better estimate of the load-deflection response of reference beams. With the exception of beams D2 and D4, the failure load and deflection of all frost-damaged beams was underestimated. Beams D1 and D3 had larger cross sections and therefore had less damage, which was not reflected in the input value of the compressive strength, assumed to be uniform throughout. The slight overestimation of the load capacity of beams D2 and D4 was due to the orientation of the freeze-thaw induced cracks; the direction of the cracks affected the fracture behaviour of concrete in compression, which was not accounted for in the analysis. The analysis was not able to accurately capture the stiffness degradation of shear critical beams, D5 and D6, and underestimated the peak load. The load-carrying capacity was underestimated because the effects of friction across the shear crack were not accounted for in the analysis; tension softening of concrete was determined by considering only the fracture energy of concrete.

A comparison of the analysis results with the experimental data indicates that, in general, the effect of frost damage on the load-carrying capacity and the changes in failure mode can be predicted by using the proposed methodology; see table 4.3 for statistical figures representing the dispersion of the results.

Table 4.3. Comparison of experimental and numerical results in terms load-deflection capacity

Beams		Deflection (mm)			Load (kN)		
		FEA Result	Experimental Result	FEA/Exp.	FEA Result	Experimental Result	FEA/Exp.
Reference	R1	29.44	37.19	0.79	360.94	372.26	0.97
	R2	26.13	28.97	0.90	273.52	270.26	1.01
	R3	29.98	31.96	0.94	451.93	483.11	0.94
	R4	27.90	29.27	0.95	307.83	324.96	0.95
	R5	14.45	15.10	0.96	216.57	215.03	1.01
	R6	10.35	11.92	0.87	141.30	151.20	0.93
	Mean			0.90	Mean		0.97
	Standard Deviation			0.064	Standard Deviation		0.035
	COV (%)			7.06	COV (%)		3.61
Damaged	D1	36.46	37.81	0.96	248.06	304.82	0.81
	D2	24.91	23.29	1.07	158.31	139.94	1.13
	D3	33.19	32.23	1.03	277.18	324.80	0.85
	D4	22.23	22.31	1.00	135.20	132.26	1.02
	D5	30.33	30.76	0.99	146.67	161.10	0.91
	D6	14.25	27.94	0.51	105.12	109.11	0.96
	Mean			0.93	Mean		0.95
	Standard Deviation			0.207	Standard Deviation		0.116
	COV (%)			22.37	COV (%)		12.26

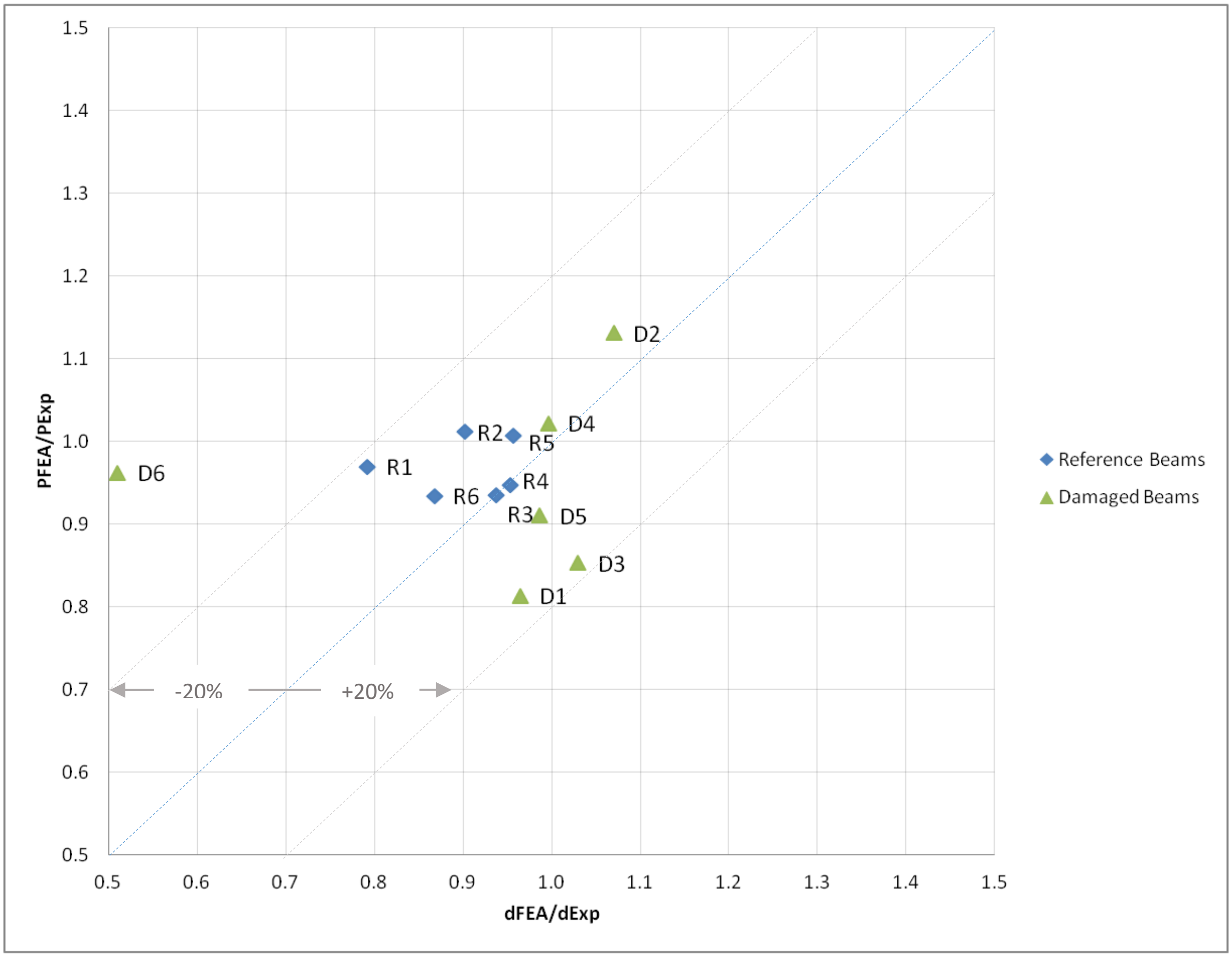

Figure 4.13. Comparison of experimental and numerical results in terms load-deflection capacity

Chapter 5. Parametric Analysis

5.1 Introduction

This chapter presents a parametric study of the effect of external and internal parameters in frost damage affecting reinforced concrete, using the methodology that was proposed and validated in Chapters 3 and 4, respectively. The influence of each parameter on the damage degree and the subsequent reduction in the load capacity is investigated. The test specimen used for the parametric analysis was designed in accordance with CSA A23.3. The results and a discussion of the results are also presented in this chapter.

5.2 Test Specimen

The beam designed to perform the parametric analysis is shown in Figure 5.1. The geometry of the beam is characterized by 4.4 m span and two concentrated loads with a shear span of 1.8 m. The height, h and the width, b of the cross section is 500 mm and 200 mm, respectively. The reinforcement of the beam consists of 4∅20 longitudinal bars and 28∅8 stirrups. It was designed to fail in bending. The compressive strength, f_c of the beam is 37.5 MPa. The reinforcement ratio and balance ratio are respectively ρ=1.25% and ρ/ρ_{bal}=0.84.

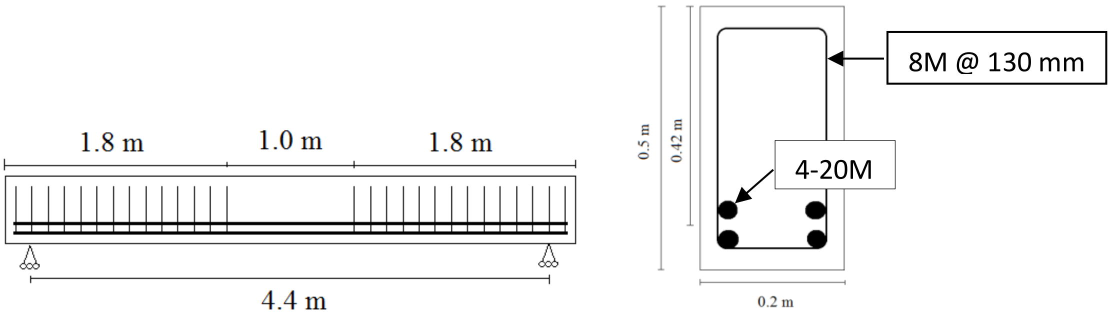

Figure 5.1. Geometry of beam used in parametric analysis

The beam was designed to meet the requirements of CSA A23.3. Table 5.1 shows validation of the design in accordance with code provisions.

Table 5.1. CSA A23.3 requirement check for validation of beam design

Requirement		Requirement Check
Minimum reinforcement	$M_r \geq 1.2M_{cr}$	$\rho = 1.5\%, f'c = 37.6\ MPa\ K_r = 4.5$ $M_r = K_r bd^2 = 157\ kN.m$ $M_{cr} = \lambda 0.6\sqrt{f'c}\ bth^2/6 = 31\ kN.m$ $1.2M_{cr} = 37\ kN.m$ $M_r \geq 1.2M_{cr}$ ✓
	$A_s \geq A_{s,min}$	$A_{s,min} = \frac{0.2\sqrt{f'c}bth}{f_y} = 307\ mm^2$ $A_s = 1256\ mm^2$ $A_s \geq A_{s,min}$ ✓
Detailing	Concrete cover	Class F: concrete exposed to freeze thaw 40 mm minimum concrete cover ✓
	Bar spacing requirements	clear distance, s shall not be less than: (1) 1.4 times the bar diameter (1.4 d_b) (2) 1.4 times the maximum size of coarse aggregate (1.4 a_{max}) (3) 30 mm s_{min}= 30mm ✓
Serviceability	Control of Flexural Cracking at Service Load	$z = f_s\ (d_c\ A)^{1/3}$ $z = 18{,}809\ N/mm \leq 25{,}000\ N/mm\ (exposed\ condition)$ ✓

5.3 Parameters

The objective of the parametric study was to investigate parameters that influence the damage caused by successive freeze-thaw cycles in reinforced concrete flexural members. The number of freeze-thaw cycles is an external variable that was investigated as part of the study. Internal variables were also considered and include moisture content and air content.

Degree of saturation, S is a critical factor influencing the freeze-thaw resistance of concrete. Frost damage will not occur after a large number of freeze-thaw cycles if the degree of saturation is below the critical degree of saturation, S_{cr}. Experimental investigation is required to determine the value of the critical degree of saturation for a specific concrete type, and it is marginally affected by repeated freeze-thaw cycles. When the pore saturation is above the critical value, there is a fatigue effect resulting from successive freeze-thaw cycles. The damage caused by increasing S above the critical value, S_{cr} is linear and is described as a function of the number of freeze-thaw cycles *N*, as given by the following expressions (Fagerlund 1995):

$$S < S_{cr};\ D = 0\ \ for\ N \quad (5.1)$$

$$S > S_{cr};\ D = K_N(S - S_{cr}) \quad (5.2)$$

where D is damage expressed as loss in dynamic modulus of elasticity (see Figure 5.2), and K_N is a coefficient of fatigue, given by:

$$K_N = \frac{A.N}{B + N} \quad (5.3)$$

where *A* and *B* are empirical constants.

From a study on the effect of the number of freeze-thaw cycles on the critical degree of saturation, specimens with a water-cement ratio of 0.40 had a value of S_{cr}=0.77 (Romben 1973). The coefficient K_N was recorded to have the following value as shown in Table 5.2 for different number of freeze-thaw cycles.

Table 5.2. Experimental values of K_N for different number of cycles

N	K_N
1	0.23
4	0.62
10	0.77
45	1.08
78	1.08

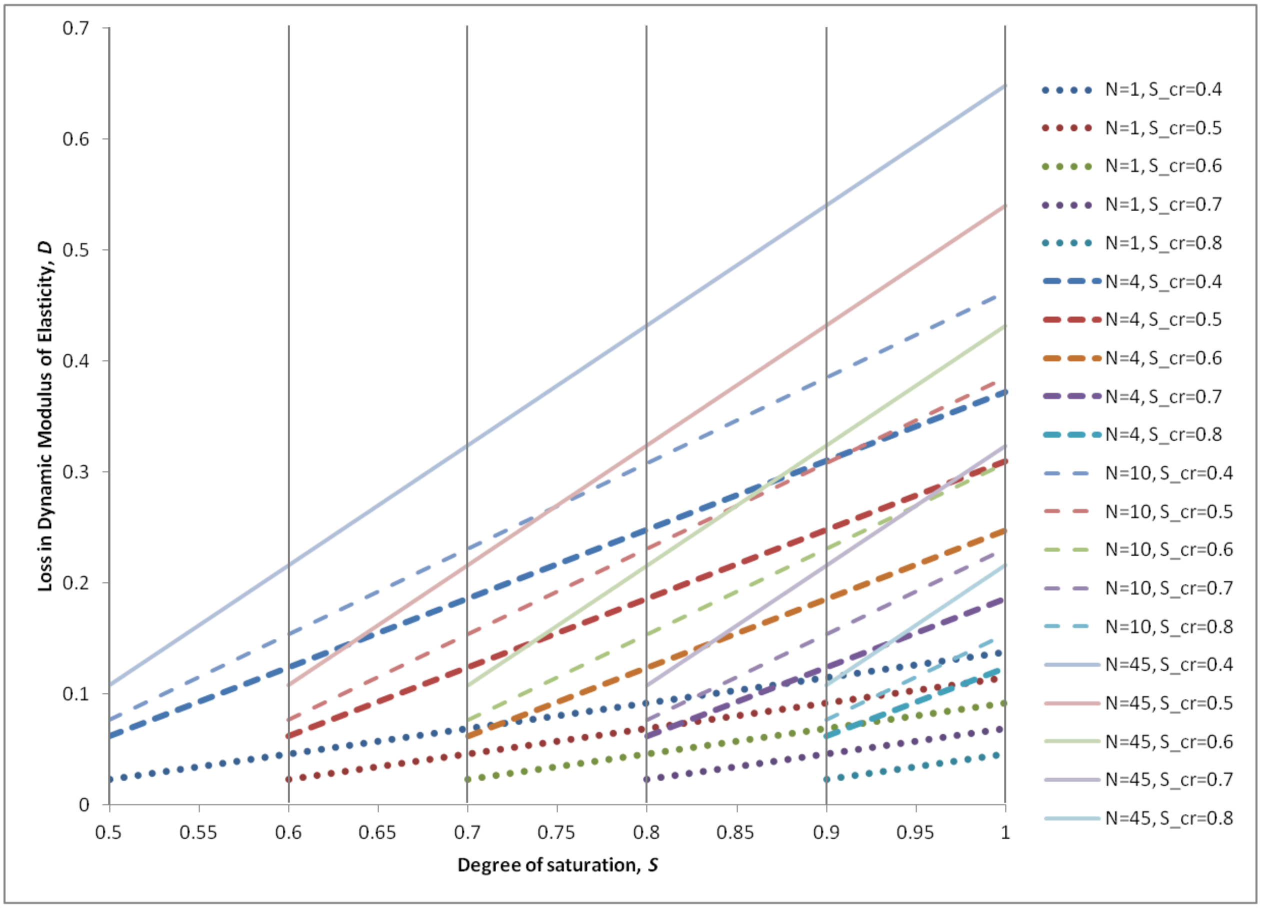

Figure 5.2. Relationship between loss in dynamic modulus of elasticity, D and degree of saturation, S (for various values of N and S_{cr})

By fitting Eq. 5.3 to the experimental data in Table 5.2, the following relationship for K_N was therefore proposed for concrete with a water-cement ratio of 0.40 to relate the degree of frost damage to the number of freeze-thaw cycles:

$$K_N = \frac{1.18 \cdot N}{(4.1 + N)} \tag{5.4}$$

Figure 5.3 shows how the analytical values of coefficient K_N relating the degree of damage to number of freeze-thaw cycles from Eq. 5.4 compare to the experimental values in Table 5.2.

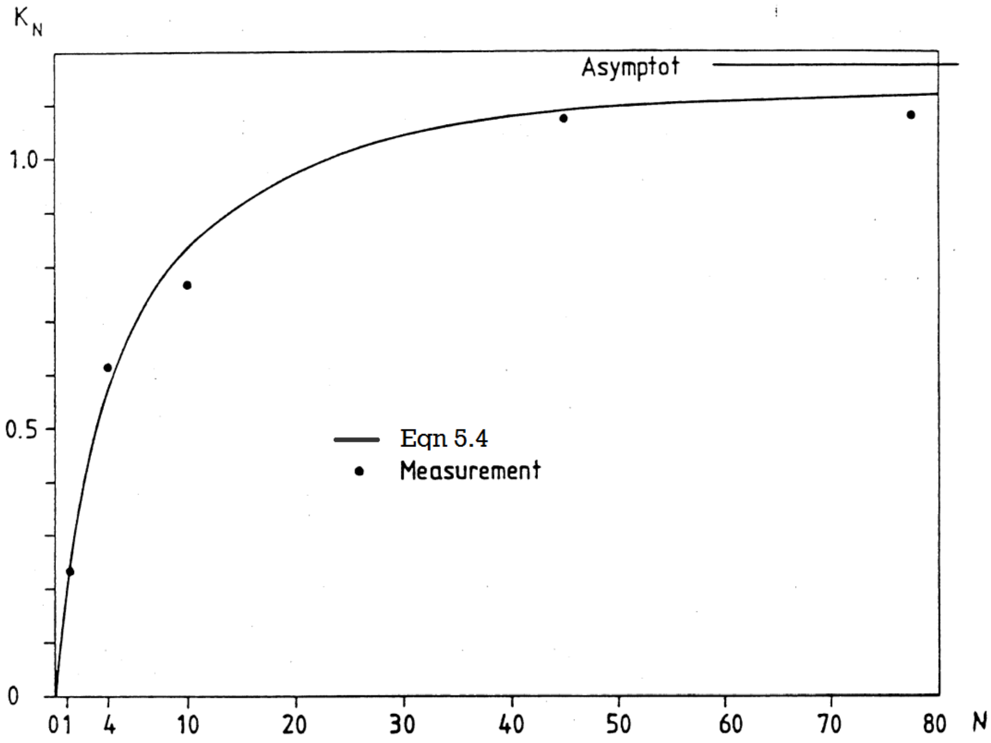

Figure 5.3. Comparison between experimental and analytical values of coefficient K_N relating the degree of damage to number of freeze-thaw cycles (reproduced from Fagerlund 1995)

The subsequent sections are a discussion on how each of the parameters were varied, whereby the effect of each one on the behaviour of the reinforced concrete beam could be identified.

5.3.1 Number of Freeze-Thaw Cycles

To determine the effects of repeated freeze-thaw cycles on the degree of frost damage, S_{cr} and S in Eq. 5.2 were set to constant values of 0.77 and 1, respectively, while the coefficient of fatigue, K_N was varied according to selected values of N assuming the concrete in the beam has a w/c of 0.4. The corresponding loss of dynamic modulus, as expressed by the damage index D, was then applied to the beam. It was also of interest to consider the effects of repeated freeze-thaw cycles on the loss of concrete weight caused by surface scaling. The method to model surface scaling is discussed in Chapter 3. Since both internal frost damage and salt scaling can occur concurrently, they were considered together in the analysis. The damaged was applied as change in the material property, E_c and change in the cross-section geometry of the beam.

Climate data published by the Government of Canada was used to determine the number of freeze-thaw cycles over a period of 74 years for different cities in Canada, including Calgary, Ottawa and St. John's. This data is shown in Figure 5.4. A freeze-thaw cycle was assumed to have occurred when a temperature of 18℃ or higher was reached, followed by a recorded minimum temperature of -18℃ or lower. This is a definition consistent with what other researchers have defined in their respective experimental works (Hanjari *et al.* 2011, Hassanzadeh and Fagerlund 2006); however, it does not correspond to a freeze-thaw cycle as defined in the field (i.e., temperature cycles above and below 0°C). The former definition was adopted because all expressions for mechanical properties and constitutive behaviour of frost-damaged concrete reported in Chapter 3 and used in the analysis were obtained from experimental testing that involved similar temperature ranges.

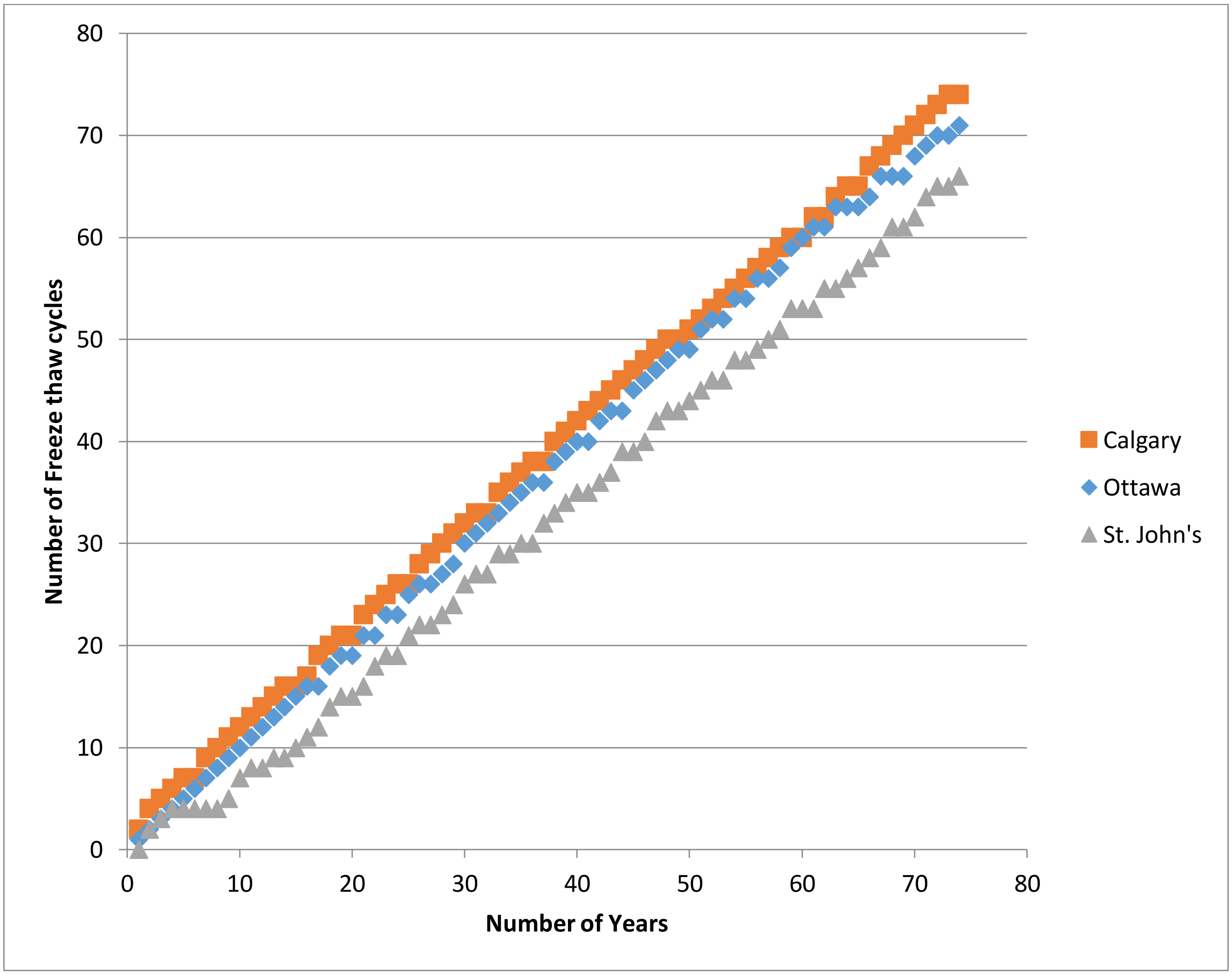

Figure 5.4. Number of freeze-thaw cycles over a period of 74 year in Calgary, Ottawa and St. John's

It was of interest to capture how the progression of damage translates into loss in the load-carrying capacity of a beam after it has been in service for 10 years, 25 years and 74 years in the three Canadian cities. Table 5.3 shows the values of N, the calculated loss in the dynamic modulus of elasticity according to Eq. 5.2, as well as the scaling depth after 10, 25 and 74 years according to Eqs. 3.25 and 3.26. The damaged was applied to the beam as change in material property, E_c and change in the cross-sectional geometry of the beam. It was assumed that the loss of E_c was homogenous throughout the beam, and surface scaling occurred uniformly along the perimeter of the cross section. The input values of E_c , f_c^d and f_t^d for the analysis are shown in Table 5.4, where f_c^d and f_t^d are calculated using Eqs. 3.1 and 3.2, respectively.

Table 5.3. Loss in the dynamic modulus of elasticity and the scaling depth for N freeze-thaw cycles

City	@ year 10			@ year 25			@ year 74		
	N	D (%)	s (mm)	N	D (%)	s (mm)	N	D (%)	s (mm)
Calgary	12	20.23	0.255	26	23.44	0.553	74	25.72	1.573
Ottawa	10	19.25	0.213	25	23.32	0.531	71	25.66	1.509
St. John’s	7	17.12	0.149	21	22.71	0.446	66	25.55	1.403

Table 5.4. Input values of E_c, f_c^d and f_t^d for numerical analysis

City	Undamaged				@ year 10				@ year 25				@ year 74			
	N	E_c (GPa)	f_c^d (MPa)	f_t^d (MPa)	N	E_c (GPa)	f_c^d (MPa)	f_t^d (MPa)	N	E_c (GPa)	f_c^d (MPa)	f_t^d (MPa)	N	E_c (GPa)	f_c^d (MPa)	f_t^d (MPa)
Calgary	0	33.7	37.5	2.02	12	26.9	27.3	2.43	26	25.8	26.7	2.37	74	25.0	26.2	2.32
Ottawa	0	33.7	37.5	2.02	10	27.2	27.5	2.44	25	25.8	26.7	2.37	71	25.0	26.2	2.32
St. John’s	0	33.7	37.5	2.02	7	27.9	27.9	2.48	21	26.0	26.8	2.38	66	25.1	26.2	2.32

5.3.2 Moisture Content

The degree of saturation was varied between values of 0.77 and 1 to determine its effects on the loss in loss in dynamic modulus of elasticity. Equation 5.2 was used to quantify the damage; S_{cr} was set to a value of 0.77, while the coefficient of fatigue, K_N for 45 freeze-thaw cycles was 1.08. The values of K_N for 45 freeze-thaw cycles was selected for the analysis because it corresponds to the number of freeze-thaw cycles at which the fatigue limit is reached, i.e., after 45 cycles, K_N cannot exceed 1.08 even when N=∞; see Table 5.2 and Figure 5.3.

The damaged was applied to the beam as change in material property, E_c. The loss in dynamic modulus of elasticity (%) calculated using Eq. 5.2 and the input value of E_c , f_c^d and f_t^d for the analysis are shown in Table 5.5, wherein f_c^d and f_t^d are calculated using Eqs. 3.1 and 3.2, respectively.

Table 5.5. Loss in dynamic modulus of elasticity for different moisture content and the corresponding input values of E_c, f_c^d and f_t^d for numerical analysis

S	D (%)	E_c (GPa)	f_c^d (MPa)	f_t^d (MPa)
0.8	3.2	32.6	30.7	2.75
0.9	14.0	29.0	28.6	2.54
1	24.8	25.3	26.4	2.34

5.3.3 Air Content

The effects of varying the volume of entrained air on the freeze-thaw resistance of concrete was examined through varying the critical degree of saturation, S_{cr} .

Yang *et al*. (2011) carried out experiments to investigate the effects of air entrainment on the mechanism of frost damage. The degree of saturation and porosity was measured in order to determine the critical degree of saturation of concrete with different air contents and water/cement ratios. It was observed that the air content was the main factor influencing the critical degree of saturation rather than the water/cement ratio. It was also observed that the critical degree of saturation decreased with increasing air content.

The mix designs of the concretes tested by Yang *et al*. (2011) are shown in Table 5.6. As the air content in air-entrained concrete increases, the compressive strength decreases. The water/cement ratio of air-entrained concrete therefore had to be adjusted to ensure that the strength was the same as that of non-entrained concrete. The specimens having various degrees of saturation were subjected to 6 freeze-thaw cycles and tested for the relative dynamic modulus of elasticity. The curves for each of the specimens are shown in Figure 5.5. These curves show the change in the material properties, from which the critical degree of saturation was inferred, i.e., the saturation degree above which there is a reduction in the relative dynamic modulus of elasticity was determined to be the critical degree of saturation.

Table 5.6. Mix designs of specimens tested in a study by Yang *et al*. (2011)

Series	w/c	Cement (kg/m^3)	Water (kg/m^3)	Sand (kg/m^3)	Coarse Aggregate (kg/m^3)	Fly Ash (kg/m^3)	Air Content (Vol. %)
A1	0.54	312	170	739	1,156	45	1.2
A4	0.53	319	170	704	1,101	46	4.1
A6	0.51	332	170	677	1,060	48	5.6
C1	0.36	478	170	669	1,047	69	1.1
C4	0.34	464	160	654	1,023	67	4.3
C6	0.32	497	160	619	969	72	6.5

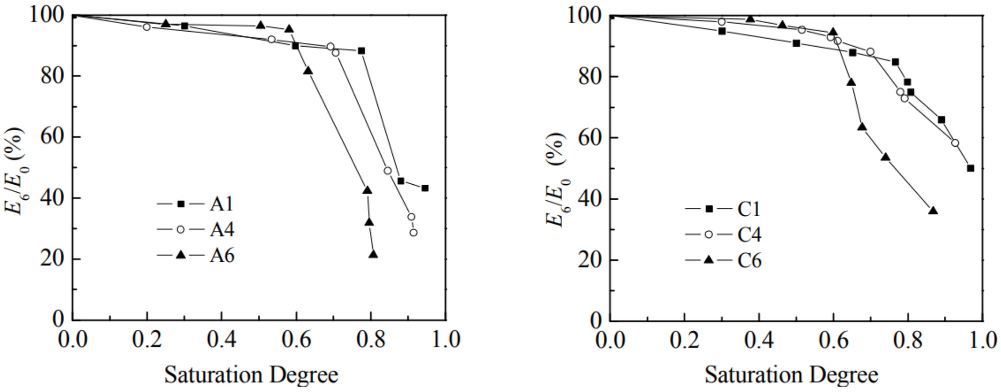

Figure 5.5. The relative dynamic modulus of elasticity of concrete specimens with different saturation degrees (reproduced from Yang *et al.* 2011)

Figure 5.6 was produced from the curves in Figure 5.5, which shows the effect of air content on the critical degree of saturation as it relates to the w/c ratio. It is apparent that air entrainment affects the critical degree of saturation, which in turn affects the dynamic modulus of elasticity.

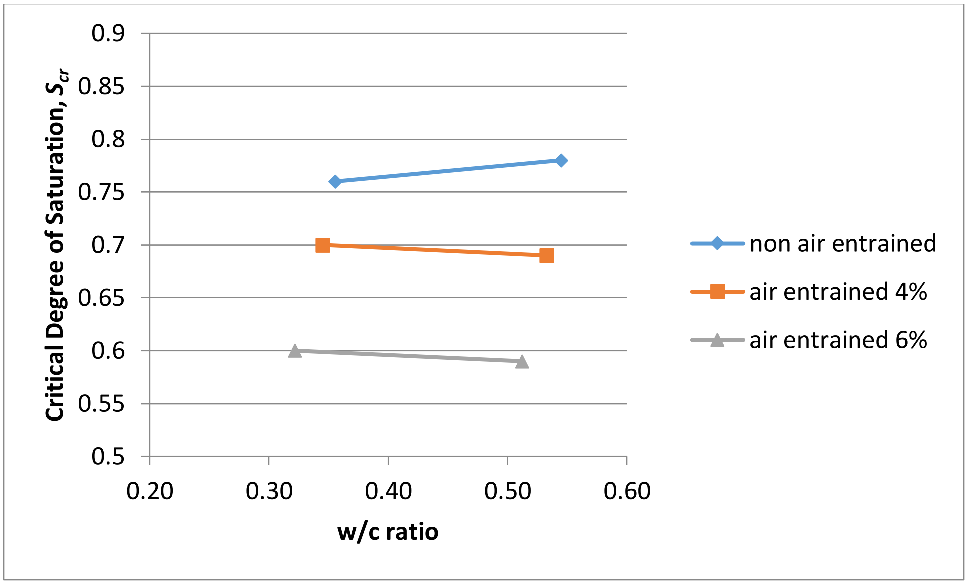

Figure 5.6. The critical degree of saturation as it relates to the w/c ratio and air content

The effect of air content was investigated by varying the critical degree of saturation. From Figure 5.6, the values for the critical degree of saturation are 0.77, 0.69 and 0.59 for concrete with a w/c of 0.4 and air content of 1%, 4% and 6%, respectively. Equation 5.2 was used to quantify the damage and determine the loss in dynamic modulus of elasticity. The degree of saturation, S was set to a value of 1, while the coefficient of fatigue, K_N for 45 freeze-thaw cycles was 1.08. The damaged was applied to the beam as change in material property, E_c. The loss in dynamic modulus of elasticity and the input value of E_c, f_c^d and f_t^d for the analysis are shown in Table 5.7, wherein f_c^d and f_t^d are calculated using Eqs. 3.1 and 3.2, respectively.

Table 5.7. Loss in dynamic modulus of elasticity for different critical degrees of saturation and the corresponding input values of E_c, f_c^d and f_t^d for numerical analysis

S_{cr}	D (%)	E_c (GPa)	f_c^d (MPa)	f_t^d (MPa)
0.59	44.3	18.8	22.4	1.97
0.69	33.5	22.4	24.6	2.17
0.77	24.8	25.3	26.4	2.34

5.4 Results and Discussion

In the presence of water, the external freezing and the subsequent thawing generates pore pressure that can cause significant damage in the solid matrix of concrete. This damage changes the internal structure of concrete as it introduces micro and macro cracks and thereby changes the material properties. The presence of salts on the concrete surface further enhances the damage extent resulting in scaling of the reinforced concrete element. Cycles of freezing and thawing are required for frost damage to occur in concrete; however, porosity and moisture content are parameters that influence the mechanisms of frost damage and dictate when the damage takes place as well as its extent. When the degree of saturation is below the critical value, the effects of repeated freeze-thaw cycles are marginal. However, when the degree of saturation exceeds the critical degree of saturation, the reinforced concrete members cannot sustain a freezing-thawing cycle without accumulating damage.

5.4.1 Number of Freeze-Thaw Cycles

In the parametric study, the effect of repeated freeze-thaw cycles on the load-carrying capacity of reinforced concrete flexural members was investigated. Climate data was retrieved from the Environment Canada database to plot the number of freeze-thaw cycles over a 74-year period for three of Canada's cities, including Calgary, Ottawa and Saint John's. A numerical analysis of a flexural governed beam subjected to damage caused by freeze-thaw cycles after being in service for 10 years, 25 years and 74 years in the three Canadian cities was conducted using the finite element software, VecTor2. This damage was estimated using Eq. 5.2 and was modeled using the method proposed in Chapter 3.

Shown in Figures 5.7-5.9 are the load-deflection responses for the beam at three specified stages of its service life (10, 25 and 74 years) for the three Canadian cities, respectively. The analytical load-deformation response of the undamaged beam is also shown in the figures. In the following discussion, the beams will be denoted by the city and the number of years in service. For example, Calgary10 indicates the beam subjected to 10 years of frost damage in the city of Calgary. From all three figures, it can be observed that with the progression of time and over the course of the beam's service life, there is stiffness degradation and a reduction in the load-carrying capacity of the beam, which reflects the increase in the extent of frost damage. The greatest loss of stiffness and overall flexural strength is experienced in the first 10 years. Between 25 years and 75 years, the magnitude of reduction in the load carrying capacity is relatively low. This is due to the fact that the first cycle causes the most severe damage, and parameter, K_N, as given by Eq. 5.4, stabilizes after 45 cycles. With the accumulation of subsequent freeze-thaw cycles, there is a fatigue limit that is reached, above which it is reasonable to assume that there is no further damage.

From the results of the numerical analysis, it is evident that the damage accumulated over the course of a reinforced concrete beam’s service life due to repeated freeze-thaw cycles has a significant impact on the load-carrying capacity of the member. The saturation degree and critical saturation degree of the beam were specified to be 1 and 0.77, respectively. However, for other values of saturation degree and critical saturation degree, a similar trend but varying magnitude of reduction in the load-carrying capacity is expected given that the degree of saturation is greater than the critical degree of saturation.

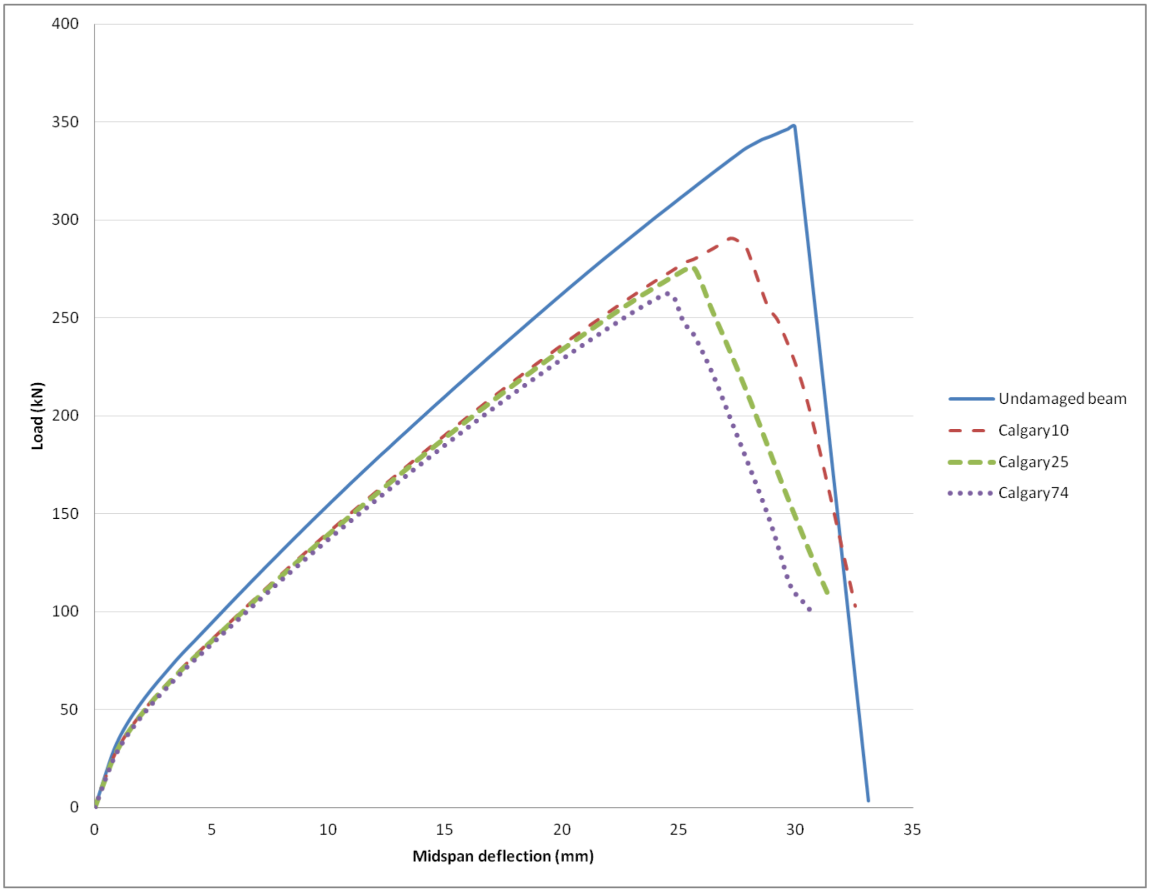

Figure 5.7. Load-deflection response of beam at three stages of its service life in Calgary

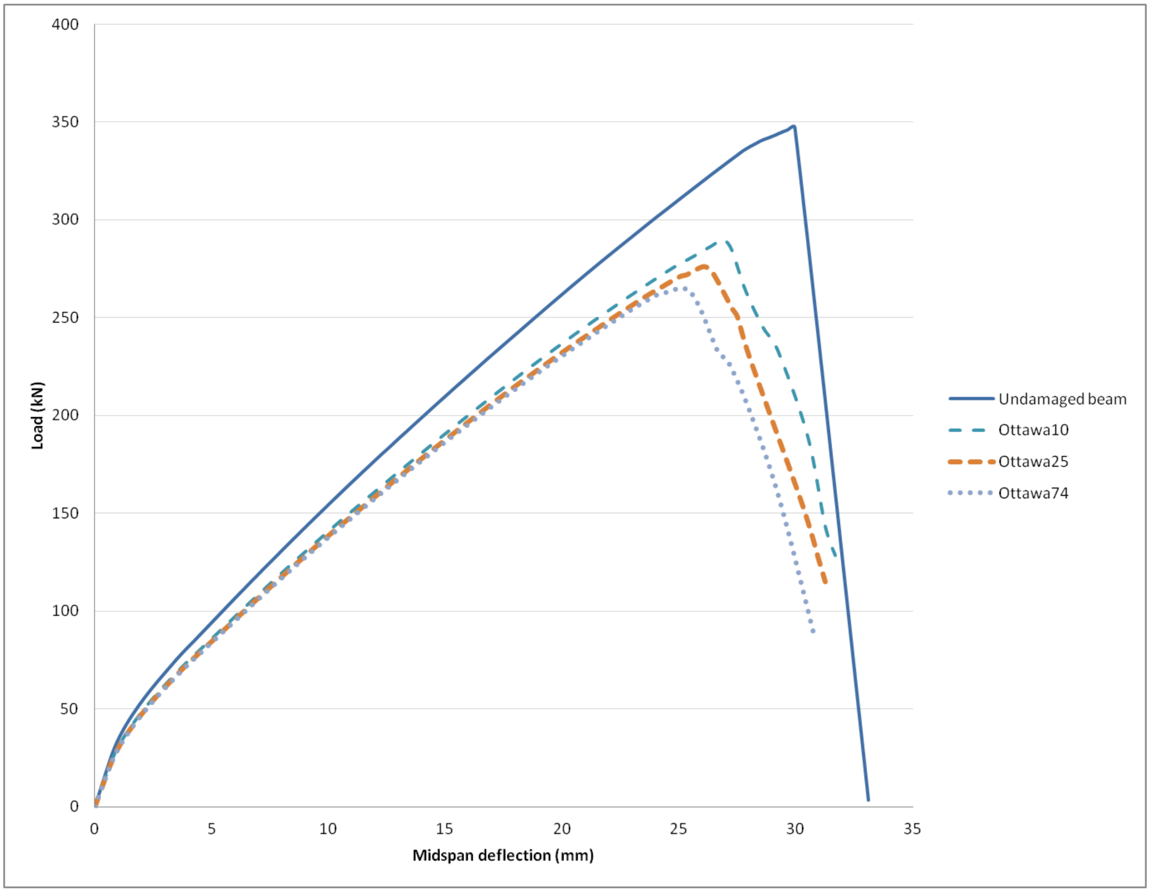

Figure 5.8. Load-deflection response of beam at three stages of its service life in Ottawa

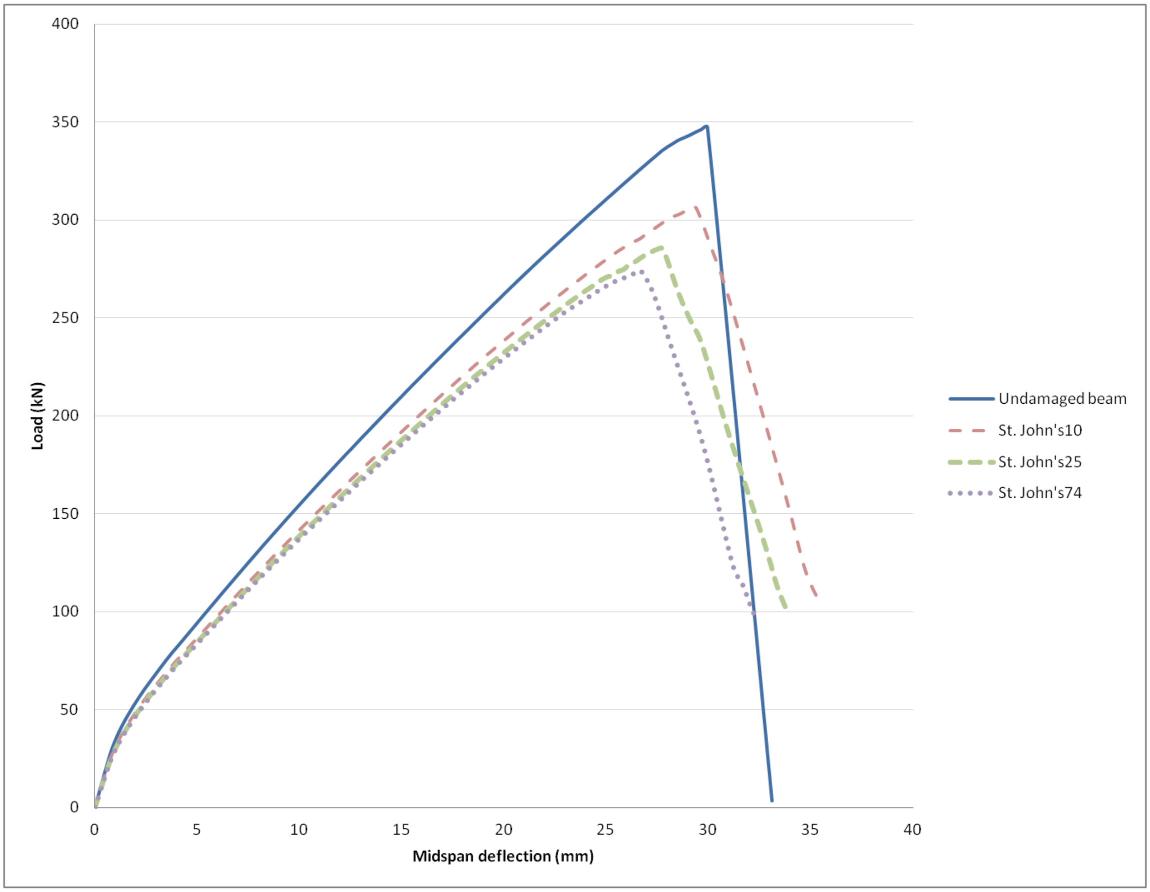

Figure 5.9. Load-deflection response of beam at three stages of its service life in St. John's

The climate in Canada changes from one region to another, and the range of temperature in cities with reinforced concrete infrastructure varies across the country. Reinforced concrete structures therefore experience different number of freeze-thaw cycles depending on which region in the country they are in service. Figures 5.10, 5.11 and 5.12 show the comparison between the load-deflection response of the beam in service in Calgary, Ottawa and St. John's after 10, 25 and 74 years, respectively. Of the three cities, the lesser impacted beam by frost damage is that in service in St. John's. The beams Calgary10 and Ottawa10, and Calgary25 and Ottawa25 show more or less the same extent of damage. However, the beam Calgary74 is the most severely impacted by frost damage in comparison with beams Ottawa74 and St. John's74. These results indicate that it is important when considering the reduction in the load-carrying capacity to consider the climate data of the city that the reinforced concrete structure is serving.

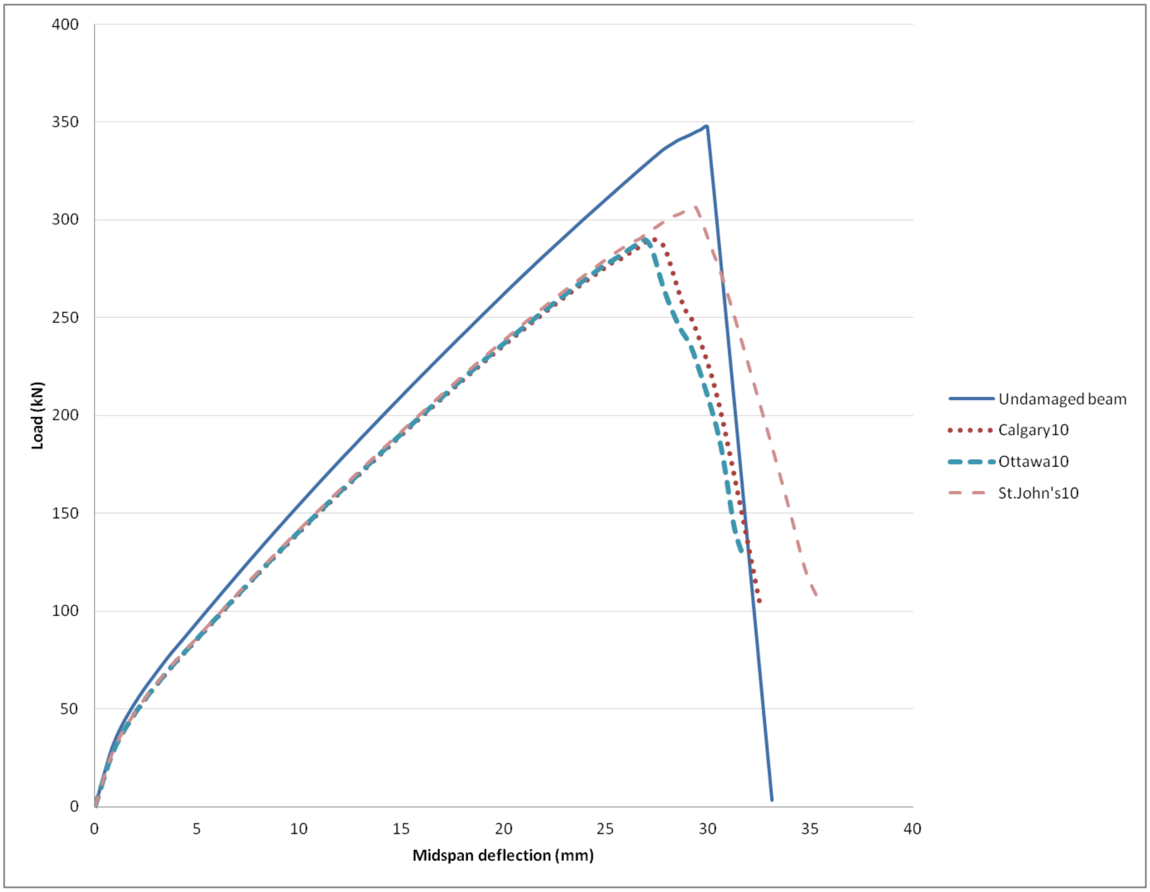

Figure 5.10. Comparison of the load-deflection response of the beam for different cities in Canada after 10 years in service

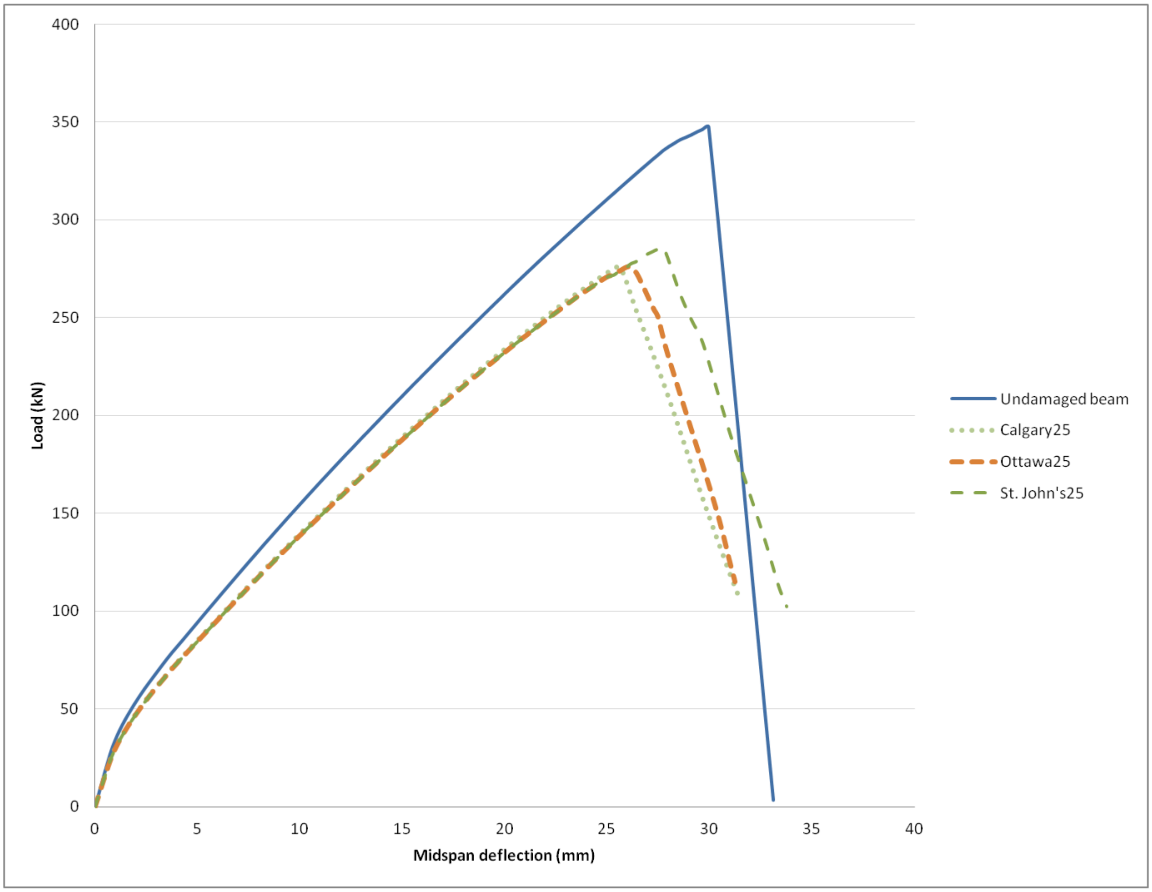

Figure 5.11. Comparison of the load-deflection response of the beam for different cities in Canada after 25 years in service

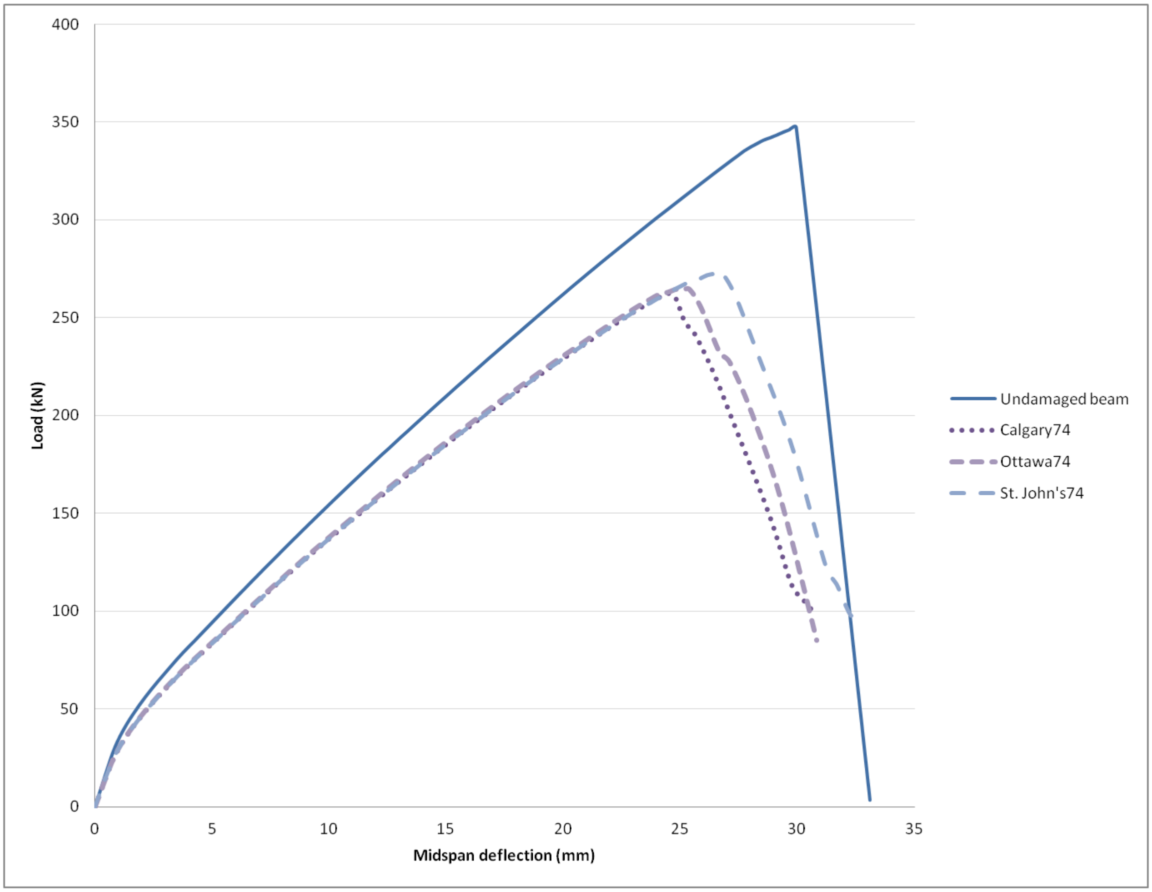

Figure 5.12. Comparison of the load-deflection response of the beam for different cities in Canada after 74 years in service

The variation in the magnitude of reduction in the load-carrying capacity was also investigated and is presented in Table 5.8. Figures 5.13 and 5.14 illustrate the loss in strength and the loss in ductility, respectively. Ductility here and in the subsequent discussions refers to the deformation capacity of the beam up to maximum load. In the first 10 years of their service life, the Calgary and Ottawa beams both suffer approximately 16% loss in strength, the Ottawa beam, however, experiences a slightly greater (0.8%) loss in ductility. After 74 years Calgary suffers a marginally greater loss in strength and ductility than the Ottawa beam. The St. John's beams experience the least amount of strength and ductility loss. However, between 10 and 74 years the greatest magnitude of reduction in strength is seen in the St. John's beam. All beams experience the greatest loss of strength and ductility in the first 10 years. Between 25 years and 75 years, the magnitude of reduction is comparatively less; this trend was discussed previously and is illustrated again in Figures 5.13 and 5.14.

Table 5.8 Loss of load-carrying capacity of beams from progression of frost damage over time

Beam	Peak Load (kN)	Strength Loss (%)	Deflection at Peak Load (mm)	Ductility Loss (%)
Undamaged	347.4		30.0	
Calgary10	290.5	16.4	27.2	9.2
Calgary25	275.7	20.6	25.6	14.5
Calgary74	262.4	24.5	24.5	18.1
Ottawa10	289.7	16.6	26.9	10.0
Ottawa25	276.1	20.5	26.1	12.9
Ottawa74	264.4	23.9	24.8	17.2
St. John's10	305.9	11.9	29.1	2.8
St. John's 25	285.2	17.9	27.8	7.2
St. John's 74	273.6	21.2	26.7	10.7

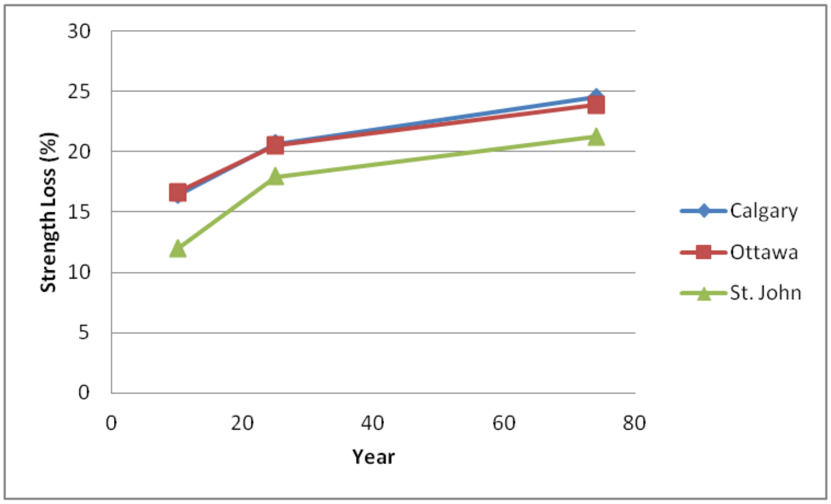

Figure 5.13. Variation in the reduction of strength over time

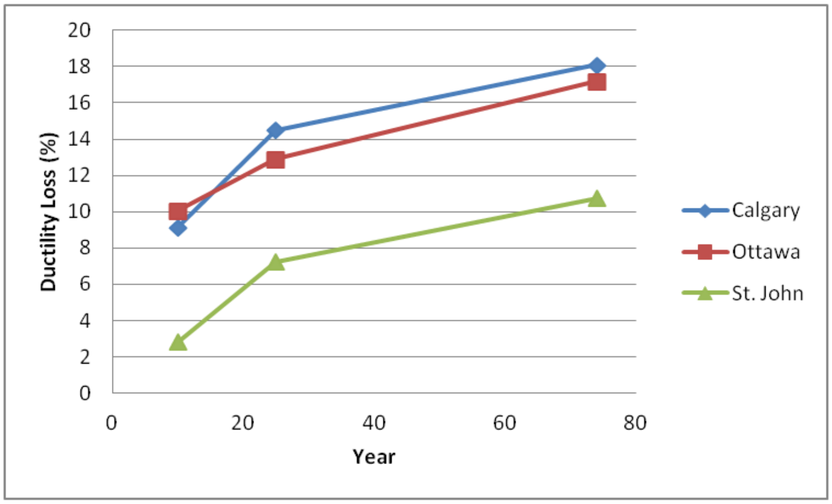

Figure 5.14. Variation in the reduction of ductility over time

The analysis shows that the undamaged beam failed due to yielding of the tensile reinforcement and the simultaneous crushing of concrete in the compression zone; see Figures 5.19 and 5.23. All frost damaged beams failed in a brittle manner from concrete crushing in the compression zone before the steel had yielded; see Figures 5.20-5.22 and 5.24-5.26. Frost damage led to a change in the failure mode, which can be understood by observing the crack patterns as shown in Figures 5.15-5.18. The crack distribution from the analysis of the undamaged beam showed that relatively few and small bending flexural cracks formed before the yielding of the tensile reinforcement (Figure 5.15), which governed the failure of the beam. For the frost-damaged beams, the numerical analysis showed the propagation of flexural cracks followed by the initiation of diagonal shear cracks before crushing of concrete in compression. The progression and extent of cracking is greater in beams with 10 years of damage than in beams with 25 or 74 years of damage; see Figures 5.16-5.18. This is expected because at 10 years, the beam has the greater load-carrying capacity. The cracking patterns reflect the beam's capacity to sustain greater loads which allows for greater extent of crack propagation.

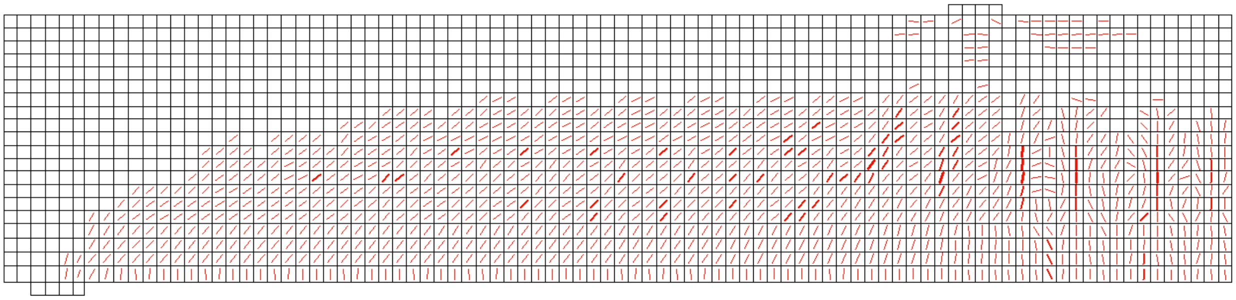

Figure 5.15. Crack pattern of the undamaged beam

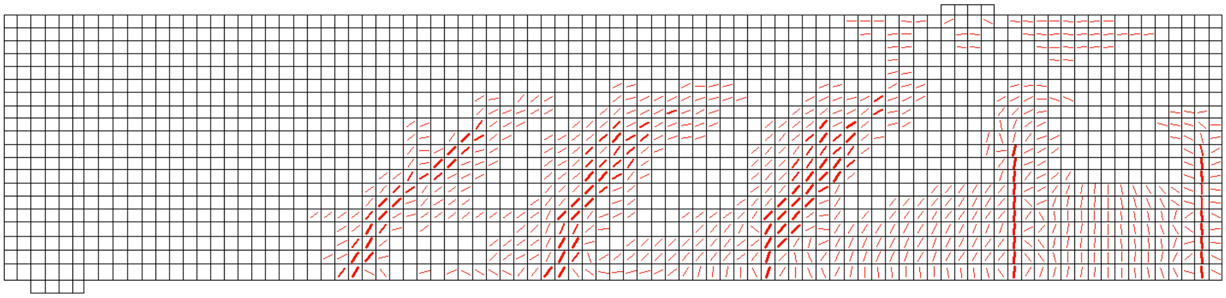

(a)

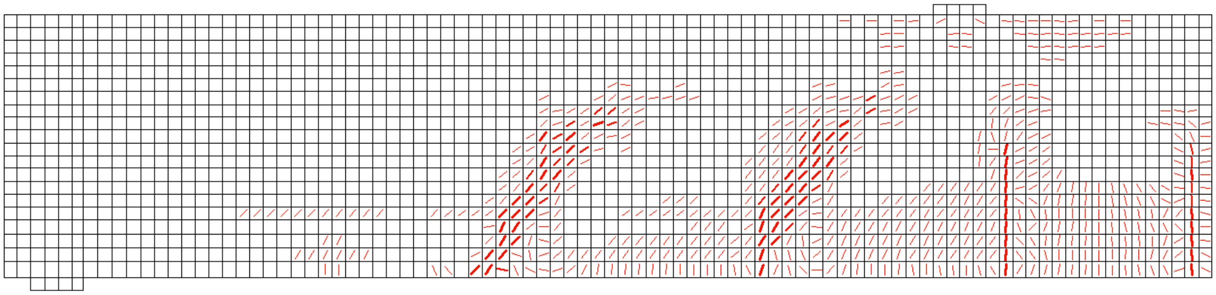

(b)

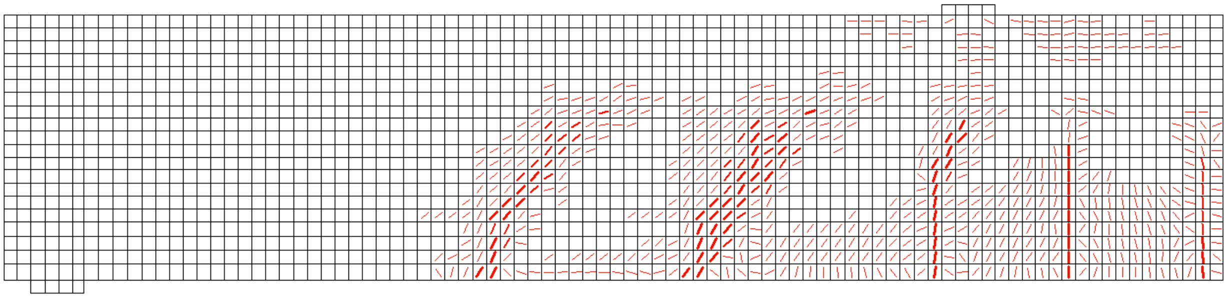

(c)

Figure 5.16. Crack pattern of beams (a) Calgary10, (b) Calgary25, and (c) Calgary74

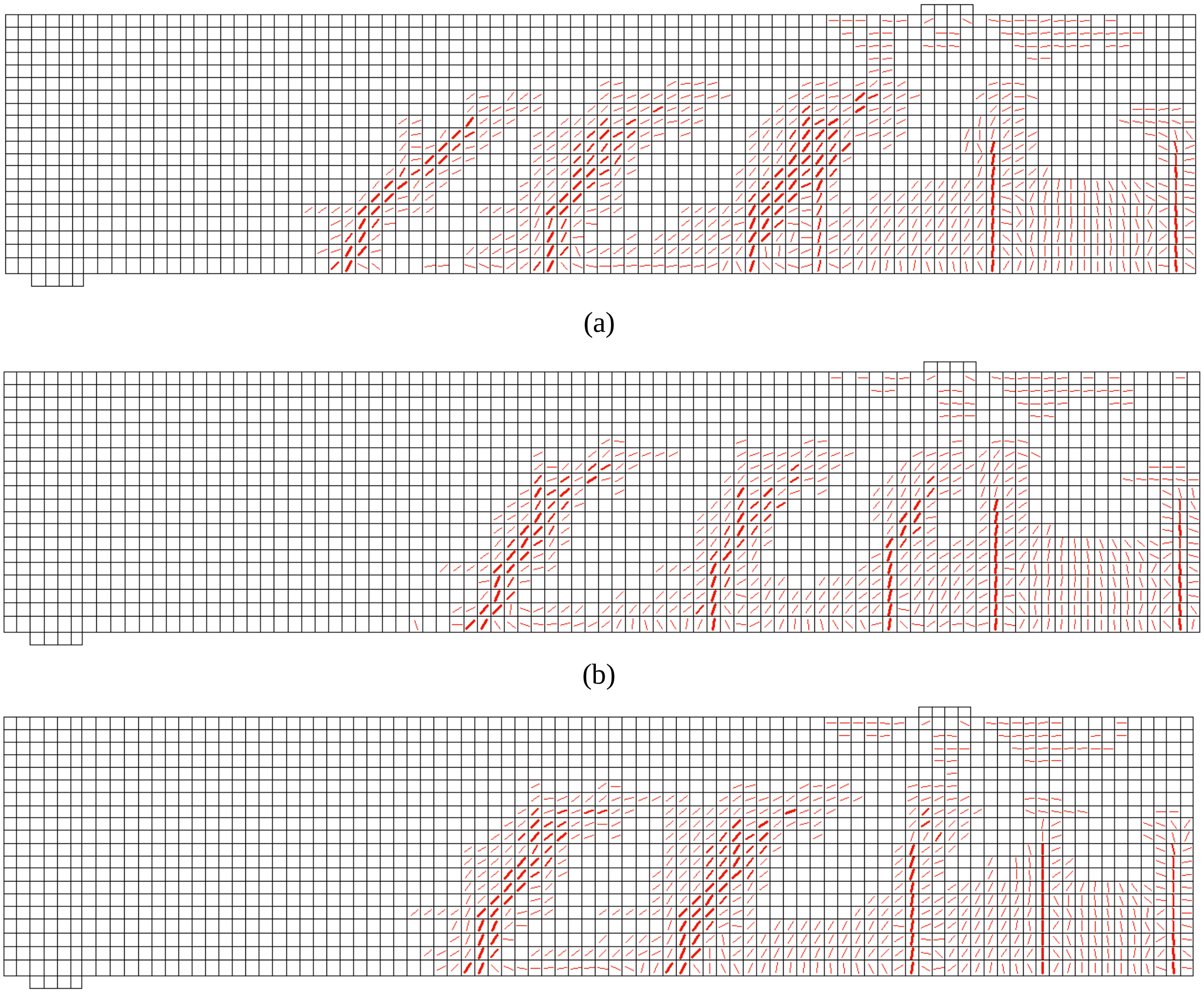

(a)

(b)

(c)

Figure 5.17. Crack pattern of beams (a) Ottawa10, (b) Ottawa25, (c) and Ottawa74

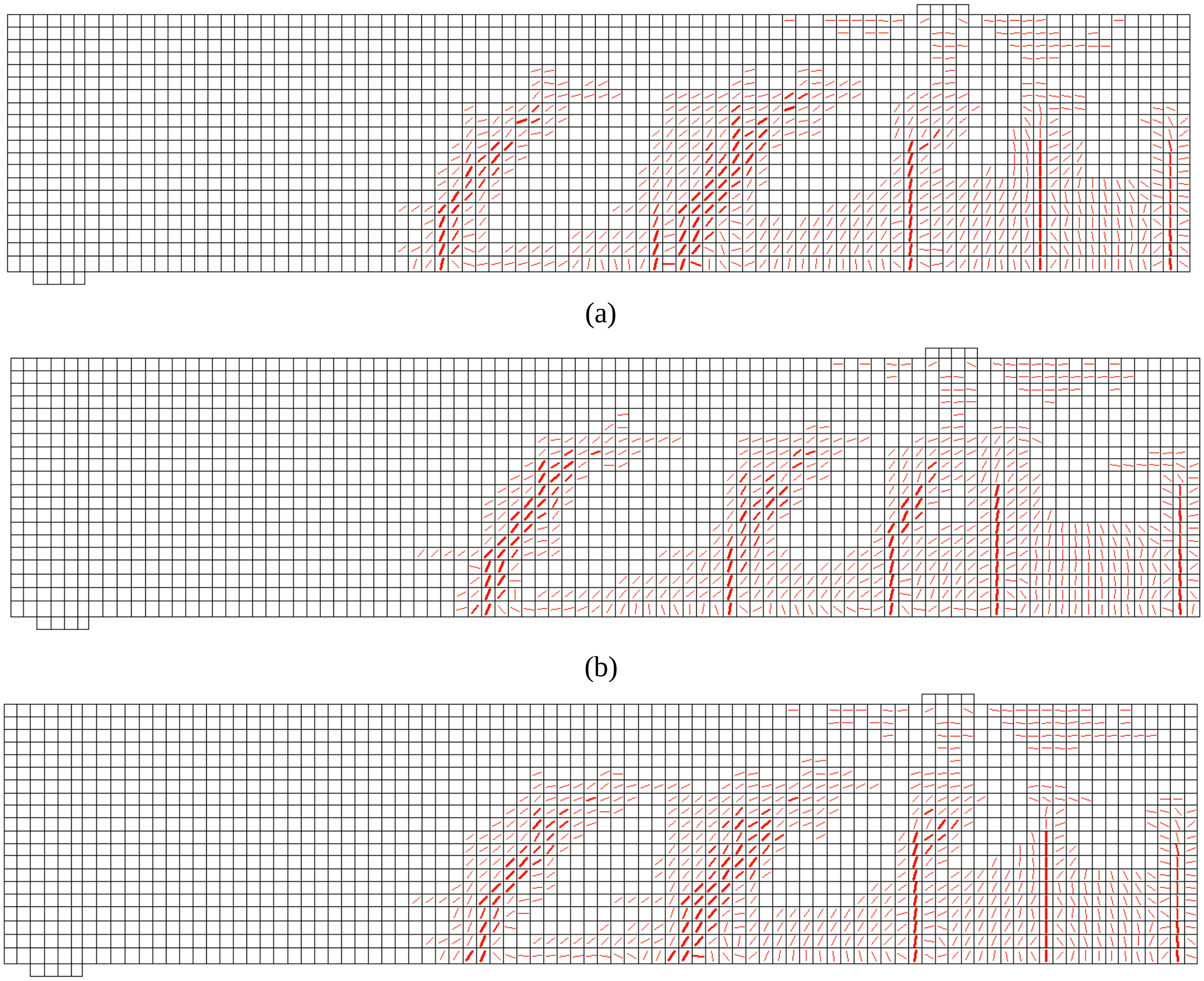

(a)

(b)

(c)

Figure 5.18. Crack pattern of beams (a) St. John’s10, (b) St. John’s25, and (c) St. John’s74

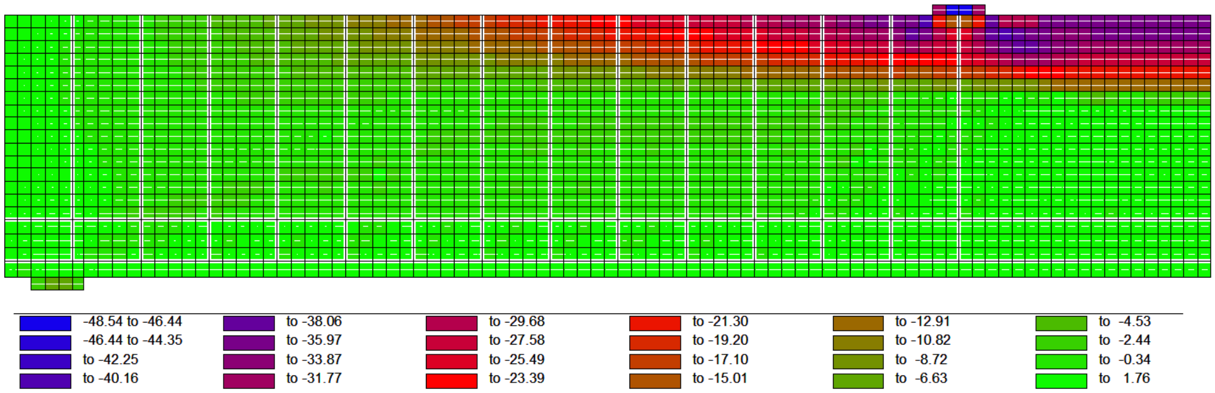

Figure 5.19. Axial stress distribution in the concrete of the undamaged beam (units in MPa)

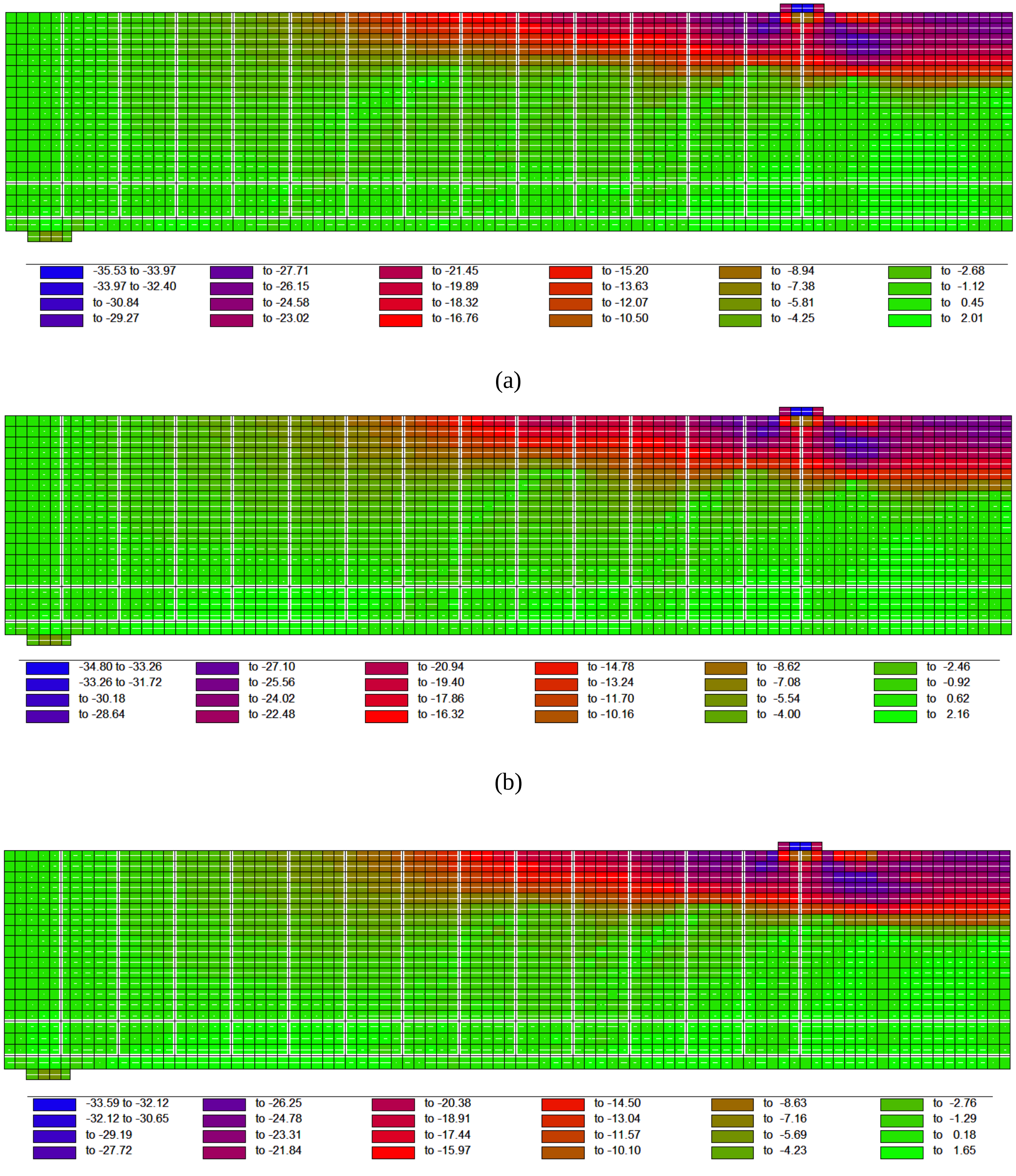

(a)

(b)

(c)

Figure 5.20. Axial stress distribution in the concrete of beams (a) Calgary10, (b) Calgary25, and (c) Calgary74 (units in MPa)

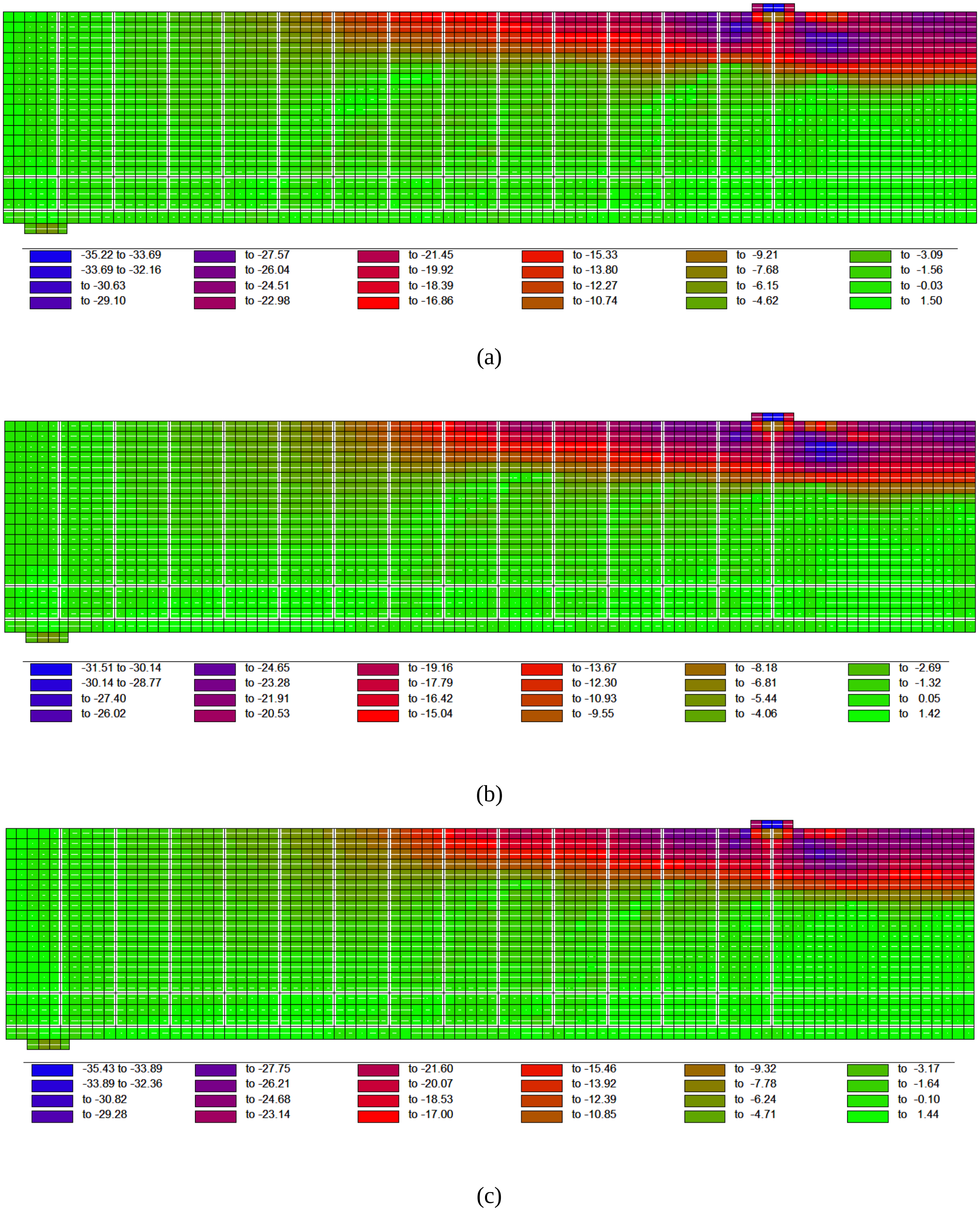

Figure 5.21. Axial stress distribution in the concrete of beams (a) Ottawa10, (b) Ottawa25, (c) and Ottawa74 (units in MPa)

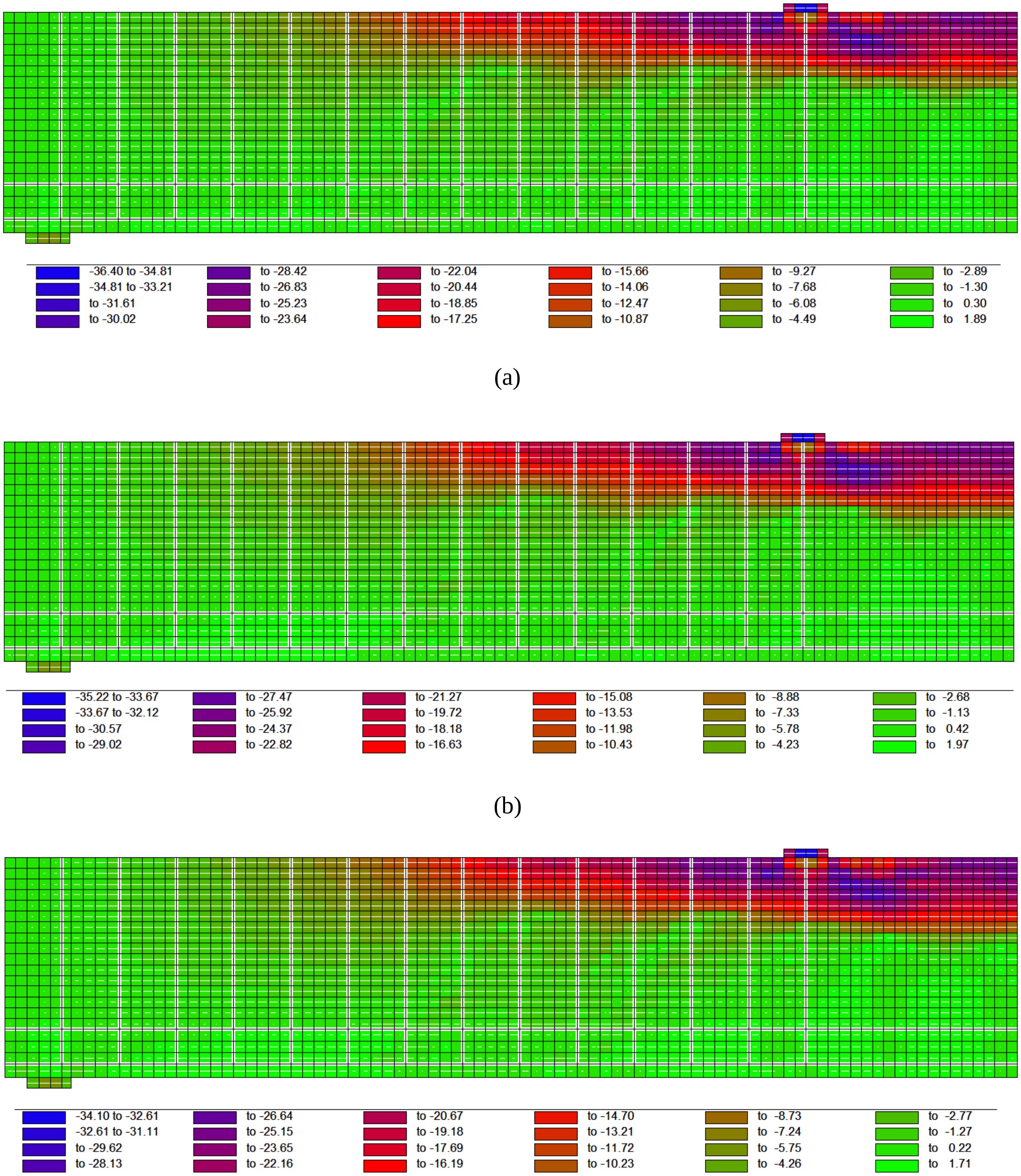

(a)

(b)

(c)

Figure 5.22. Axial stress distribution in the concrete of beams (a) St. John's10, (b) St. John's25, and (c) St. John's74 (units in MPa)

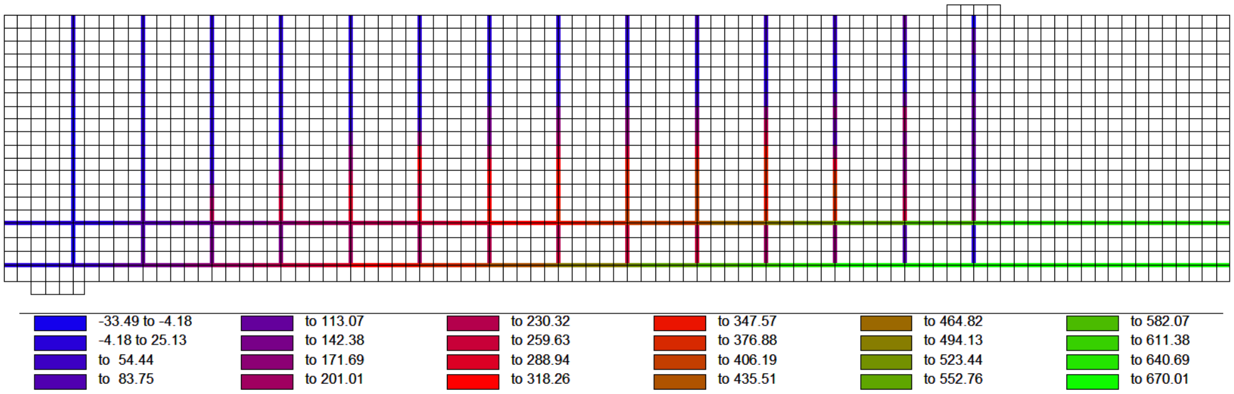

Figure 5.23. Axial stress distribution in the steel reinforcement of the undamaged beam (units in MPa)

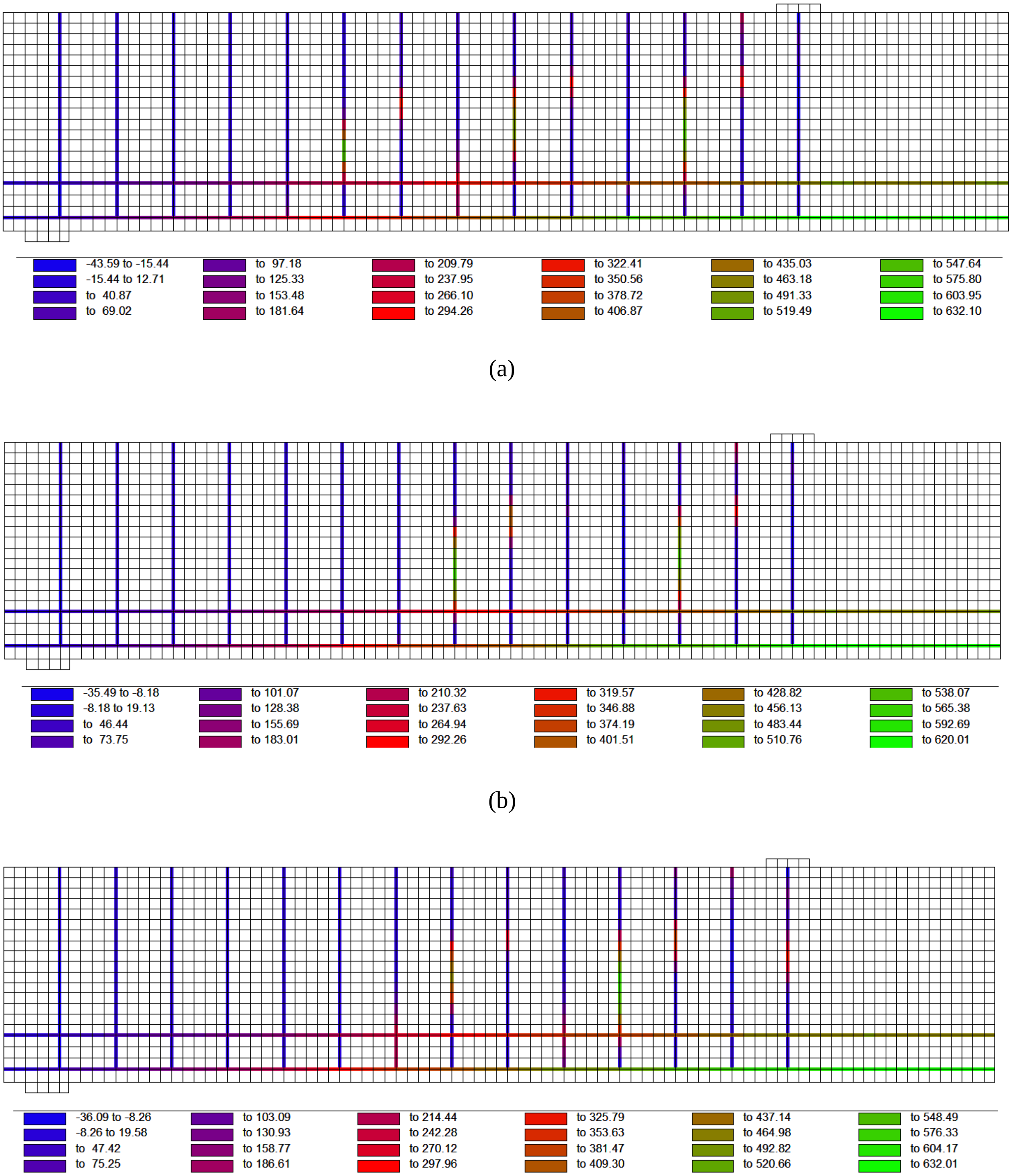

(a)

(b)

(c)

Figure 5.24. Axial stress distribution in the steel reinforcement of beams (a) Calgary10, (b) Calgary25, and (c) Calgary74 (units in MPa)

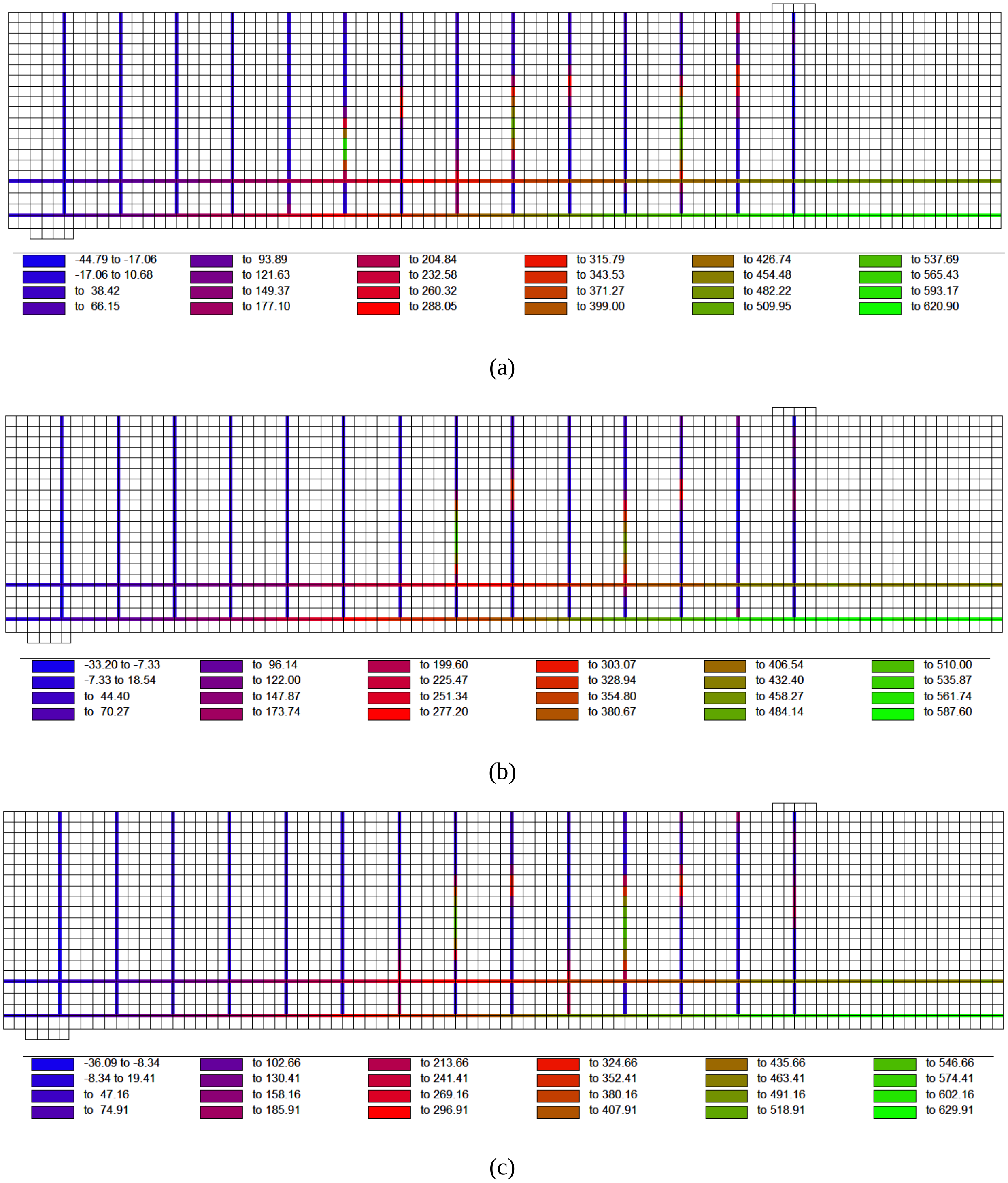

Figure 5.25. Axial stress distribution in the steel reinforcement of beams (a) Ottawa10, (b) Ottawa25, (c) and Ottawa74 (units in MPa)

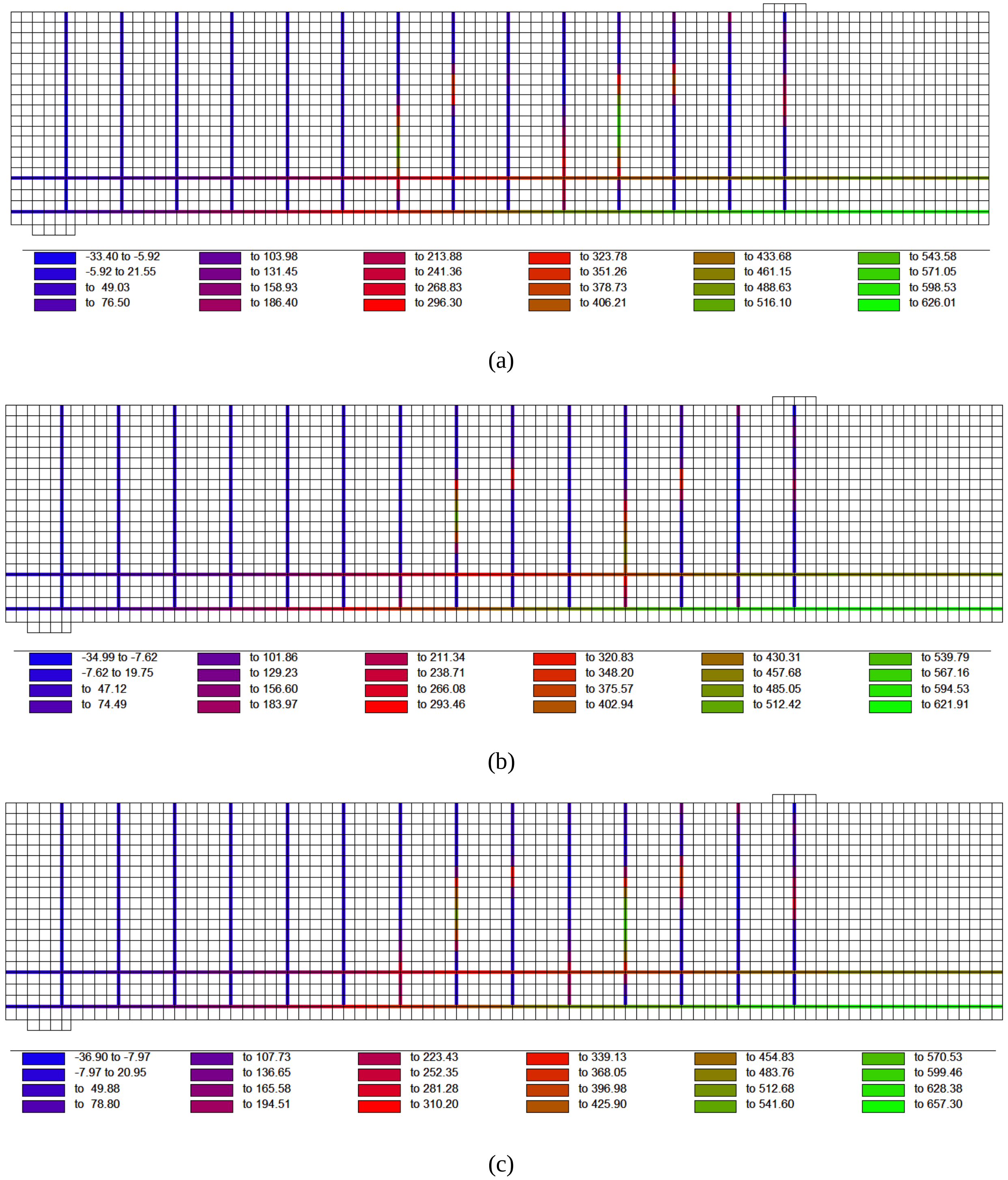

Figure 5.26. Axial stress distribution in the steel reinforcement of beams (a) St. John's10, (b) St. John's25, and (c) St. John's74 (units in MPa)

In designing the beam, it is of paramount importance to consider this loss of load and deflection capacity as it will have an effect on the mode of failure. However, the current design code, CSA A23.3 does not provide measures to quantify and mitigate accordingly this loss in capacity that results from successive freeze-thaw cycles over the service life of the reinforced concrete member. The standard does, however, refer to the CSA A23.1, which specifies a maximum water-to-cement ratio, a minimum specified compressive strength at 28 days, and a minimum amount of entrained air depending on the exposure category.

5.4.2 Moisture Content

When concrete is saturated, it becomes susceptible to frost damage. To observe the effects of the moisture content on the load-carrying capacity of reinforced concrete, beams with three different degrees of saturation were modeled. The load-deflection response of the beams with varying degrees of saturation and S_{cr} = 0.77 subjected to freeze-thaw cycles is shown in Figure 5.27. The initial stiffness does not change with the degree of saturation; however, the load-deflection response of the beam deteriorates as the moisture content is increased. When the beam is fully saturated, it shows a 22% reduction in the strength and a 15% loss of ductility; see Table 5.9 and Figures 5.28 and 5.29. The magnitude of the loss in the overall load-carrying capacity of the beam when the saturation degree is increased from 0.8 to 0.9 is less than when the degree of saturation is increased from 0.9 to 1.

The axial stress distribution from analysis showed that the three damaged beams with varying saturation degrees all experienced brittle failure (Figures 5.31 and 5.32); the deterioration of concrete led to failure in compression before the reinforcement had yielded. The varying degree of damage applied to the beams is reflected in the axial stress distribution. Figure 5.30 shows the crack distribution at failure in the beams. The development of vertical flexural cracks followed by inclined flexural-shear cracks can be observed. The initiation and subsequent propagation of the cracks is indicative of deterioration, because the undamaged beam, as seen in Figures 5.15, 5.19 and 5.23, failed from yielding of reinforcement prior to development of diagonal cracks.

The trends observed in the analytical results are in agreement with the understanding that the effect of frost damage on the structural response of reinforced concrete members is intensified when the degree of saturation is increased. The Canadian design code stipulation for providing resistance to frost damage is to specify air entrainment in the concrete mix design. However, if concrete is fully saturated, repeated freezing and thawing will cause significant amount of damage, regardless of the quantity of the air. It is, therefore, imperative that reinforced concrete members subjected to freeze-thaw cycles are protected from moisture. Current preventative measures to protect the concrete against water uptake and permeation include the use of water-resisting admixtures for the concrete.

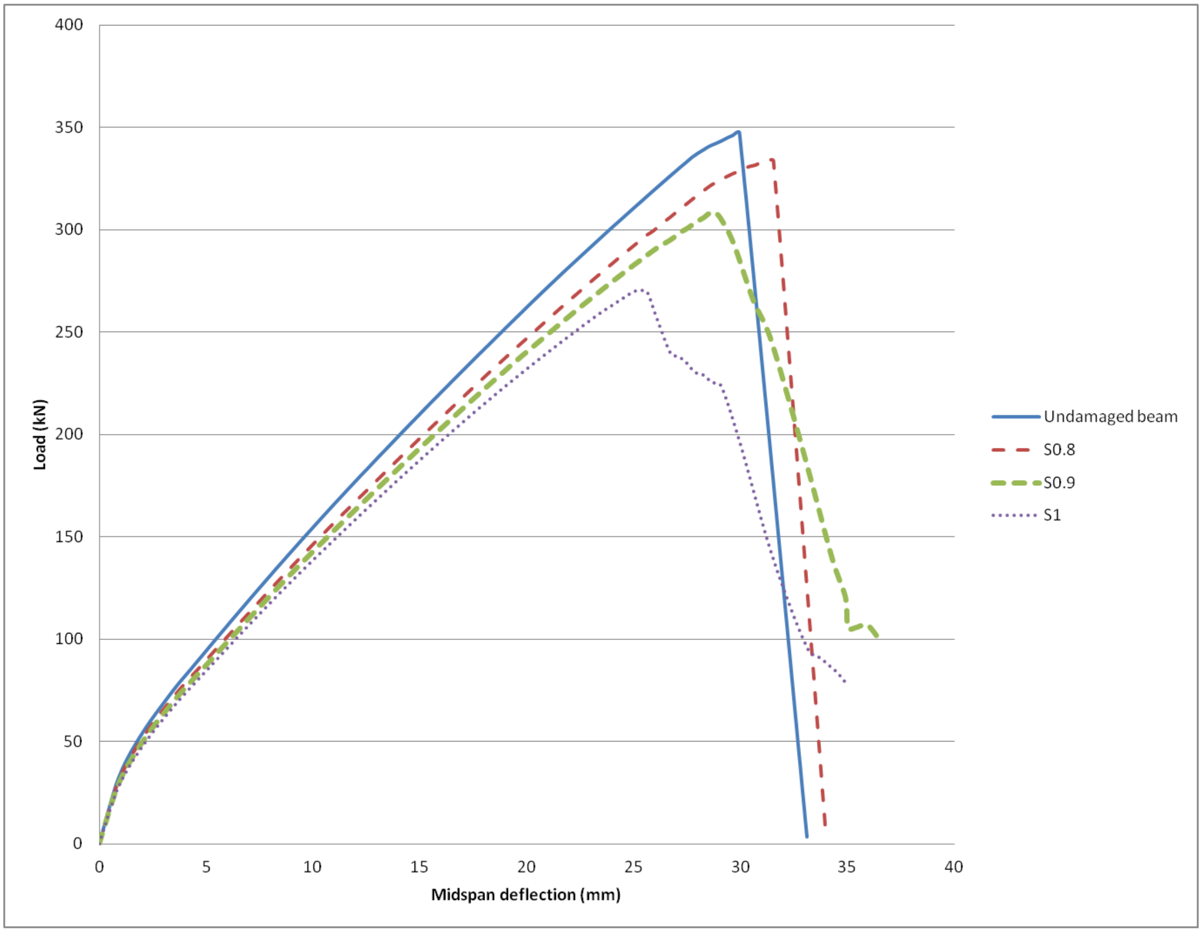

Figure 5.27. The load-deflection response of the beam with different degrees of saturation

Table 5.9. Loss of load-carrying capacity of beams with varying degrees of saturation

Beam	Peak Load (kN)	Strength Loss (%)	Deflection at Peak Load (mm)	Ductility Loss (%)
Undamaged	347.4		30.0	
S0.8	333.9	3.9	31.3	0
S0.9	308.5	11.2	28.8	3.8
S1	270.6	22.1	25.3	15.4

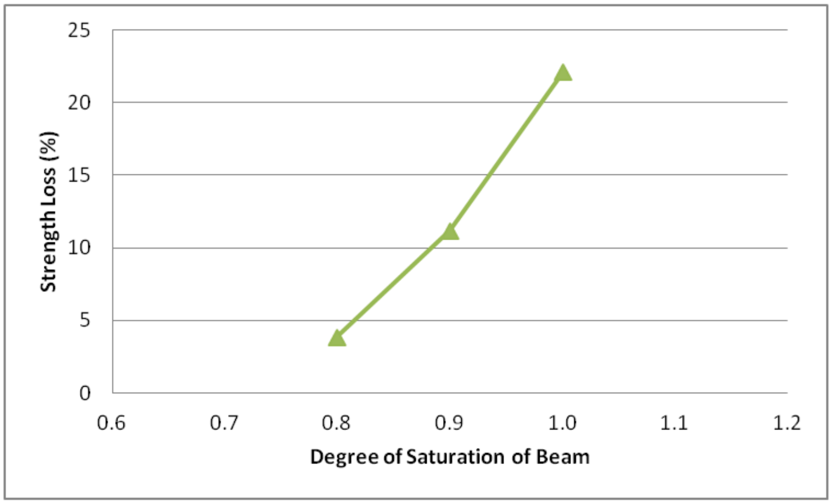

Figure 5.28. Loss of strength for varying degrees of saturation

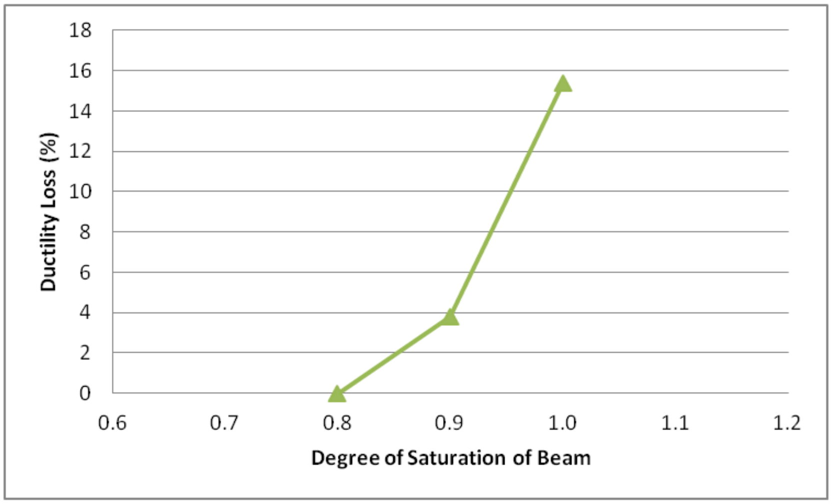

Figure 5.29. Loss of ductility for varying degrees of saturation

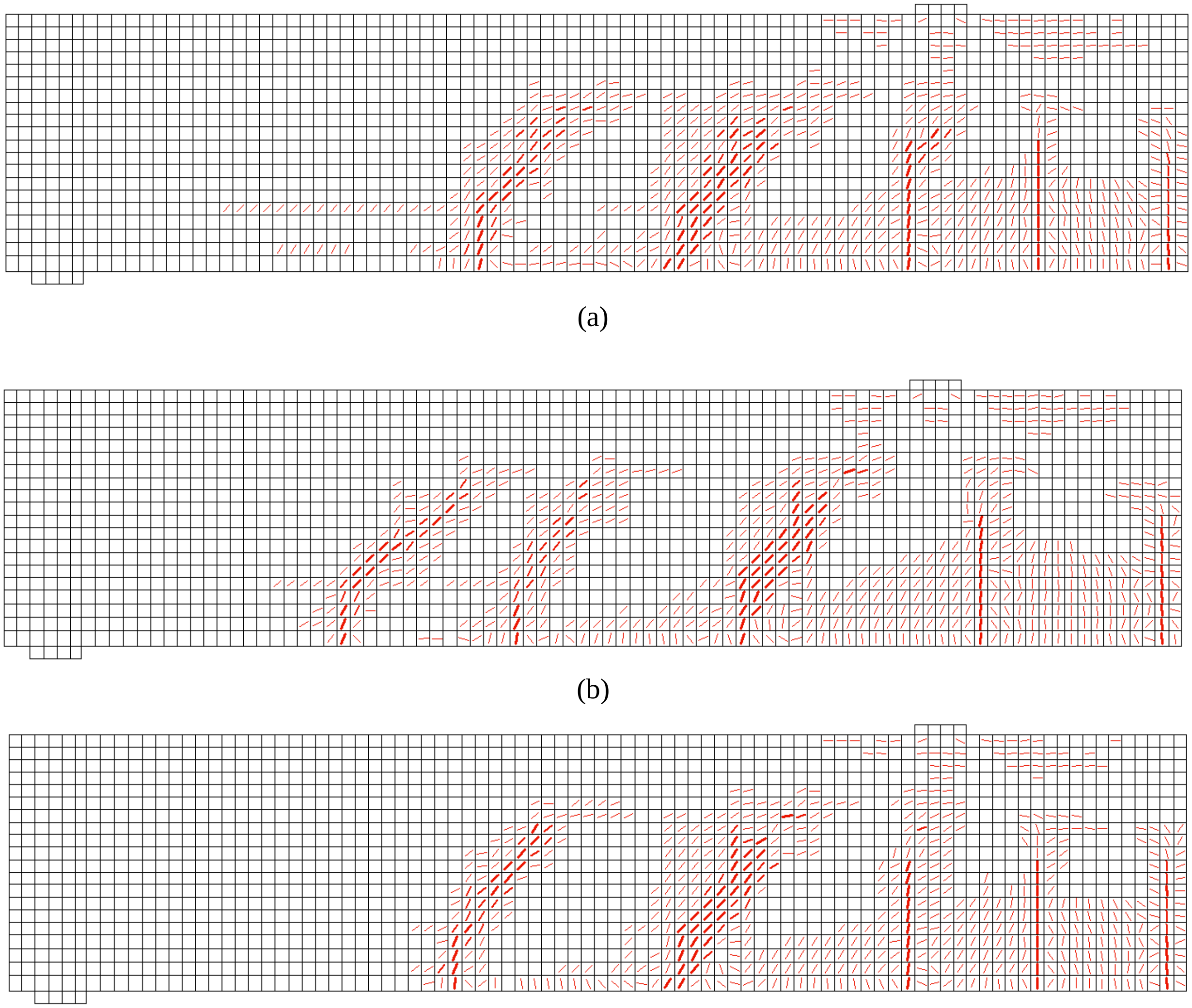

(a)

(b)

(c)

Figure 5.30. Crack pattern of beams (a) S0.8, (b) S0.9, and (c) S1

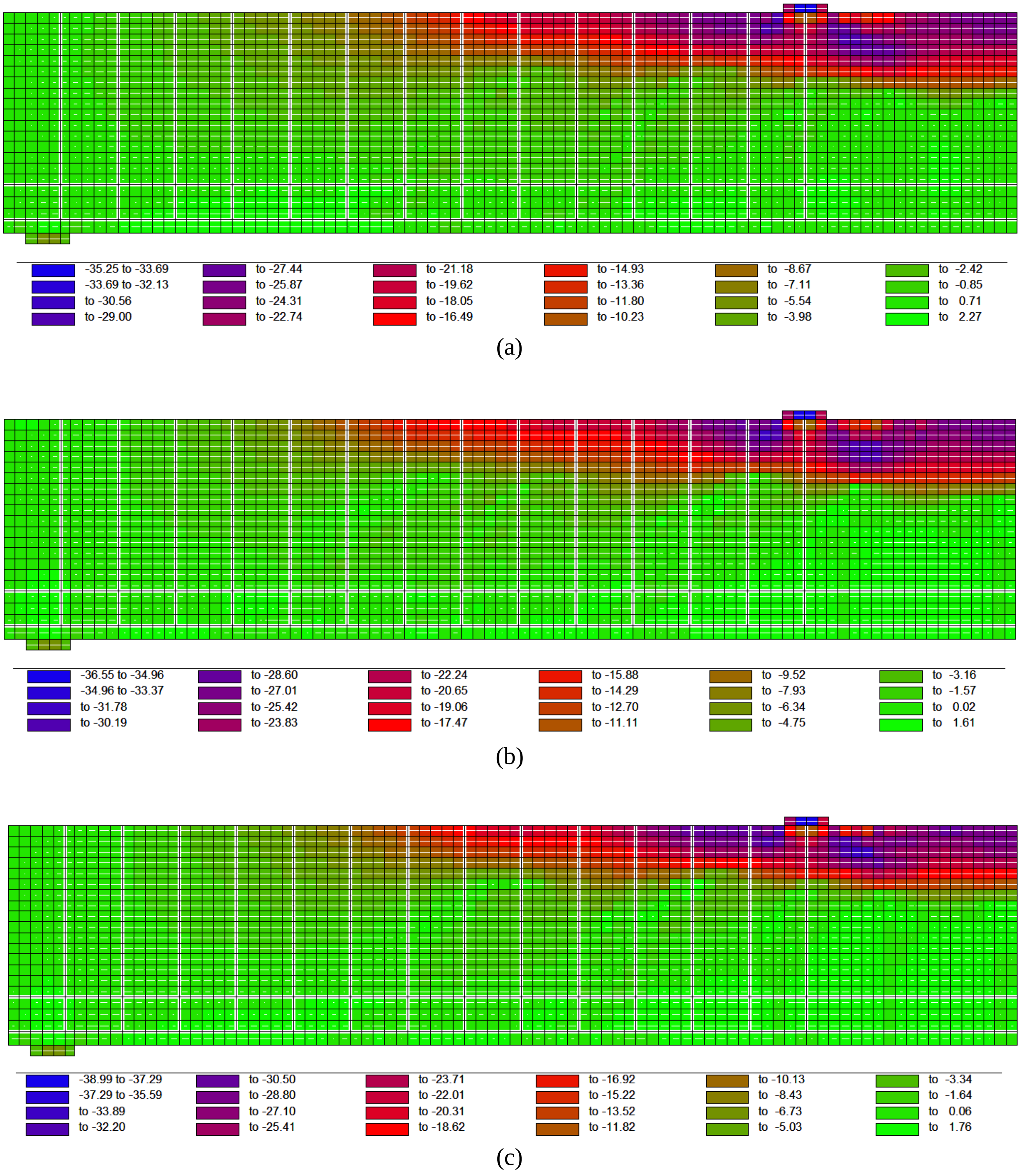

Figure 5.31. Axial stress distribution in the concrete of beams (a) S0.8, (b) S0.9, and (c) S1 (units in MPa)

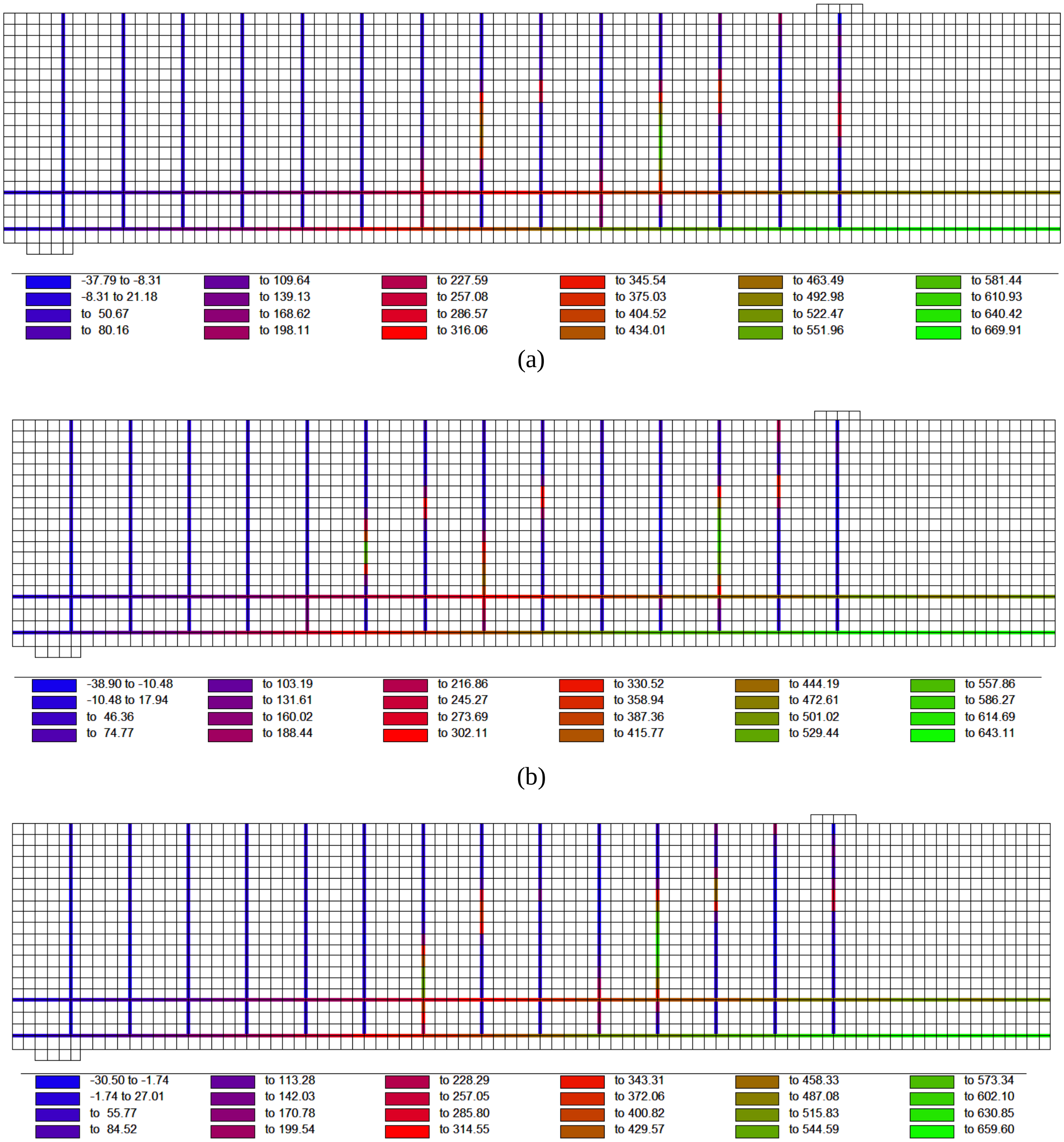

(a)

(b)

(c)

Figure 5.32. Axial stress distribution in the steel reinforcement of beams (a) S0.8, (b) S0.9, and (c) S1 (units in MPa)

5.4.3 Air Content

The volume of entrained air in concrete is an important parameter that affects the freeze-thaw resistance of concrete and is related to the critical degree of saturation. As part of the parametric study, effects of varying the volume of entrained air on the freeze-thaw resistance of concrete was examined through varying the critical degree of saturation, S_{cr} (when S=1). Studies have shown that S_{cr} decreases with increasing air content (Yang *et al*. 2011). Thus, effects of increasing air content and subsequently lowering S_{cr} on the extent of frost damage was modeled using the methods proposed in Chapter 3. The results of the numerical analysis are presented as the load-deflection response of the beam in Figure 5.33. It is evident that concrete with lower S_{cr} has less capacity to sustain loading. Table 5.10 presents the magnitude of reduction in the load-carrying capacity of beams with critical degrees of saturation increased from 0.59 to 0.69 and then to 0.77. These results are illustrated in Figures 5.34 and 5.35. From these figures, it is observed that both the loss in strength and the loss in ductility follow a linear trend. Beams subjected to freeze-thaw cycles that have a critical saturation degree of 0.59, 0.69, and 0.77 experience strength reduction of 39.5%, 30.4% and 21.2%, respectively. The loss in ductility is slightly less compared to the loss of strength (31.3%, 23%, and 12.9% in beams with critical saturation degrees of 0.59, 3.69 and 0.77, respectively). The cracking pattern of the beams from the analysis can be observed in Figure 5.36. Vertical flexural cracks and inclined flexural-shear cracks are observed in each beam. The axial stress distribution in the concrete and steel reinforcement, presented in Figures 5.37 and 5.38, shows that the load-carrying capacity of the beams was limited by the crushing of the concrete in the compression zone. It is important to note that the above results assume that the concrete is fully saturated, i.e., S = 1. The degree of frost damage is a function of the difference between the actual saturation level of the concrete and its critical degree of saturation.

The quantity of the air voids in concrete is related to the critical degree of saturation. The results of the analysis show that for concrete with higher air content there is greater stiffness degradation and reduction in the load-carrying capacity of reinforced concrete flexural members. However, another important parameter that affects the freeze-thaw resistance of concrete, which was not taken into account in the analysis, is the quality of air distribution. The quality of the air distribution is related to the critical flow distance, which is defined as the maximum distance that water can flow from freezing site to the closest air-filled pore. As discussed previously, frost damage does not occur unless the degree of saturation is greater than the critical degree of saturation. Additionally, if the flow distance is below the critical distance and the degree of saturation is less than the critical degree of saturation, frost damage does not occur. If either the flow distance or degree of saturation is above their respective critical values, then concrete will experience frost damage upon being subjected to freeze-thaw cycles. The quality of air distribution and the volume of the air are two important parameters affecting the freeze-thaw resistance of the system. As mentioned before, air entrainment, as stipulated by code provisions, is the most effective method in protecting reinforced concrete members against frost damage. However, the quality of air distribution needs to be also considered in the context of frost-damage resistance.

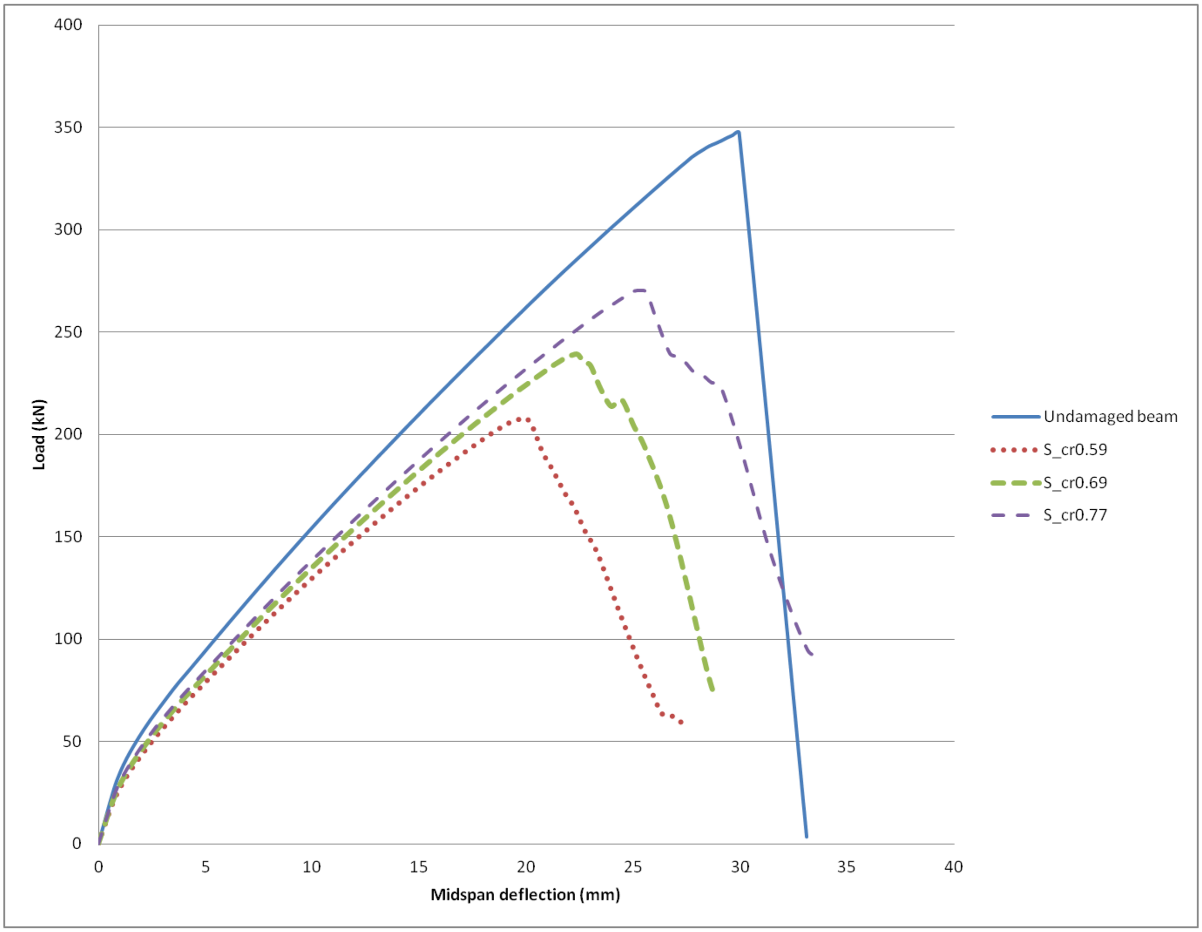

Figure 5.33. The load-deflection response of beam with varying degrees of saturation

Table 5.10. Loss of load-carrying capacity of beams with varying values of critical saturation degrees

Beam	Peak Load (kN)	Strength Loss (%)	Deflection at Peak Load (mm)	Ductility Loss (%)
Undamaged	343.4		29.1	
S_cr0.59	207.7	39.5	20.0	31.3
S_cr0.69	239.0	30.4	22.4	23.0
S_cr0.77	270.6	21.2	25.3	12.9

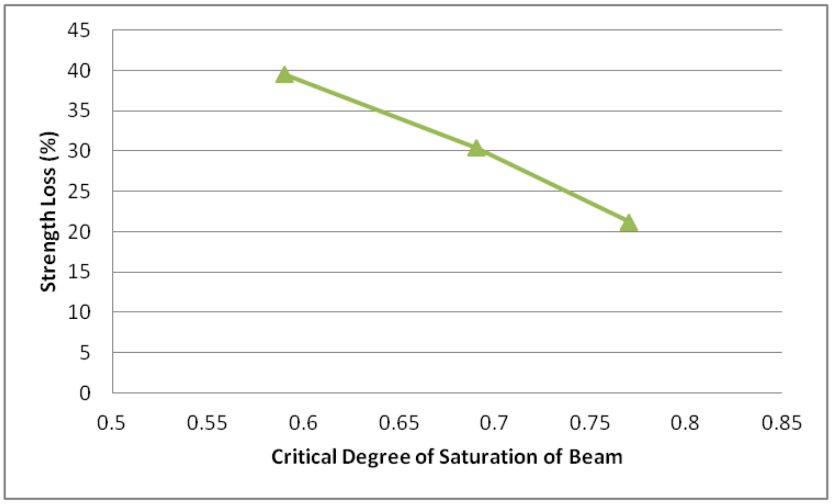

Figure 5.34. Loss of strength for varying critical saturation degrees

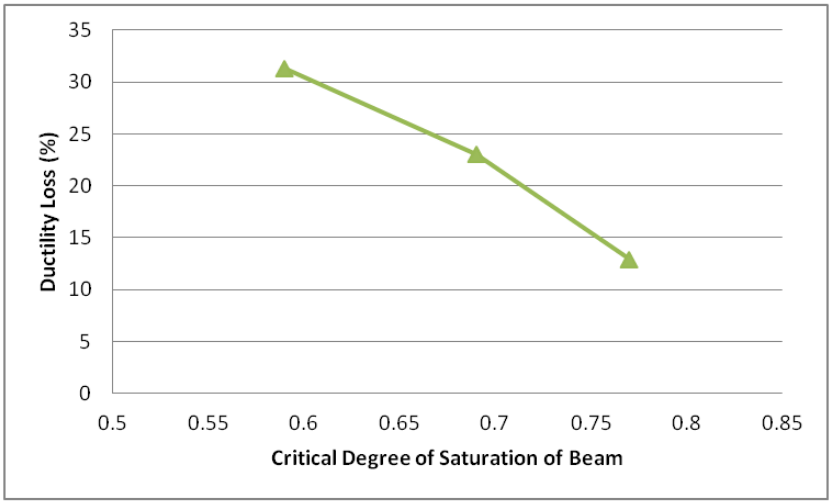

Figure 5.35. Loss of ductility for varying critical saturation degrees

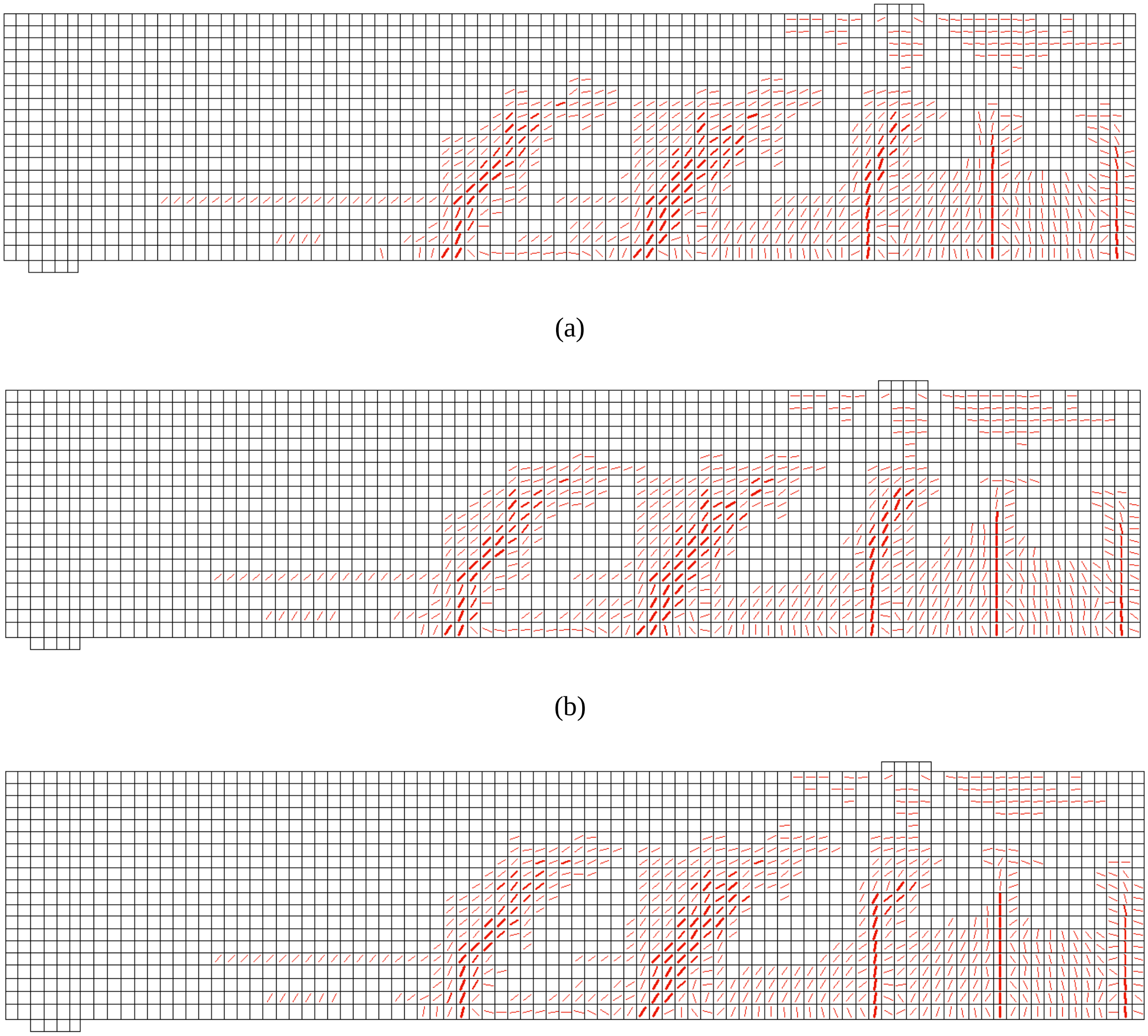

(a)

(b)

(c)

Figure 5.36. Crack pattern of beams (a) S_cr0.59, (b) S_cr0.69, and (c) S_cr0.77

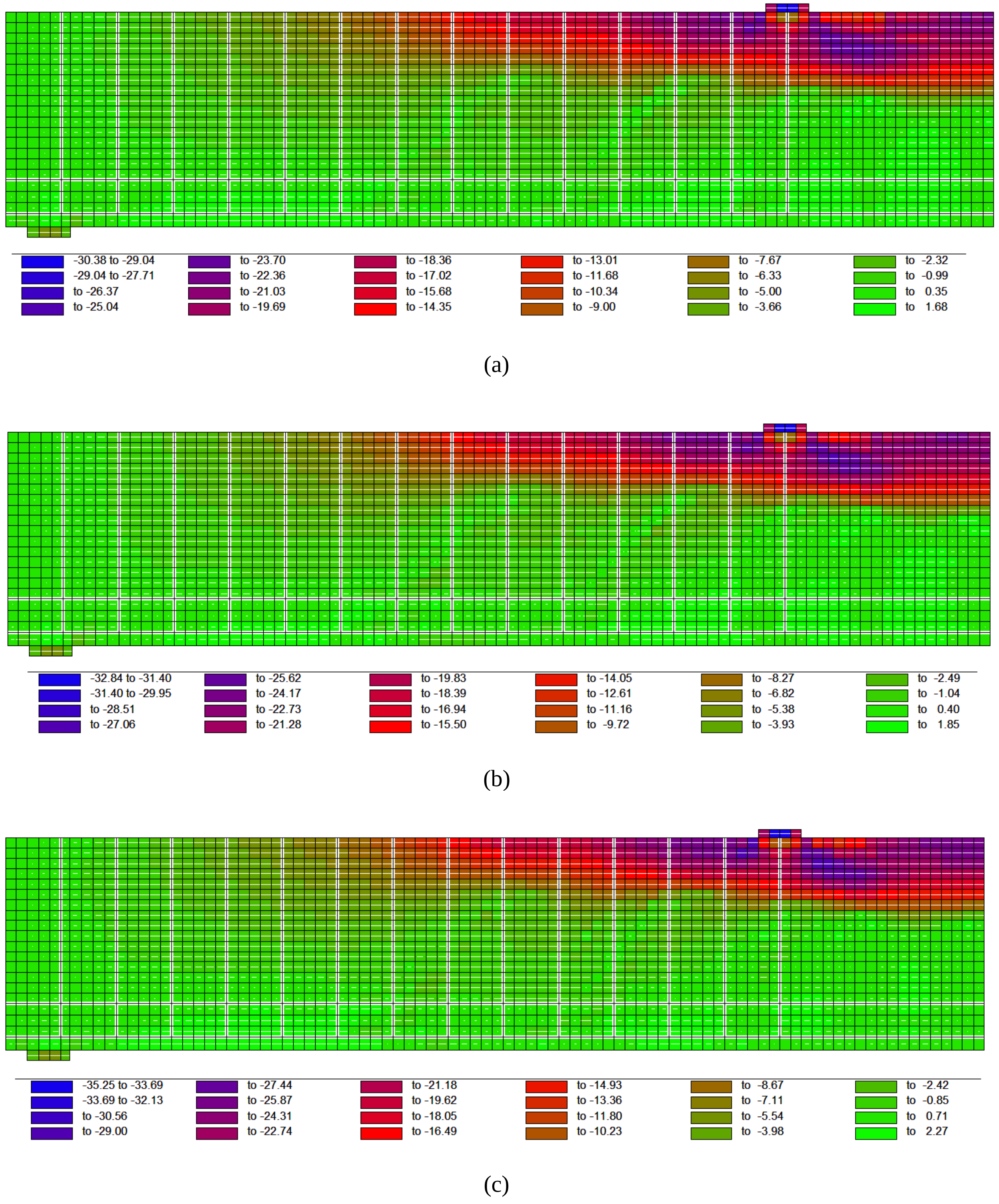

Figure 5.37. Axial stress distribution in the concrete of beams (a) S_cr0.59, (b) S_cr0.69, and (c) S_cr0.77 (units in MPa)

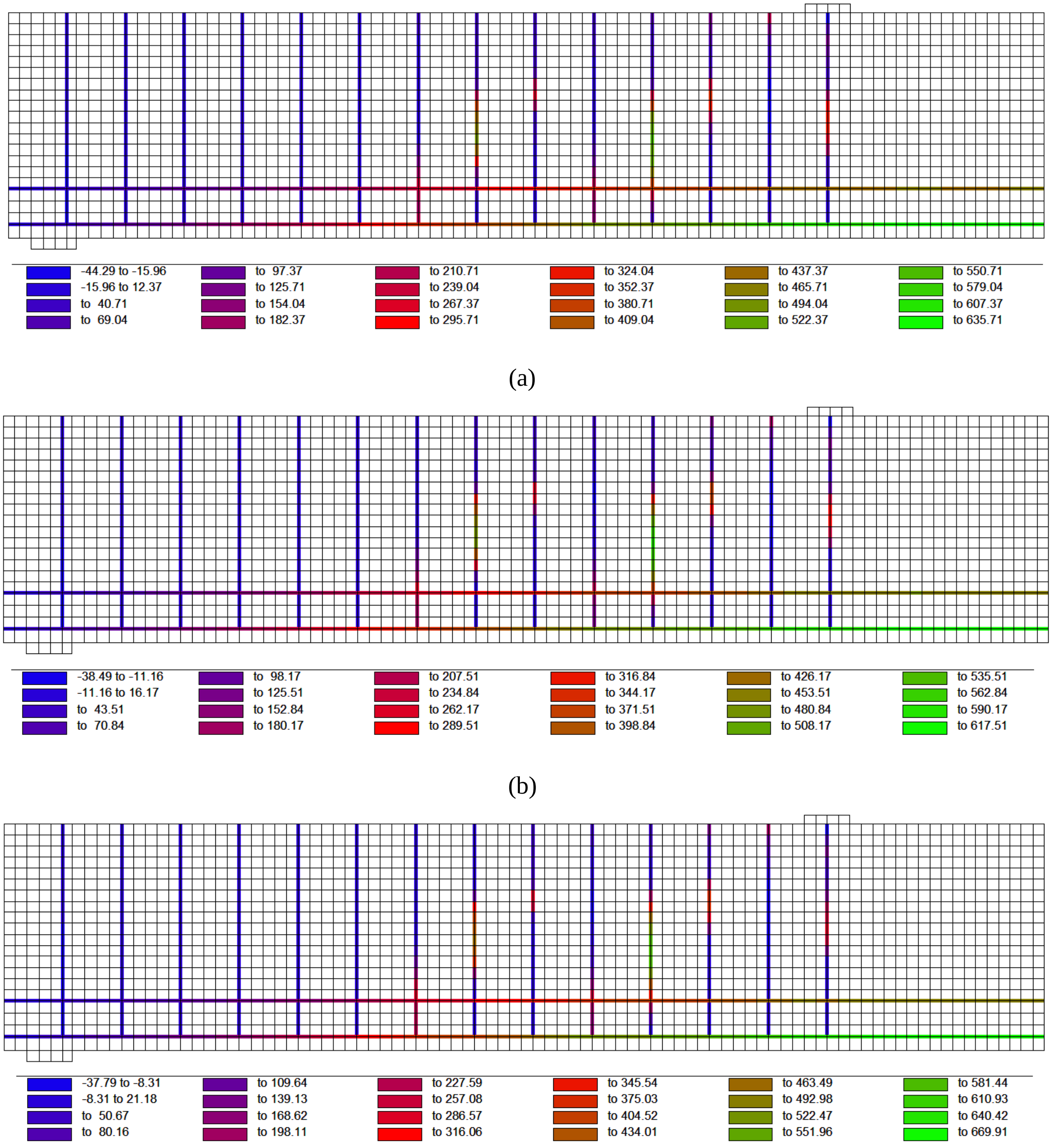

(a)

(b)

(c)

Figure 5.38. Axial stress distribution in the steel reinforcement of beams (a) S_cr0.59, (b) S_cr0.69, and (c) S_cr0.77 (units in MPa)

5.5 Parametric Analysis Summary

Concrete resistance against frost damage is influenced by internal and external climate factors. The most influential internal parameters discussed in this chapter are moisture content and air content. The number of freeze thaw cycles is an external climate factor that was also investigated in this chapter. From the results of the parametric analysis, the following conclusions are drawn:

1. The damage accumulated over the course of a reinforced concrete beam's service life due to repeated freeze-thaw cycles has a significant impact on the load-carrying capacity of the member.
2. With the progression of time and over the course of the beam's service life, there is stiffness degradation and a reduction in the load-carrying capacity of the beam which reflects the increase in the extent of frost damage.
3. The greatest loss of stiffness and overall flexural strength is experienced in the first 10 years. Between 25 years and 75 years, the magnitude of reduction in load-carrying capacity is relatively low.
4. The comparison between the load-deflection response of the beam in service in Calgary, Ottawa and St. John's after 10, 25 and 74 years indicates that when considering the reduction in the load-carrying capacity, it is important to consider the climate data of the city that the reinforced concrete structure is serving.
5. The initial stiffness does not change with the degree of saturation; however, the load-deflection response of the beam deteriorates as the moisture content is increased.
6. The effect of frost damage on the structural response of reinforced concrete members is intensified when the degree of saturation is increased.
7. Effects of increasing air content and subsequently lowering S_{cr} include a reduction in the capacity to sustain loading, provided the concrete is saturated.
8. For concrete with a lower critical saturation degree, there is greater stiffness degradation and reduction in the load-carrying capacity of reinforced concrete flexural members.

The structural response of frost-damaged reinforced concrete members is most critically affected by the air content, which is related to the critical degree of saturation, and the quality of the air pore system, which is related to critical spacing factor. Concrete becomes susceptible to damage only when the degree of saturation exceeds the critical value and therefore, considering the critical degree of saturation in the design of reinforced concrete structures subjected to freeze-thaw cycles is of vital importance. When the pore saturation is below the critical value, the freezing of water fills up the void space before exerting stress on the pore wall; the phase change from water to ice inside the pore will not damage the solid matrix of the material. The critical spacing factor between air pores is also of vital importance to the performance of reinforced concrete structural members. Water flow, arising from the 9% volume increase from ice formation, generates pressure. If the distance for the water to flow from freezing site to the nearest air-filled space is below the critical distance then, the effects are marginal. Damage does not occur when the saturation degree is less than the critical saturation degree and the flow distance is below the critical flow distance. If either the critical degree of saturation or the critical flow distance is exceeded, the reinforced concrete member will experience frost damage during a freezing cycle, and therefore, it is imperative that these two parameters be considered in the design of reinforced concrete structures subjected to freeze-thaw cycles.

Chapter 6. Concluding Remarks

6.1 Conclusions

The effects of frost damage on reinforced concrete flexural members were studied in order to propose a structural analysis method that accounts for the degradation of the load-carrying capacity and stiffness of frost-damaged reinforced concrete flexural members. A methodology was introduced in which frost damage is accounted for by incorporating the material properties of deteriorated and frost-damaged concrete in existing analytical constitutive models for concrete in compression and tension and for bond steel-concrete interaction, and by modifying the member's geometry to account for surface scaling. VecTor2 is the nonlinear finite element software used in this study for the analysis of frost-damaged reinforced concrete members. The analysis procedure was validated with published experimental results of reinforced concrete beams subjected to frost damage. From the results of the validation stage, the following conclusions can be made

1. The effects of frost damage on the load-carrying capacity and the changes in failure mode were captured by changing the material and bond properties as well as the cross-section of the damaged concrete.
2. In general, the proposed methodology was more effective in predicting the response of flexural governed than shear-governed beams.

Once the methodology was validated, it was used to investigate parameters that influence the damage caused by successive freeze-thaw cycles in reinforced concrete flexural members. The number of freeze-thaw cycles is an external variable that was investigated as part of the parametric study. Internal variables were also considered and include moisture content and air content. The parametric analysis included the study of the following beam characteristics:

1. Load-deformation curves
2. Loss in strength
3. Loss in ductility

The results from the numerical analysis were used to identify the effects of the parameters and to highlight trends within the results relating to these parameters. From the parametric study, the following conclusions can be made:

1. The damage accumulated over the course of a reinforced concrete beam's service life due to repeated freeze-thaw cycles has a significant impact on the load-carrying capacity of the member.
2. With the progression of time and over the course of the beam's service life, there is stiffness degradation and a reduction in the load-carrying capacity of the beam which reflects the increase in the extent of frost damage.
3. The greatest loss of stiffness and overall flexural strength is experienced in the first 10 years.
4. Between 25 years and 75 years, the magnitude of reduction in load-carrying capacity is relatively low.
5. The comparison between the load-deflection response of the beam in service in Calgary, Ottawa and St. John's after 10, 25 and 74 years indicates that when considering the reduction in the load-carrying capacity, it is important to consider the climate data of the city that the reinforced concrete structure is serving
6. The initial stiffness does not change with the degree of saturation; however, the load-deflection response of the beam deteriorates as the moisture content is increased.
7. The effect of frost damage on the structural response of reinforced concrete members is intensified when the degree of saturation is increased.
8. Effects of increasing air content and subsequently lowering S_{cr} include a reduction in the capacity to sustain loading.
9. For concrete with higher air content, and thus a lower critical saturation degree, there is greater stiffness degradation and reduction in the load-carrying capacity of reinforced concrete flexural members.

The objective of this study was to model the effects of frost damage on reinforced concrete flexural members in order to provide a reliable methodology to asses deteriorated concrete structures. The important findings of this study to consider in the assessment of existing structures include:

1. Incorporating frost damage effects through the stress–strain response of concrete in compression, the stress-crack opening relation in tension and the bond–slip behaviour changes the behaviour of frost-damaged reinforced concrete flexural member changes, and therefore, they should be considered in the analysis.
2. The effects of frost damage can be taken into account through modification of the concrete cross-section, the response of the materials in tension and compression and the bond–slip relation.
3. The changes in the effective material and bond properties results in change in the failure mode of reinforced concrete members.

6.2 Future Work

The method introduced to account for frost damage in the two-dimensional FE model should be further developed for three-dimensional analysis to account for the out-of-plane damage. Furthermore, the extension and distribution of the damage over the cross-section should be more extensively studied as it affects prediction of the failure load and deformation. For reinforced concrete elements, the application of de-icing salts raises concerns over not only frost damage, but also corrosion of embedded reinforced steel bars. In Canadian winters especially, these deterioration mechanisms usually appear concurrently. To better understand the combined effects of these two deterioration mechanisms on the response of reinforced concrete members, the analysis procedures currently used to model reinforcement corrosion should be applied with the proposed methodology to model frost-damage. Design and assessment guidelines should be developed upon further investigation of the effects frost damage on design parameters. Suggestion to modify these parameters in order to account for deterioration could be provided in assessment guidelines of existing deteriorated concrete structures.

References

Berto, L., Saetta, A., and Talledo, D. (2015). “Constitutive model of concrete damaged by freeze–thaw action for evaluation of structural performance of RC elements.” *Construction and Building Materials*, **98**(Supplement C), 559-569.

Broo, H., Lundgren, K., and Plos, M. (2008). “A guide to nonlinear finite element modelling of shear and torsion in concrete bridges.” Report 2008:18, Civil and Environmental Engineering, Chalmers University of Technology, Göteborg, Sweden.

CSA A23.1/A23.2 (2019). "Concrete materials and methods of concrete construction/Test methods and standard practices for concrete." Canadian Standards Association, Mississauga, ON, Canada.

CSA A23.3-04 (2019). "Design of Concrete Structures." Canadian Standards Association, Mississauga, ON, Canada.

Coussy, O. (2005). “Poromechanics of freezing materials.” *Journal of Mechanics and Physics of Solids*, **53**, 1689-1718.

Eligehausen, R., Popov, E., and Bertero, V. (1983). “Local Bond Stress-Slip relationship of Deformed Bars under Generalized Excitations.” Report UCB/EERC-83/23, Earthquake Engineering Center, University of California, Berkeley.

Fagerlund, G. (1993). “On the service life of concrete exposed to frost action.” Report TVBM-7054, Division of Building Materials, Lund Institute of Technology, Sweden.

Fagerlund, G. (1995). “Frost damage on concrete Estimation of the future deterioration.” Report TVBM-3067, Division of Building Materials, Lund Institute of Technology, Sweden.

Fagerlund, G. (1997). “Internal frost attack - state of the art: suggestions for future research.” Report TVBM (Intern 7000-rapport); Vol. 7110, Division of Building Materials, Lund Institute of Technology, Sweden.

Fagerlund, G. (2002). “Mechanical damage and fatigue effects associated with freeze-thaw of materials.” *In Proceedings of 2nd International RILEM Workshop on Frost Resistance of Concrete,* eds. Setzer M.J., Auberg R., Keck H.-J. RILEM, Essen, pp. 117–132.

Fagerlund, G. (2004). “A service life model for internal frost damage in concrete.” Report TVBM-3119, Division of Building Materials, Lund Institute of Technology, Sweden.

GCC (2019) *Government of Canada Climate Report*. Government of Canada Climate, Canada.

Hanjari, K. Z., Utgenannt, P., and Lundgren, K. (2011). “Experimental study of the material and bond properties of frost-damaged concrete.” *Cement and Concrete Research*, **41**(3), 244–254

Hanjari, K. Z., Kettil, P., and Lundgren, K. (2013). “Modelling the structural behaviour of frost-damaged reinforced concrete structures.” *Structure and Infrastructure Engineering*, **9**(5), 416-431.

Hassanzadeh, M., and Fagerlund, G. (2006). “Residual strength of the frost-damaged reinforced concrete beams” III European conference on computational mechanics solids, structures and coupled problems in engineering, 5–8 June 2006, Lisbon, Portugal, 336.

Ho, E., and Gough, W. (2006). “Freeze thaw cycles in Toronto, Canada in a changing climate.” *Theoretical and Applied Climatology*, **83**(1), 203-210.

ICOLD (1984) *Deterioration of Dams and Reservoirs: Examples and their Analysis*. International Committee on Large Dam, Balkema Publishers, Boorkfield, VT.

IPCC (2001) *Climate change 2001: Impacts, adaptations, and vulnerability,* Intergovernmental Panel on Climate Change, New York: Cambridge University Press.

Li, A., Xu, S., Wanng, Y., (2017). “Effects of Frost-damage on Mechanical Performance of Concrete.” *Journal of Wuhan University of Technology-Mater. Sci. Ed*, **32**(1), 129-135.

Li, K., (2016). “Durability design of concrete structures phenomena, modeling, and practice.” Singapore: Wiley.

Li, W., Pour-Ghaz, M., Castro, J., and Weiss, J. (2012). “Water absorption and critical degree of saturation relating to freeze-thaw damage in concrete pavement joints.” *Journal of Materials in Civil Engineering*, **24**(3), 299-307.

Lindmark, S. (1993). “Effect of variations in salt concentration, salt distribution and freeze-thaw cycle at a salt scaling test according to the Swedish Standard SS 137244.” Report M2:01, Lund Institute of Technology, Lund, Sweden.

Lohaus, L., and Petersen, L. (2002). “Influence of Frost Deterioration on Concrete Properties,” *Beton*, **12**(2) Publisher Building and Technics, Germany.

Ma, Z., Zhao, T., Yang, J. (2017). “Fracture Behavior of Concrete Exposed to the Freeze-Thaw Environment.” *Journal of Materials in Civil Engineering,* **29**(8), 1-10.

Nili, M., Azarioon, A., and Hosseinian, S. M. (2017). “Novel Internal-Deterioration Model of Concrete Exposed to Freeze-Thaw Cycles.” *Journal of Materials in Civil Engineering,* **29**(9), 1-11.

Petersen, L., Lohaus, L., Polak, Maria Anna. (2007). “Influence of Freezing-and-Thawing Damage on Behavior of Reinforced Concrete Elements.” *ACI Materials Journal,* **104**(4), 369-378.

Pigeon, M., Marchand, J., and Pleau, R. (1996). “Frost resistant concrete.” *Construction and Building Materials,***10**(5), 339-348.

Powers, T.C. (1949) “The air requirement of frost resistant concrete.” *Highway Research Board Bulletin*, **29**, 184-211.

Powers, T.C., and Helmuth, R.A. (1953) “Theory of volume changes in hardened Portland cement paste during freezing.” *Highway Research Board Bulletin*, **32**, 285–297.

Qin, X.-C., Meng, S.-P., Cao, D.-F., Tu, Y.-M., Sabourova, N., Grip, N., Ohlsson, U., Blanksvärd, T., Sas, G., and Elfgren, L. (2016). “Evaluation of freeze-thaw damage on concrete material and prestressed concrete specimens.” *Construction and Building Materials,* **125**(Supplement C), 892-904.

Qin, Q., Zheng, S., Li, L., Dong, L., Zhang, Y., and Ding, S. (2017). “Experimental Study and Numerical Simulation of Seismic Behavior for RC Columns Subjected to Freeze-Thaw Cycles.” *Advances in Materials Science and Engineering,* 2017, 1-13.

Romben, L. (1973). Report of Activities 1972-73, The Swedish Cement and Concrete Research Institute, Stockholm.

Scherer, G. W. (1999). “Crystallization in pores.” *Cement and Concrete Research,* **29**, 1347–1358.

Setzer, M. J. (2001). “Micro-ice-lens formation in porous solid.” *Journal of Colloid and Interface Science,* **243**, 193–201.

Tang, L., and Petersson, P.E. (2004). “Slab test: Freeze/thaw resistance of concrete – internal deterioration.” *Materials and Structures,* **37** (274), 754–759.

Thorenfeldt, E., Tomaszewicz, A., and Jensen, J.J. (1987). “Mechanical properties of high-strength concrete and applications in designed.” Conference on Utilization of High-Strength Concrete, Stavanger, Norway, 149–159.

Wong, P. S., and Vecchio. F.J. (2002). "VecTor2 and FormWorks User's Manual."

Xu, S., Li, A., and Wang, H. (2017). “Bond properties for deformed steel bar in frost-damaged concrete under monotonic and reversed cyclic loading.” *Construction and Building Materials,* **148**(Supplement C), 344-358.

Yang, W., Ge, Y., Zhang, B., & Yuan, J. (2011). “Effect of Saturation Degree on Concrete Deterioration due to Freeze-Thaw Action.” *Key Engineering Materials,* **477**, 404-408.

Zhenhai, G., Xudong, S. (2003). “Reinforced Concrete Theory and Analyse.” Tsinghua University Press, Beijing.